Multiscale Modelling of Haemorrhagic Transformation After Ischaemic Stroke

JIAYU WANG
Somerville College
SUPERVISOR: Prof. S. J. PAYNE



Cerebral Haemodynamics RESEARCH GROUP
DEPARTMENT OF ENGINEERING SCIENCE
UNIVERSITY OF OXFORD

A thesis submitted in partial fulfilment of the requirements of
the degree of Doctor of Philosophy
Trinity Term 2022

Multiscale Modelling of Haemorrhagic Transformation After Ischaemic Stroke

Jiayu Wang, Somerville college, University of Oxford

A thesis submitted for the degree of Doctor of Philosophy

Trinity Term 2022

The brain occupies around 2 % of human adult bodyweight but accounts for nearly 20% of metabolism in the body and 14% of blood flow. With an increasingly elderly population globally, the impacts of cerebrovascular diseases, such as stroke and dementia, are becoming increasingly significant. Notably, the clinical challenge of stroke is growing. For example, the data collected by the Stroke Association show that there are approximately 17 million new stroke patients across the world and more than 100,000 strokes each year in the UK.

Haemorrhagic transformation (HT) is one of the most common complications after ischaemic stroke caused by damage to the blood–brain barrier (BBB) that could be the result of stroke progression or a complication of stroke treatment with reperfusion therapy, causing bleeding in the brain. This can lead to further damage to the brain tissue and can increase the risk of disability or death. To better assist in understanding this, in this thesis a new intracerebral haemorrhagic transformation model is presented. This model is divided logically into three steps, starting from simulating haemorrhage in a single vessel to HT in a 3-dimensional vasculature model, and eventually applying this model within a whole brain model.

In the first model, a mathematical model of HT is developed to simulate the consequence of HT over a range of vasculature length scales. Then in the second study, this model is developed further into an enlarged multi-scale microvasculature model in order to investigate the effects of HT on the surrounding tissue and vasculature. Next, this HT is applied into a computational whole brain model. The effects of capillary compression and tissue displacement are also considered in these three models.

Finally, the volume of the haematoma is investigated in 15 subjects and used for validation against clinical imaging data. In addition, perfusion is calculated in the region of HT and used to compare with experimental data. This model is the first such to be able to simulate the

1 correlation between bleeding regions and haematoma, which may be of assistance in future
2 to assess the HT for clinicians.

Acknowledgement

I would first of all like to thank my supervisor, Stephen Payne, who introduced and encouraged me to apply for this DPhil studentship three years ago and then guided me through the entire study. An old saying in China goes, “admire a worthy man greatly as one stops looking up at a mountain top”. His teaching, support and guidance have been gratefully received.

This is in contrast to my girlfriend Shahan Jiang, MD, PhD, who doubts my research all the time and provides critical suggestions from an excellent clinician and biologist’s perspective. We often debate when she thinks my figures in slides and papers are dramatically ugly, but later she will help me generate wonderful figures by Illustrator.

I would also thank my parents, who have provided exceptional support and unconditional love throughout this embarkation, deserve the most credit. I am also greatly indebted to my friends, Haodong He, Rui Lei, Jia Wei, Yifei Zhang, Hanwen Zhang, Qingze Gu, Jiaqi Zheng and Tianxiong Wang, who have been all ears to my problems and was always giving the best advice.

I must also thank the members of Cerebral Haemodynamics Research Group. Thank Wahbi and Tamas as excellent mentors and for helping me develop my study in three years. Albert, thanks for your company and encouraging me to apply to this group three years ago. Xi, you are an excellent colleague and it’s my honour to complete this study with you. I also thank Katinka and Charles from Amsterdam, who support me from the clinicians’ perspective and without them, a key piece of this study would be missing.

My final thanks and love go to my dear motherland, China. Despite I am separated with her for three years and more than 5,000 miles apart, her love still can be touched.

Learn for the construction of a prosperous China.

为中华之崛起而读书。

-----Zhou, Enlai, a diplomat.

Dissemination

Peer-Reviewed Journal Papers (3 published)

- J. Wang and S. J. Payne, "Mathematical modelling of haemorrhagic transformation after ischaemic stroke," Journal of Theoretical Biology, p. 110920, 2021.
- J. Wang, K. R. van Kranendonk, W. El-Bouri, C. B. Majoie, and S. J. Payne, "Mathematical modelling of haemorrhagic transformation within a multi-scale microvasculature network," Physiological Measurement, 2022.
- Chen, X*., Wang, J*., van Kranendonk, K.R., Józsa, T.I., El-Bouri, W.K., Kappelhof, M., van der Sluijs, M., Dippel, D., Roos, Y.B., Marquering, H.A. and Majoie, C.B., 2023. Mathematical modelling of haemorrhagic transformation in the human brain. Applied Mathematical Modelling.

* These authors contributed equally.

Conference Presentations and Posters (3)

- Wang J, Payne SJ. Multiscale Modelling of Intracerebral Haemorrhage After Ischaemic Stroke. Cerebral Autoregulation Research Network I, 2021 April, Shenzhen.
- Wang J, Payne SJ. Multiscale Modelling of Intracerebral Haemorrhage After Ischaemic Stroke. 9th World Congress of Biomechanics (WCB) 2022, July, TAIWAN.

- Wang J, Payne SJ. Multiscale Modelling of Intracerebral Haemorrhage After Ischaemic Stroke. Computational and Mathematical Biomedical Engineering. 2022 July, Milan.

Contents

List of Abbreviations **1**
Nomenclature **3**
Chapter 1: Introduction **7**
1.1 Background 7
1.2 Motivation 12
1.3 Synopsis 12
Chapter 2: Literature Review **16**
2.1 Brain Physiology 16
2.1.1 Anatomy of the Cerebral Circulation 16
2.1.2 Blood Vessels 21
2.2 Stroke Pathology 25
2.2.1 Stroke 25
2.2.2 Ischaemic Stroke 26
2.2.3 Treatment of Ischaemic Stroke 29
2.3 Haemorrhagic Transformation Physiology 32
2.4 Vasculature models 38
2.4.1 Poiseuille's Law 38
2.4.2 Viscosity 39
2.4.3 Vascular Model 41
2.4.4 Microvasculature Models 45
2.4.5 Homogenization 50
2.5 Current Brain model 51
2.6 Measurements 58
2.6.1 Measurements of Blood flow 58
2.6.2 Measurements of Blood Volume 61
2.6.3 Measurements of Haematoma Volume 64
2.7 Verification, validation& uncertainty quantification 66
2.8 Summary 69
Chapter 3: Mathematical modelling of haemorrhagic transformation after ischaemic stroke **70**
3.0 Abstract 70
3.1 Introduction 71

3.2 Materials and Methods....73
3.2.1 Governing equations....73
3.2.2 Physiological parameter....81
3.2.3 Network models....82
3.3 Results....84
3.3.1 Leakage fraction....84
3.3.2 Haematoma volume....88
3.4 Discussion....92
3.5 Conclusion....98
3.6 Evaluating the Model: Advantages and Limitations....98
3.7 Appendix....100
Appendix 3.A Supplementary for the Green's Function....100
Appendix 3.B Viscosity vs. haematocrit....101
Appendix 3.C Haematoma formation time vs. haemostasis....102
Appendix 3.D Pseudo-algorithms....104
Chapter 4: Mathematical modelling of haemorrhagic transformation within a multi-scale microvasculature network....105
4.0 Abstract....105
4.1 Introduction....107
4.2 Materials and methods....110
4.2.1 Model formulation....110
4.2.2 Network model....114
4.3 Results....117
4.3.1 Single vessel model....117
4.3.2 Network model....121
4.4 Discussion....123
4.5 Conclusion....131
4.6 Evaluating the Model: Advantages and Limitations....132
4.7 Appendix....134
Appendix 4.A Animal model....134
Appendix 4.B Algorithm and convergence....135
Appendix 4.C Sensitivity analysis....136
Chapter 5: Mathematical modelling of haemorrhagic transformation in the human brain....138

5.0 Abstract 138
5.1 Introduction 140
5.2 Materials and methods 144
5.2.1 Perfusion Model[1] 144
5.2.2 Leakage model 146
5.2.3 Model Coupling[1] 149
5.2.4 Quantifications of CT images 153
5.3 Results 156
5.3.1 Haematoma location and volume measurements 156
5.3.2 Perfusion deficit quantification 159
5.3.3 Sensitivity analysis 159
5.4 Discussion 162
5.5 Conclusion 169
5.6 Evaluating the Model: Advantages and Limitations 169
5.7 Appendix 172
Appendix 5.A Discussion of model coupling procedures 172
Chapter 6: Conclusion, Final Discission and Future Direction 174
6.1 Thesis Summary 174
6.2 Further Discussion 177
6.2.1 Temporal scales 177
6.2.2 Therapy optimisation 177
6.2.3 Verification, validation, and uncertainty quantification 178
6.3 Future Work 181
6.3.1 Oedema and HT model 182
6.3.2 Virtual Imaging in validation 183
6.3.3 BBB breakdown modelling 184
6.3.4 Haemostasis 185
6.4 Final Remark 186
References: 187

List of Abbreviations

ACA	Anterior cerebral artery
ACT	Arteriole-capillary transition
APC	Activated protein C
ASL	Arterial spin labelling
BBB	Blood–brain barrier
BL	Basal lamina
B	Magnetic field
CBF	Cerebral blood flow
CBV	Cerebral blood volume
CPM	Cellular Potts Model
CSF	Cerebrospinal fluid
CT	Computed tomography
CTP	Computed tomography perfusion
DCE-MRI	Dynamic contrast-enhanced magnetic resonance imaging
DCI	Delayed cerebral ischemia
DSC-MRI	Dynamic susceptibility contrast magnetic resonance imaging
ECASS II	European Cooperative Acute Stroke Study II
FSL	FMRIB software library
GLUT1	Glucose transporter 1
HI1	Haemorrhagic infarction type 1
HI2	Haemorrhagic infarction type 2
HT	Haemorrhagic transformation
ICA	Internal carotid arteries
ICC	Intracranial compliance
ICG	Indocyanine green
ICH	Intracerebral haemorrhage
ICP	Intracranial pressure
IL-1β	Interleukin 1 beta
KPS	Permeability-surface area product
LRP	Receptor-related protein
MCA	Middle cerebral artery
MLS	Midline shift
MMP	Matrix metalloprotein
MMP-9i	Matrix metalloprotein-9 inhibitor
MRA	Magnetic resonance angiography
MRI	Magnetic resonance imaging
MT1-MMP	Membrane-tyoe-1 matrix metalloprotein
NF-κB	Nuclear factor-κB
PAR1	Protease activated receptor 1
PCs	Pericytes
PCAs	Posterior cerebral arteries

PET	Positron emission tomography
PH1	Parenchymal hematoma type 1
PH2	Parenchymal hematoma type 2
rCBV	Relative cerebral blood volume
rCBF	Relative cerebral blood flow
REV	Representative elementary volume
ROS	Reactive oxygen species
rt-PA	Recombinant tissue-plasminogen activator
TNF-α	Tumour Necrosis Factor Alpha
T1w-MR images	T1-weighted magnetic resonance images
SAH	Subarachnoid haemorrhage
sICHs	Symptomatic intracranial haemorrhages
SPECT	Single-photon emission computed tomography
T	Time constant
TBI	Traumatic brain injury
TJs	Tight junctions
TOF	Time-of-flight
VA	Vertebral arterioles
V&V	Verification and validation
VV&UQ	Verification, validation and uncertainty quantification

Nomenclature

α_a,α_v,β_a and β_v Nondimensional hydraulic conductivities

α^w Biot parameter for water

γ Leakage fraction

γ_i Individual leakage fraction

δ_{nj} Kronecker's delta function.

ϵ Scaling factor

ϵ' Ratio of vessel radius to vessel length

θ Angle of rotation

μ $(kg/m/s)$ Fluid viscosity in the interstitial space

$\mu_b(kg/m/s)$ Blood viscosity

μ_{rel} Relative blood viscosity

μ_w Water viscosity

$\mu_{0.45}$ Blood viscosity when haematocrit is 0.45

$\rho\left(g\,cm^{-3}\right)$ Cerebral tissue density

$\hat{\sigma}$ Surface area in Green's function

ω_{ij} fluid transfer coefficients between compartments i and j.

ω_{ij}^{g} fluid transfer coefficients between compartments i and j in grey matter.

ω_{ij}^{w} fluid transfer coefficients between compartments i and j in white matter.

A (μm^2¿ Cross-section area

$A^{'}$ Vascular surface area of exchange vessels per 100g of tissue

A_b Vessel lumen cross-sectional area at its maximum compliance point

CFC Capillary filtration coefficient

D (μm) Vessel diameter

D_{eff} (μm) Thickness of the endothelial surface layer

E Bulk modulus which represents the capillary wall stiffness

f Fraction of vessels remaining open

F Perfusion

$\Delta F\ (\%)$ Reduced perfusion

FPV Fractional perfused volume

G Shear modulus

h (μm) Vessel thickness

h_bVascular wall thickness at maximum compliance point

H_D Haematocrit

i Unit vector

$ICP(mmHg)$ Intracranial pressure

J_f Transcapillary filtration rate

k ($\mu m^3 s kg^{-1}$) Hydraulic conductivity

k_i Permeability tensor of compartment i

$K_a(m^2)$ Permeability tensor for the arteriole

K_b Permeability blood in the interstitial space

K_c and $K_c(m^2)$ Permeability tensor for the capillary

$K_v(m^2)$ Permeability tensor for the venule

K_w Permeability of water in the interstitial space

l (μm) Arc length

L (μm) Vessel length

L_o Linear differential operator

L_p ($\mu m^2 s kg^{-1}$) Vascular permeability

n Constant value that defines the degree of curvature of the pressure-area relationship

n Normal unit vector

$\overline{n}_b$ Volume fraction of blood vessel in a unit volume of brain tissue

Ne Number of elements

$\dot{p}(mmHg)$Definition of haematoma surface pressure in general

p' Definition of haematoma surface pressure change in percentage

$\overline{p}(mmHg)$ Baseline value of interstitial pressure

$p_a(mmHg)$ Blood pressure in arteriole

p_a' Blood pressure change in percentage

1 p_{aD} ($mmHg$) Darcy pressure in arteriole

2 p_c ($mmHg$) Capillary pressure

3 p_{cD} ($mmHg$) Darcy pressure in capillary

4 p_i ($mmHg$) Tissue pressure distribution

5 p_{io} ($mmHg$) Exterior interstitial pressure

6 $p_v(mmHg)$ Blood pressure in venule

7 p_{vD} ($mmHg$) Darcy pressure in venule

8 $p_w\ (mmHg)$ Hydrostatic interstitial fluid pressure

9 $P(mmHg)$ Pressure

10 $P_a(mmHg)$ Inlet arterial pressure

11 $P_v(mmHg)$ Inlet venous pressure

12 $P_o(mmHg)$ Ambient tissue pressure

13 P_{99}, $P_{15.1}$and $P_{15.5}$ ($mmHg$) Definitions of haematoma surface pressue

14 ΔP ($mmHg$) Transmural pressure

15 ΔP_{at} ($mmHg$) Inlet pressure and ambient pressure difference, $P_a - P_o$

16 $\Delta P_{av}(mmHg)$ Network pressure difference, $P_a - P_v$

17 PV Principle value

18 q' Dimensionless parameter of leakage flux

19 q_eLeakage flux vector

20 Q (mm^3/s) Flowrate

21 Q_a (mm^3/s) Inlet capillary flowrate

22 Q_c (mm^3/s) Capillary flowrate

23 Q_v (mm^3/s) Outlet capillary flowrate

24 $Q_{flux}(mm^3/s)$ Flow flux from the blood vessel

25 r (μm) Vessel radius

26 $r_{mb}(\mu m)$ Vessel lumen radius at its maximum compliance point

27 $R(\mu m)$ Haematoma radius

28 R Radial direction axis

29 R_{res} ($kg/mm^4/s$) Flow resistance

1 R_{es} Dimensionless flow resistance

2 $\dot{s}_{ce}(mm¿¿3/s)¿$ Leakage flow rate from the bleeding region

3 $t(mins)$: Computational time

4 S ($\mu m^2¿$ Surface area

5 $T(min)$ Haematoma formation time

6 u Fluid velocity vector

7 $U(\mu m)$ Tissue displacement

8 v ($\mu m/s$) Blood velocity

9 v' Poisson's ratio

10 $V(mm^3)$ Haematoma volume

11 $V^{'}$(%) Haematoma volume change

12 $V^{-¿¿}$ (%) Reduced haematoma volume

13 $V^{+¿¿}$ (%) Increased haematoma volume.

14 $V^{¿}$ (mm^3) Volume in Green's Function

15 V_t (mm^3) tissue volume

16 V_{total} (mm^3/s) Total volumetric blood flowrate

17 $x=(Z,R,\theta)$and $x'=(Z',R',\theta')$ Field point

18 (x,y,z) Haematoma centre

19 $Z(\mu m)$ Horizontal distance of x(field point) from the vessel entrance point

Chapter 1: Introduction

The purpose of this chapter is to introduce an overview of haemorrhagic transformation (Section 1.1) and gaps in the current understanding of this clinical phenomenon and models of it, to provide a clear motivation for the thesis (Section 1.2). Section 1.3 then provides a synopsis of this thesis, including brief methods and results in this model.

Please be aware that all acronyms and abbreviations utilized in this thesis are detailed in the "List of Abbreviations" section and will be described when first introduced in the text.

1.1 Background

The brain is a highly dynamic system that needs continuous and sufficient supplies of nutrients, primarily oxygen and glucose, to maintain adequate cerebral metabolism. With an increasingly elderly population globally, cerebrovascular diseases have become growing and significant clinical challenges. In particular, stroke is one of the most severe and important causes of damage to brain tissue and a leading cause of death and disability (Payne, 2017). Meanwhile, the most significant factor leading to stroke is age (Carandang et al., 2006).

The Stroke Association shows that there are more than 100,000 strokes each year in the UK and approximately 17 million new stroke patients per year across the world (Association, 2016). Patel et al. (2017) have predicted that the rate of first-time strokes in people aged 45 and over is expected to increase by 59% in the next 20 years.

Two main types of strokes have been classified based on their pathology, ischaemic stroke and haemorrhagic stroke. The first type of stroke is caused by blockage of a major

blood vessel to cut off the blood supply to brain regions, and the second type is caused by disruption of the blood vessel wall, leading to a significant amount of blood leakage and increasing intracranial pressure.

In the context of ischaemic stroke, however, it is also important to consider haemorrhagic transformation (HT), since this is a frequent, often asymptomatic, complication after acute ischaemic stroke onset (Álvarez-Sabín et al., 2013), and one that can lead to long-term morbidity and mortality by causing bleeding in the brain via damaged blood vessels. (Marsh et al., 2013). Tan et al. (2014) reported that spontaneous HT was observed in 50 of 407 patients (12.3%) and HT was observed in 29 patients (12%) in the study by Terruso et al. (2009).

HT is commonly classified according to the European Cooperative Acute Stroke Study II (ECASS II) classification based on radiological appearance (Milloy and Wood, 2015). This classification divides HT into four types: haemorrhagic infarction type 1 (HI1), which is defined as small petechiae (tiny spots of bleeding) along the peripheral margins of infarct; haemorrhagic infarction type 2 (HI2), defined as confluent petechiae within the infarcted area but without mass effect; parenchymal hematoma type 1 (PH1) as blood clots in $\leq 30\%$ of the infarcted area with some slight mass effect; and parenchymal hematoma type 2 (PH2) as blood clots in ¿30% of the infarcted area with substantial mass effect (Milloy and Wood, 2015).

HT is caused by disruption of the blood–brain barrier (BBB) and can result in significant damage to brain tissue. However, HT can also occur as a complication of stroke treatment with thrombolytic therapy (Group, 1996) and often BBB breakdown can be

caused by a combination of severe ischaemic stroke and thrombolytic therapy (Lakhan et al., 2013). Nowadays only recombinant tissue-plasminogen activator (rt-PA) is known to be effective for thrombolytic therapy (O'Collins et al., 2006). rt-PA has the ability to break down the blood clots by catalysing the transformation of plasminogen to plasmin. However, there are side effects caused by rt-PA, such as the increased risk of haemorrhage, which is due to the change of the permeability of the BBB with the development of cerebral oedema (Kassner et al., 2009). The functional outcome of patients with HT varies, however patients with large haematomas are most likely to have a poor functional outcome (van Kranendonk et al., 2019).

BBB breakdown is a crucial aspect to haemorrhage. Thus, it is worth investigating the structure of blood vessels and the barrier between blood vessels and brain tissue. Blood vessels are divided into three main types, arteries, capillaries and veins, and together comprise the cerebral circulation that plays a vital role in blood supply in the brain and is responsible for transporting nutrients to tissue cells. To create a diffusion barrier, tight junctions (TJs) are present between the cerebral endothelial cells.

The current brain models, simulating blood flow across different length scales, allow researchers to investigate haemodynamics both within blood vessels and in tissue (as shown in Figure 1.1). A large number of brain studies use a single vessel as a starting point (Pozrikidis and Farrow, 2003, Pozrikidis, 2013, Payne and Lucas, 2018). Meanwhile, penetrating networks with an enlarged vasculature length scale are also widely used to investigate and to quantify the influence of abnormal blood flow to surrounding healthy blood vessels and tissue (El-Bouri and Payne, 2018, Acosta et al., 2015, Safaeian et al.,

2011, Safaeian and David, 2013). Furthermore, a series of studies into ischaemic stroke has been applied on full brain models to investigate, for instance, the development of oedema, blood pressure, and other factors (Józsa et al., 2021, Padmos et al., 2021).

This study has three main goals:

1. From a modelling perspective: to build a governing mathematical model to describe the performance of HT, from micro to macro.
2. From a physiology perspective: the process of blood vessel damage and bleeding can be described by unified mathematical formulas, by considering and verifying the physical characteristics of blood vessels and tissues.
3. From a clinical perspective:

   3.1. to answer whether the HT can be predicted after ischaemic stroke, i.e., whether or not clinicians can identify those patients who are most at risk of haemorrhage based on available imaging data and other non-imaging parameters. 3.2. to assist clinicians to identify bleeding vessels or narrow bleeding regions, shortening treatment time.

Meanwhile, the consequences of HT can also be simulated and compared with experimental data. By creating a haemorrhage model than goes from a cortical scale to a whole brain scale model, based on mechanical behaviour and data validation with clinical results, researchers and clinicians may in the future be able to predict the occurrence and outcome of intracerebral haemorrhage accurately, leading to improved therapies and treatment outcomes.

Due to the limited experimented data and imaging technology, the limitations and constraints of each simulation will be explicitly defined and explored, along with a discussion on whether these can be resolved in the subsequent model. The potential benefits that each model provides to assist clinicians will also be part of the discussion. The three goals of this model have been partially answered: for example, a mathematical model to describe HT has been developed by considering available haemodynamics and imaging data. However, from a clinical viewpoint, challenges persist due to the limitations in the imaging data.

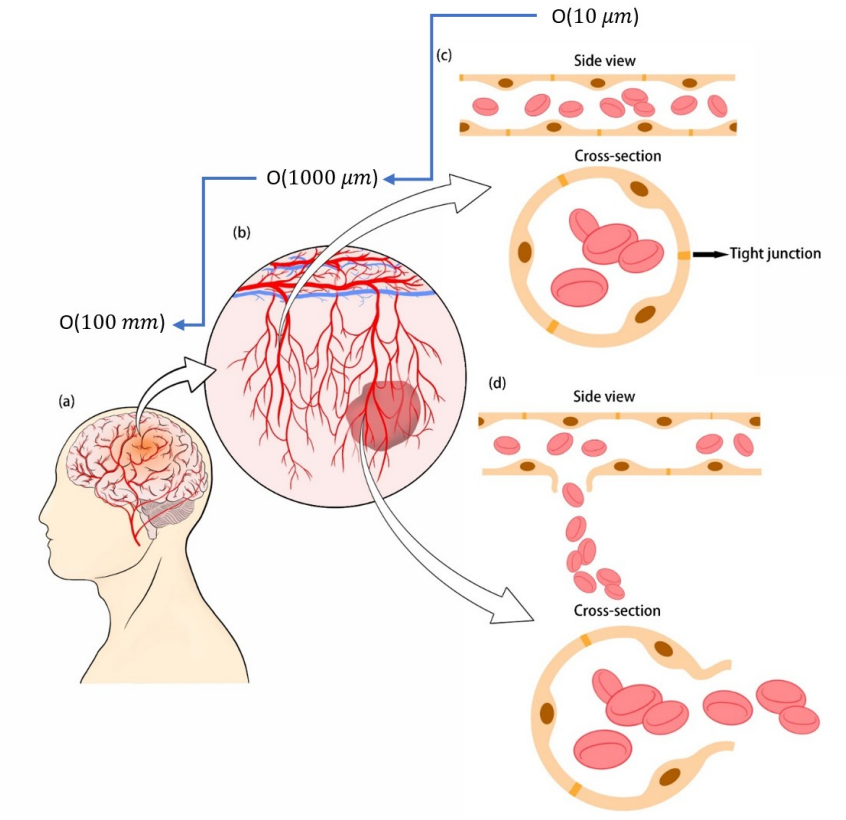


Figure 1.1 Macroscopic (a) and microscopic (b, c, d) configurations of haemorrhagic transformation simulation across different length scales: (a) HT model in whole brain model; (b) simulation of HT in penetrating network: (c) healthy vessel; (d) haemorrhagic vessel with breakdown of BBB (usually diagnosed with HI1 or HI2).

1.2 Motivation

The motivation for this project is therefore to develop a new model which is able to simulate the severity of haemorrhage across all the vasculature length scales. The model will be presented as a mechanical leakage model for an individual vessel at first. Then this mechanical model will be applied on a 1-dimensional vasculature model with multiple generations which are displayed as having different geometries. This model should have capabilities to display several severe properties of the haemorrhage for different blood vessels. Properties such as blood leakage fraction and haematoma volume can then be selected to describe the severity of the haemorrhage.

Furthermore, this simulation will be extended to a 3-dimensional vasculature haemorrhage model. By enlarging the vessel number and cube scale (the size of the 3-dimensional vasculature network model), the interactions between nearby vessels and the impact of tissue displacement can be displayed. The final step is modelling the whole cerebral haemorrhage. By validating this intracerebral haemorrhage model with clinical data, an optimised model can be obtained which can in future predict the severity of HT, the patients who are most at risk of haemorrhage and suggest to clinicians the optimal therapy or combinations of therapy, such as blood pressure control in place of rt-PA treatment.

1.3 Synopsis

The literature review (Chapter 2) contains more detailed background information and highlights the current gaps in this research area, as well as the available experimental and clinical results. Brain physiology is introduced first, including the cerebral circulation and blood vessel structure. Then stroke pathology comprising both haemorrhagic stroke and ischaemic stroke is described in the next section before introducing thrombolytic therapy, a treatment for ischaemic stroke and haemorrhagic transformation is discussed in detail. The following sections include the haemodynamics and vasculature network model information. Then the current brain model will be introduced and the feasibility of the brain model discussed. The next part of this chapter provides the background information for methods to measure the blood flow, blood volume and haematoma volume. The concluding segment of this chapter presents the methodology known as "Verification, Validation, and Uncertainty Quantification (VV&UQ)".

Chapter 3 is a description of the mathematical methods used to solve the leakage fraction and haematoma volume. The aim of this study is to develop a mathematical model that can be used to simulate the consequence of HT over a range of vasculature length scales. A 2D vasculature model is used to investigate the severity of HT with different vascular geometry. The resulting model shows that the haematoma radius is approximately constant across different length scales ($100-1000\,\mu m$) and is in good agreement with the available experimental data. In addition, this study identified that the effects of capillary compression do appear to have a significant impact on the leakage fraction of blood and hence act to restrain the development of a haematoma.

In chapter 4, the mathematical model is applied to a penetrating network in order to investigate the effects of HT on the surrounding tissue and vasculature. In addition, this study investigates the relationship between tissue displacement and vascular geometry. A voxel-scale model can be used to compare this HT simulation with available clinical imaging data for perfusion and cerebral blood volume (CBV) in the multi-scale microvasculature network.

Table 1.1 Summary of the models in Chapter 3, 4 and 5.

Chapters	Model of HT in	Highlights	Main assumptions
#3	a 2D microvasculature model	3.1 Developing a mathematical model to simulate the severity of HT. 3.2 Haematoma radius' dependences on haemodynamics and geometry of the vessels are not significant. 3.3 Capillary compression has been shown a greater impact to venules than arterioles and capillary generations. 3.4 Capillary compression can reduce blood leakage and restrain haematoma development.	3.1 The disruption of the BBB is assumed to occur in a homogeneous manner. 3.2 The blood, comprised of blood cells suspended in liquid, is assumed to behave as a uniform fluid. The blood flow is assumed to be laminar and steady, and that blood is incompressible. 3.3 Brain tissue is assumed to be an isotropic porous medium. 3.4 The method employed for determining the haematoma surface involved the utilization of a specific pressure. 3.5 Haematoma is assumed to be of the form with no mass effect. 3.6 The formation of haematoma is assumed to be fast enough such that haemostasis does not occur. 3.7 The whole vessel is assumed to be permeable to simplify the calculations in this study.
#4	a penetrating network	4.1. Developed a mathematical model to simulate HT within a multi-scale microvasculature network. 4.2. Enabled simulation of HT severity and hemodynamic post-HT onset. 4.3. The model showed that larger vessel breakdown results in increased hematoma radius, elevated tissue displacement, and higher intracranial pressure. 4.4. A significant feature of the model is its ability to compare HT simulations based on reductions in cerebral blood	Assumptions (3.1-3.6) are consistently maintained within this model. 4.1. The middle third of the vessel is assumed permeable in this study。 4.2. Perfusion and relative cerebral blood flow can therefore be assumed to directly equivalent in this case.

		volume and perfusion.	
#5	a whole brain model	5.1 The first mathematical model is developed to simulate HT in the full brain. 5.2 This model is compared with real clinical images (MR CLEAN-NO IV). 5.3 A reduction in perfusion after HT onset is found in the range of 5-16%. 5.4 Increased blood glucose level and high blood pressure potentially lead to more severe HT.	Assumptions (3.1-3.6) are consistently maintained within this model. 5.1 Only the capillaries are assumed to be leaky when HT occurs. 5.2 In the haematoma model, following removal of the occlusion, the blood perfusion is assumed to be fully restored. 5.3 In the computational brain model, subregions were postulated to serve as the source of haemorrhage, as opposed to originating from specific blood vessels.

In chapter 5, the HT model is implemented within a full computational brain model. The mathematical model is extended further to integrate within the computational whole brain model. The different types of HI1, HI2 and PH1 are simulated and compared with clinical image data, in order to optimise the model. Then the consequences of HT and the factors that affect the severity of HT are investigated.

Finally, in Chapter 6, a summary of all findings and limitations in the thesis and suggestions for future work are presented.

Chapter 2: Literature Review

To develop a model of haemorrhage transformation (HT), the physiological background is required, including the haemorrhage transformation and the structure of the cerebral vasculature. In order to obtain the reference data for developing a vasculature model and a haemorrhage transformation (HT) model, experimental data and methods are also introduced here along with a description of the empirical equations used to calculate key parameters.

2.1 Brain Physiology

2.1.1 Anatomy of the Cerebral Circulation

In this section, the anatomy of the cerebral circulation is described, starting with the large arterial vessels. Figure 2.1 shows the four main large arterial vessels that supply blood to brain, the left and right internal carotid arteries (ICA) and the left and right vertebral arterioles (VA) (Willie et al., 2012, Alastruey et al., 2007). Each ICA bifurcates to develop a middle cerebral artery (MCA) and an anterior cerebral artery (ACA) to perfuse the temporal, parietal and frontal regions of the brain. The two VAs combine into the basilar artery, then divide into two symmetrical posterior cerebral arteries (PCAs) to deliver blood to the regions of the brain through a tree-like structure. The basilar artery connects the VAs with ICAs through a ring-like arterial structure, called the Circle of Willis (Papantchev et al., 2007). This is an important structure to maintain the perfusion and blood supply to different regions or territories of the brain even in the

presence of missing or occluded large vessels. However, this structure is only found in $58.6\,\%$ of patients (Papantchev et al., 2013). This means not all patients have the ability to compensate a reduction in blood flow through a collateral flow.

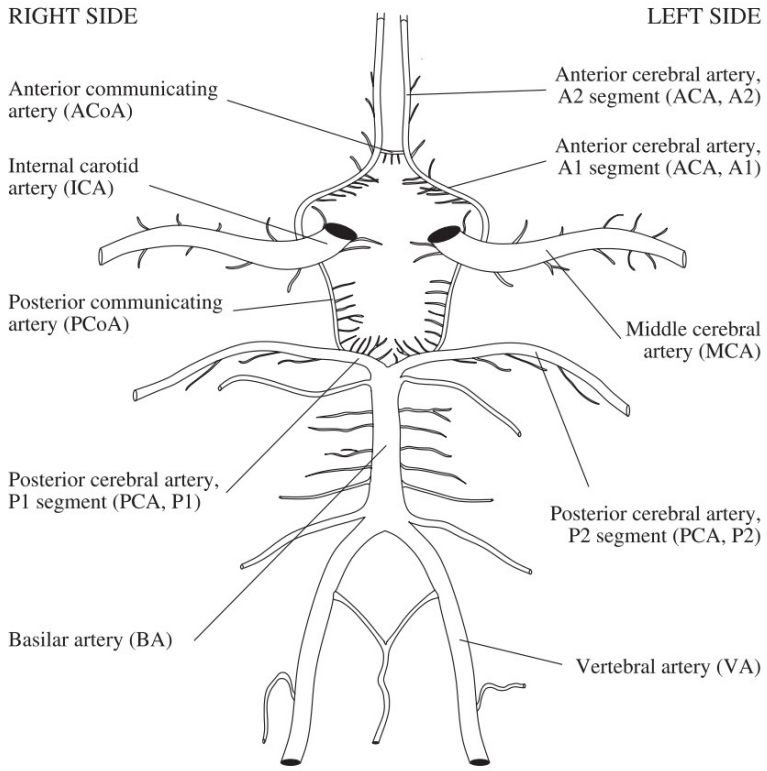


Figure 2.1 Schematic representation of the Circle of Willis and large arterial vessels.

Blood vessels play an essential role in blood supply in the brain and are responsible for transporting nutrients to tissue cells. Oxygen and glucose are the two primary nutrients and substances supplied to cells. The cerebral blood flow constitutes approximately 13% of the total body's blood circulation, with an estimated flow rate of around 750 mL/min (Vlachopoulos et al., 2011). Due to the fact that oxygen diffuses slowly but the cells in the brain consume oxygen rapidly for metabolism, every brain cell is located within a small distance, approximately $25\,\mu m$, of a blood vessel (Abbott et al., 2010). Thus, the

cerebral vasculature reaches into every part of the brain to supply the nutrients to each brain cell, as shown in Figure 2.2.

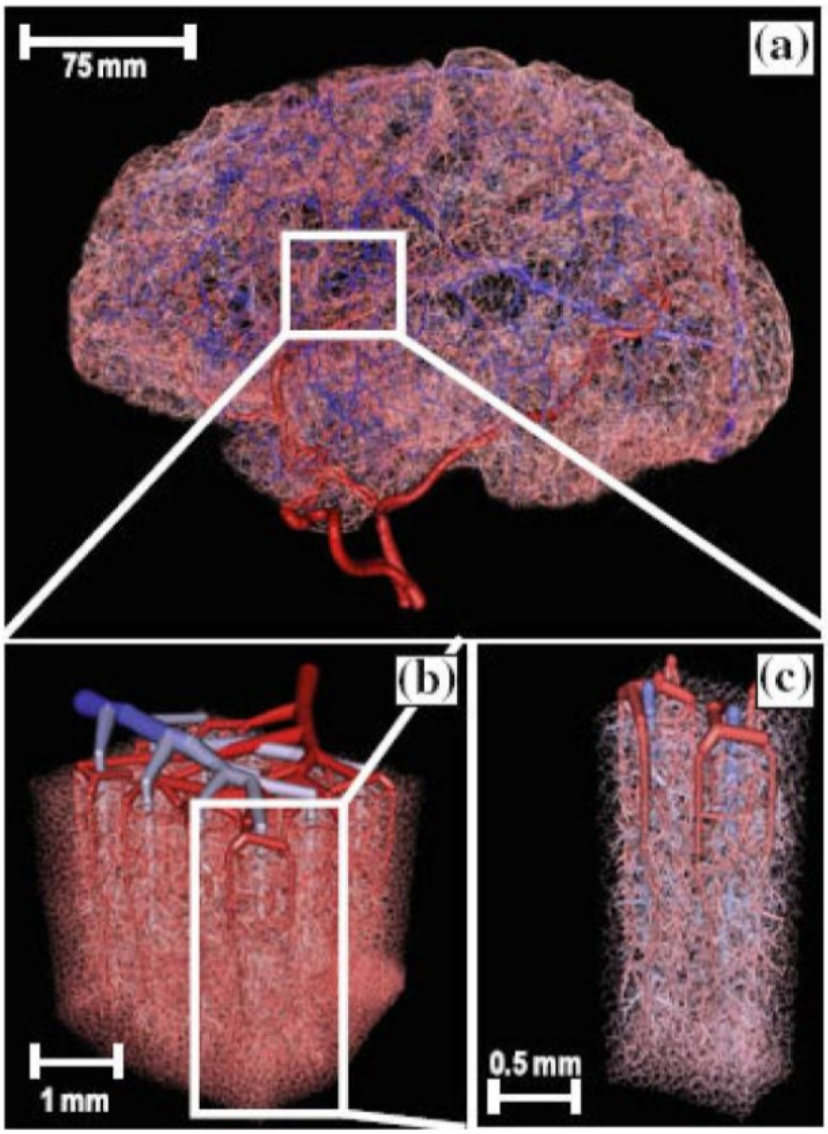


Figure 2.2 Overview schematic of the cerebral vasculature. This figure is reproduced from Linninger et al. (2013).

Blood vessels are divided into three main types: arteries, capillary and veins. Arteries contain an abundant concentration of oxygen and other nutrients and span multiple generations across different length scales down to the smaller arteries, arterioles. As

shown in Figure 2.3, the capillary network connects arterioles and venules (smaller veins) and is the predominant place that is responsible for exchanging oxygen, carbon dioxide and other nutrients and substances to tissue cells for supporting cerebral metabolism.

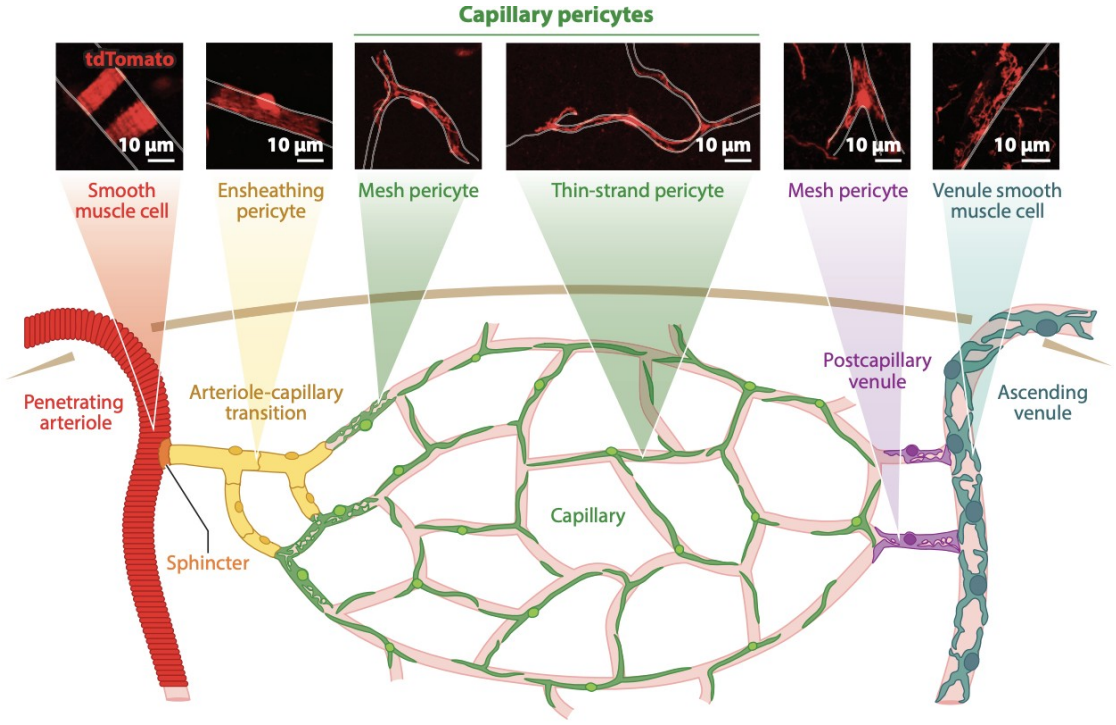


Figure 2.3 Schematic showing different zones of the brain microvasculature, including the pial arteriole, penetrating arteriole, arteriole-capillary transition (ACT), capillary, postcapillary venule, ascending venule, and pial venule. The precapillary sphincter is occasionally seen at the start of the ACT zone. The appearance and names of mural cells occupying these distinct zones, as seen from sparsely labeled (NG2-tdTomato or Myh11-tdTomato) mice, are shown. This figure is reproduced from Hartmann et al. (2022).

Apart from the arterial and venous circulations, the cerebral vasculature includes a smaller length scale blood vessel network, capillary network. These blood vessels are mainly small capillary vessels, which are responsible for transporting the key nutrients to the cells.

Different blood vessels have different proportions of each of three layers: arterioles have thick walls with a large fraction of smooth muscle cells since they act at high pressure to control blood flow; capillaries have very thin walls with no smooth cells, since they act at low pressure to supply nutrients through the wall to the surrounding tissue; veins have thinner wall than arteries, since they operate at a lower pressure than capillaries, although they have valves to ensure that the blood returns to the heart.

The venous circulation structure is shown in Figure 2.4. The intracranial venous system has unique anatomical characteristics. Veins in the brain are absent the muscular layer and valves; hence, the wall thickness of the veins is very thin (Egemen and Solaroglu, 2017). Three primary sinuses, superior sagittal sinus, straight sinus and occipital sinus, converge together at the back of the head, as shown in Figure 2.4. Then blood returns to the jugular vein via the sigmoid sinus. Blood drains into the heart through the neck via the superior vena cava.

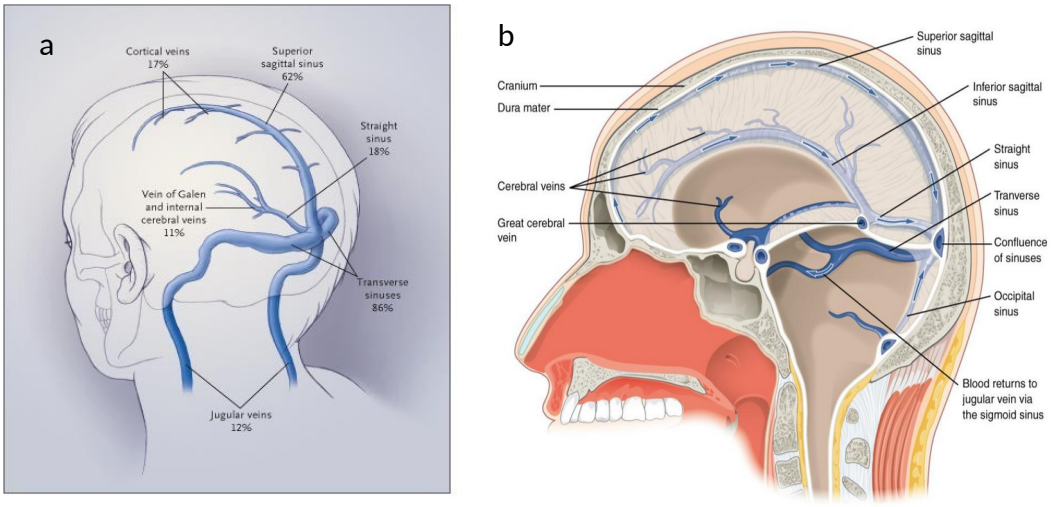


Figure 2.4 Schematic of brain large venous vessels. (a) Thrombosis frequency of the major cerebral veins and sinuses. (b) Detail structure of venous circulation. Reproduced without changes from OpenStax College under license

http://creativecommons.org/licenses/by/3.0/. This file can be shared freely under the Creative Commons Attribution 3.0 Unported license.

The anatomical and geometrical data of the capillary network in humans are limited due to the experimental data that are highly challenging to obtain in vivo. A brief summary of the available experimental and imaging data is given in Section 2.4.

2.1.2 Blood Vessels

Blood vessels are formed of hollow tubes and are responsible to the transportation of blood and nutrients. The blood vessel walls play a key role in the blood-brain barrier (BBB). Endothelial cells form the innermost layer, whilst the middle layer is mainly made up by smooth muscle cells, and the outer layer predominantly comprises elastin and collagen (Yuan and Rigor, 2011, Payne, 2017).

As shown in Figure 2.5, different blood vessels possess various thickness of the three layers depending on their functional properties and roles: arteries have thick walls with a large proportion of muscle cells, due to the blood pressure in arteries being high; capillaries are absent the smooth muscle cells due to the blood pressure in these vessels being lower than in arteries and arterioles. Veins and venules also have a thinner wall than arteries and arterioles, since the blood pressure is much lower.

The BBB is formed by three cellular elements of the brain microvasculature: endothelial cells, astrocyte end-feet, and pericytes (PCs) (Ballabh et al., 2004). Tight junctions (TJs) are presented between the cerebral endothelial cells and create a diffusion barrier. The BBB is able to regulate essential nutrients, ions, neurotransmitters, macromolecules and

neurotoxins (Abbott et al., 2010). Small molecules such as oxygen and carbon dioxide supporting the cellular respiration diffuse freely across the BBB. The transport for other substances, for instance, glucose transporter 1 (GLUT1) for glucose is regulated by transporter proteins. The BBB is now known to be regulated dynamically to meet the transport requirements in local brain tissues (Abbott et al., 2010).

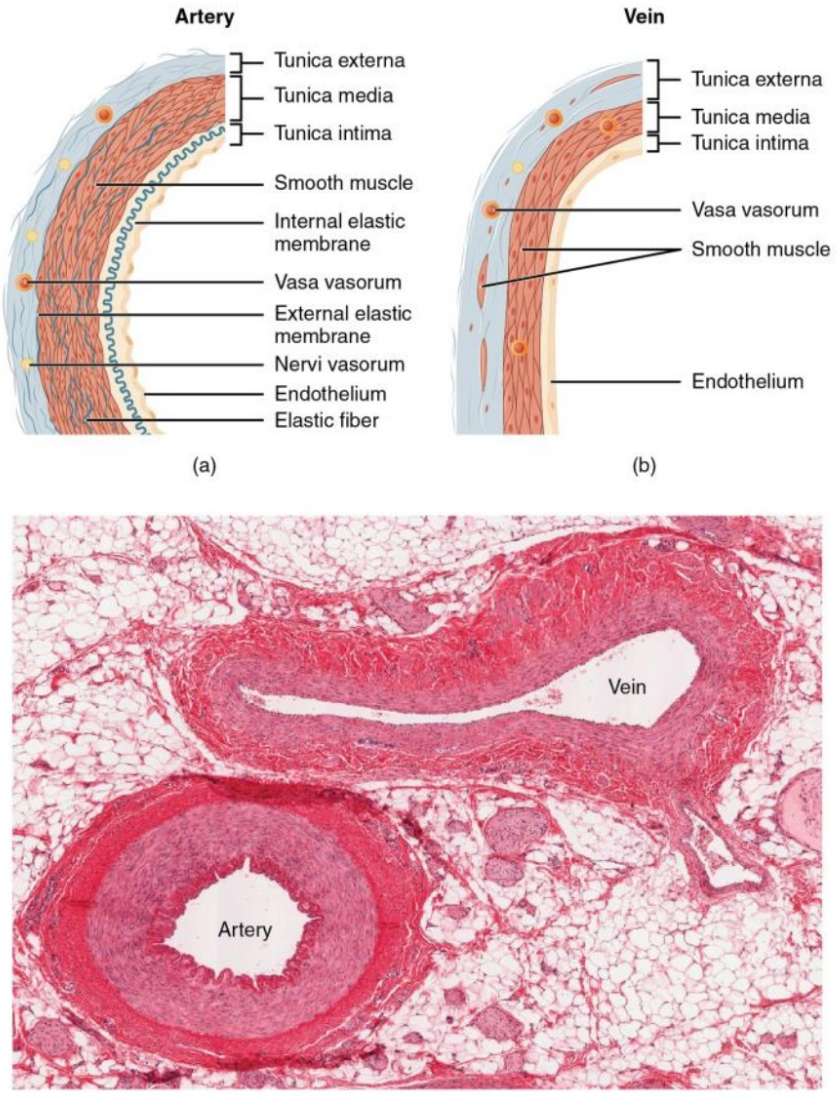


Figure 2.5 Schematic structure of the (a) artery wall; (b) vein wall; artery and (c) vein wall. All figures are reproduced without changes from OpenStax College under license http://creativecommons.org/licenses/by/3.0/. This file can be shared freely under the Creative Commons Attribution 3.0 Unported license.

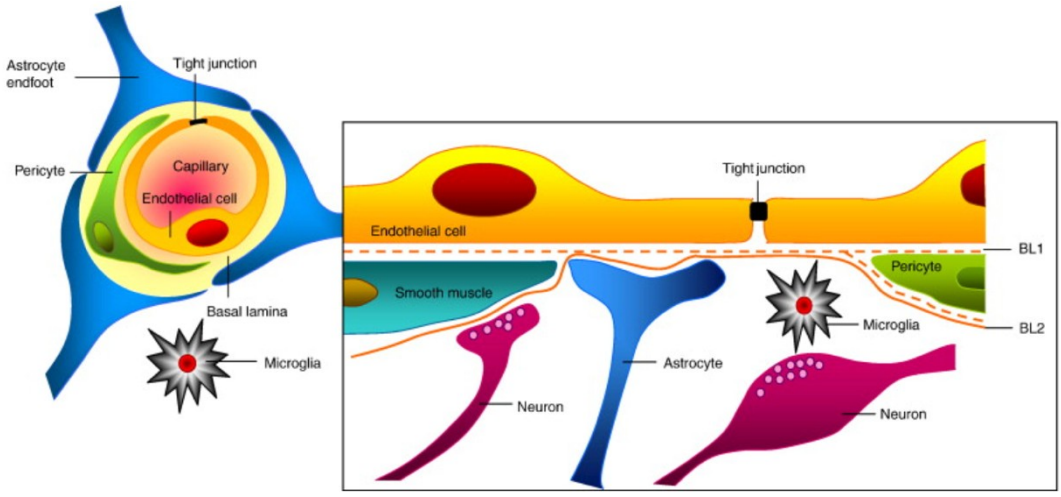


Figure 2.6 Schematic structure of the cell associations at the blood brain barrier (BBB). BL represents basal lamina. This figure is reproduced from Abbott et al. (2010).

Figure 2.6 shows that the cerebral endothelial cells form tight junctions at their margins which seal the aqueous paracellular diffusional pathway between the cells. Pericytes are distributed discontinuously along the length of the cerebral capillaries and partially surround the endothelium. Both the cerebral endothelial cells and the pericytes are enclosed by, and contribute to, the local basement membrane which forms a distinct perivascular extracellular matrix (basal lamina 1, BL1), different in composition from the extracellular matrix of the glial endfeet bounding the brain parenchyma (basal limina 2, BL2). Foot processes from astrocytes form a complex network surrounding the capillaries and this close cell association is important in induction and maintenance of the barrier properties. Axonal projections from neurons onto arteriolar smooth muscle contain vasoactive neurotransmitters and peptides and regulate local cerebral blood flow. Microglia are the resident immunocompetent cells of the brain. The movement of

solutes across the BBB is either passive, driven by a concentration gradient from plasma to brain, with more lipid-soluble substances entering most easily, or may be facilitated by passive or active transporters in the endothelial cell membranes.

Molecules transported by the BBB are influenced by physiological and pathophysiological condition, such as stroke, trauma, Alzheimer's disease, multiple sclerosis, Parkinson's disease and brain tumours (Payne, 2017). BBB rupture may occur after approximately 2 hours after the onset of ischaemia (Brouns and De Deyn, 2009), with the activation of matrix metalloproteins (MMP) leading to a reversible degradation of the tight junctions proteins. This process is described in Section 2.3.2 in more detail.

Meanwhile, the concept of intracranial compliance should be noted briefly here. Intracranial pressure (ICP) (P_{ICC}) is dependent on homeostatic intracerebral volume (V_{ICC}) regulation, which is governed by the Monro-Kellie doctrine, which describes the constant total volume constraint that governs the parenchyma, cerebrospinal fluid and blood within the cranium of the skull (Kim et al., 2012, Monro, 1783). Intracranial pressure is the pressure exerted by cerebrospinal fluid (CSF) within the brain and on the brain tissue, which is normally found to be in the range of $7-15\,mmHg$(Steiner and Andrews, 2006). Intracranial compliance (ICC) represents the change in volume (ΔV_{ICC}) per unit change in pressure (ΔP_{ICC}) and is exactly the inverse of elastance.

When there is a reduction in driving blood pressure, vessel radius will tend to decrease, thus leading to an increase in resistance and hence a reduction in flow caused by both a drop in driving pressure and an increase in resistance. This is known as the passive response and in healthy autoregulation this is counterbalanced by the active (myogenic)

response. The active response acts to increase the vessel radius (the process known as vasodilation) in response to a drop in driving pressure.

Eide and Sorteberg (2007) found that mean ICP wave amplitude was significantly higher in recordings with mean ICC $\leq 0.5\,ml/mmHg$ than recordings with mean ICC ¿$0.5\,ml/mmHg$, while mean ICP wave amplitude was significantly lower in recordings with mean ICC $1.51-3.0\,ml/mmHg$ than recording with mean ICC $\leq 1.50\,ml/mmHg$. As compared to recordings with mean ICC ¿$1.5\,ml/mmHg$, mean ICP was significantly higher in recordings with mean ICC¿$0.5\,ml/mmHg$ or mean ICC $0.5-1.0\,ml/mmHg$. Strong correlations between ICP amplitude and mean ICP with ICC were found.

2.2 Stroke Pathology

2.2.1 Stroke

Stroke is one of the leading diseases that cause death and disability globally. This disease affects both the brain and body functions (Association, 2018). The data collected by the Stroke Association show that there are more than 100,000 strokes each year in the UK and approximately 17 million new stroke patients over the world (Association, 2016).

There are two main types of stroke based on their physiology, ischaemic stroke and haemorrhagic stroke. The first type is caused by a blockage of a major blood vessel to cut off the blood supply to specific brain regions. Blood clots and other materials in the bloodstream (e.g., fatty deposits) can cause a blockage of a major blood vessel. The resulting damage depends on the blockage location, due to different brain function territories being located differently. The second type of stroke is due to disruption of the

blood vessel wall, leading to blood leakage and increase in intracerebral pressure. Haemorrhagic stroke is normally more severe than ischaemic stroke and has a higher risk to patients of dying both within the first three months and beyond. Around 10% of haemorrhagic stroke patients die before they are transported to hospital (Party, 2012). Stroke statistics show that approximately 85% of all strokes are ischaemic stroke and 15% are haemorrhagic stroke (Party, 2012).

The most significant factor predicting stroke is age (Carandang et al., 2006). Meanwhile, gender is another critical factor for stroke. Although women have longer life expectancy than men, the risk of stroke for women is higher over their lifetime (Carandang et al., 2006). The proportion of haemorrhagic stroke is also higher for women (Niewada et al., 2005). The physiology mechanisms of gender that cause different risk of stroke are still unclear (Gibson, 2013). Meanwhile, some pre-existing conditions and lifestyle habits, such as hypertension, atrial fibrillation, high cholesterol diabetes and smoking are all additional risk factors for stroke.

2.2.2 Ischaemic Stroke

Ischaemic stroke is the most common stroke type and is caused by a blockage of a blood supply vessel. If brain tissue cannot obtain sufficient nutrient supply from the blood supply, it will be starved of oxygen and may proceed to necrosis or apoptosis inevitably. Necrosis is the death of tissue, caused by a reduction in blood flow to the tissue. Apoptosis is considered as a process of programmed cell death. However, excessive apoptosis can be caused by various ischemia-associated injuries. One example is

myocardial ischaemia caused by an insufficient blood supply, leading to a decrease in oxygen delivery to the cardiomyocytes and subsequent death of cells (Elmore, 2007). Ischaemic strokes are classified by Adams et al. into five groups (Adams Jr et al., 1993):

1. Large-artery atherosclerosis (embolus/thrombosis)
2. Cardioembolism (high-risk/medium risk)
3. Small-vessel occlusion (lacune)
4. Stroke of other determined aetiology
5. Stroke of undetermined aetiology
    5.a. Two or more causes identified
    5.b. Negative evaluation
    5.c. Incomplete evaluation

Regarding large-artery atherosclerosis ischaemic stroke, fats, cholesterol and other substances build up on and in the artery walls (Arenillas and Álvarez-Sabín, 2005), then the blood flow is restricted. The second type of ischaemic stroke is due to heart pumping unwanted substances to the brain and then cause occlusions in the blood vessels (Ferro, 2003). The lacunes are cavities in the basal ganglia or white matter that are filled with 3 to 15 mm CSF and not clearly associated with specific neurological symptoms (Wardlaw, 2008). “Lacunar stroke” is a clinical ischaemic stroke syndrome with specific symptoms and signs and refers to a small subcortical and brainstem lesion. Lacunar infarcts are small infarcts and constitute up to 25% of all ischaemic strokes (Boiten and Lodder, 1991). The fourth type of ischaemic stroke includes some rare

causes of stroke and the fifth category essentially comprises the residue, where no specific single cause can be determined.

Ischaemic stroke is emphasised in this thesis due to the proposed HT model being based on ischaemic stroke and focusing on post-ischaemic haemorrhage. This model is a particular leakage model and not suitable to simulate haemorrhagic stroke, which is associated with a rupture of a large blood vessel, i.e., a large amount of blood moves to tissue from blood vessels.

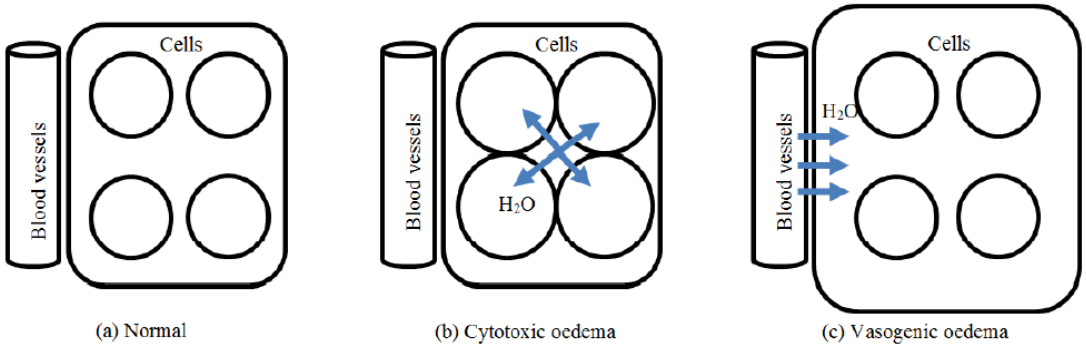


Figure 2.7 Two types of oedemas. (a) normal conditions; (b) cytotoxic oedema occurs when the water accumulates from extracellular space into the cells due to osmotic pressure imbalance; (c) vasogenic oedema occurs when the water from blood vessels enters the extracellular space due to BBB disruption (Mokhtarudin, 2016b).

In addition, cerebral oedema commonly occurs after ischaemic stroke onset (Raslan and Bhardwaj, 2007). Two types of oedemas are shown in Figure 2.7, cytotoxic oedema and vasogenic oedema. One of the consequences of BBB breakdown is vasogenic oedema. As the BBB breaks down, its permeability increases, allowing protein plasma to filtrate through the capillary into the interstitial space (Kimelberg, 2004, Unterberg et al., 2004). This later creates an osmotic gradient which causes excess water movement from the capillary into the interstitial space, resulting in vasogenic oedema. Vasogenic oedema

causes a water content expansion in the brain tissue space, brain tissue swelling and also an increase in the ICP.

The other type of oedema is known as cytotoxic oedema, usually coexisting with vasogenic oedema. This involves the accumulation of water in the astrocyte and neuron but is mostly seen to occur in the astrocyte (Kimelberg, 2004, Unterberg et al., 2004). Being different from vasogenic oedema, cytotoxic oedema occurs not due to BBB disruption or an increase in the BBB permeability, but due to the imbalance of osmotically active solutes between the astrocyte and the extracellular space.

Cerebral oedema is known as excess accumulation of fluid in the brain, causing an increase in intracranial pressure. This disease can lead to impaired nerve function and compress both the brain tissue and blood vessels. Symptoms of cerebral oedema are dependent on the location of oedema, but can include headaches, nausea, visual disturbances, seizures, vomiting, drowsiness, dizziness, and in severe cases, coma and death (Leinonen et al., 2018).

2.2.3 Treatment of Ischaemic Stroke

The treatment for ischaemic stroke has improved significantly in recent decades. However, the process of translation that applies a new treatment to ischaemic stroke from animal experiments to in humans vivo is slow and difficult and the medical trial cost is high. Thus, the number of drugs for ischaemic stroke is limited and today only recombinant tissue-plasminogen activator (rt-PA) is known to be effective for

thrombolytic therapy (O'Collins et al., 2006). rt-PA has the ability to break down the blood clots by catalysing the transformation of plasminogen to plasmin.

rt-PA (also known under its trade name, alteplase(Lees et al., 2010)) was first licensed in North America in 1996 and in Europe in 2002, initially only when used within 3 hours of stroke onset and with a number of conditions. As evidence has grown, the use of rt-PA has been extended, with the 'window of opportunity' later being extended to 4.5 hours after onset (Lees et al., 2010). A meta-analysis, Wardlaw et al. (2012), of 12 trials with 7012 patients found that the application of intravenous rt-PA within 6 hours increased the proportion of both those patients who 238 were alive with favourable outcome and also of those patients who were alive and independent. It was also shown that the benefit was greatest in those patients treated within 3 hours and that there was a similar benefit in patients aged over 80 years old compared to those aged under 80 years, in particular when treated early.

However, there are side effects led by rt-PA, such as the increased risk of haemorrhage, which is due to the change of the permeability of the BBB with the development of cerebral oedema (Kassner et al., 2009). Tsuji et al. reported that Ischaemic MMP-9 levels and brain oedema were significantly lower in rt-PA knockout mice than wild type mice subjected to transient focal ischaemia (Tsuji et al., 2005). It was also suggested that MMP-9 could be involved in BBB dysfunction after rt-PA treatment (Copin et al., 2011) and this phenomenon is discussed in Section 2.3.3 in more detail.

rt-PA was identified as an efficient drug for the ischaemic stroke treatment with a strict "window time", within 3 hours of symptom onset, when first developed. Then the

European Cooperative Acute Stroke Study III investigated the cost-effectiveness of treatment within 3 to 4.5 hours after symptom onset with adding a dose of 0.9mg/kg to 1.1mg/kg (Hacke, 1997, Boudreau et al., 2013). A recent study by Wardlaw et al. described that the odds of survivors and independence after rt-PA treatment increased significantly in 12 trials (7012 patients).

However, the risk of leading to haemorrhage by rt-PA is not the only disadvantage in clinical treatment, and the “no reflow” phenomenon has also been reported. This phenomenon describes the failure of re-perfusion to acute ischaemic regions in the microcirculation (Ames et al., 1968). The cause of this phenomenon remains controversial: Ames at al. reported that astrocyte endfoot swelling resulted in capillary blockage (Chiang et al., 1968); Attwell et al. stated it had been attributed to a failure of arteriolar vasodilation mechanisms (Attwell et al., 2010); Yemisci et al. (2009) suggested that pericyte damage causes this phenomenon. Finally, Heusch et al. (2009) reported that inflating an angioplasty balloon or deploying a stent within an atherosclerotic plaque that has ruptured and resulted in an overlying thrombus may result in a shower of emboli composed of atherosclerotic debris or thrombotic material in humans (Heusch et al., 2009). These emboli can then result in additional microvascular occlusions above and beyond those due to endothelial swelling and disruption observed in animal models with normal coronary arteries. These emboli could not only block flow mechanically but could result in vasospasm (Kloner, 2011). Vasospasm is defined as inappropriate constriction or insufficient dilatation in the microcirculation, reducing the amount of blood that can flow through it (Flammer et al., 2001). Vasospasm is an important

complication of subarachnoid haemorrhage (Frontera et al., 2009). More than half of the treated patients were found to develop a syndrome of focal and/or cognitive deficits due to cerebral vasospasm between the fourth and ninth day after the subarachnoid haemorrhage. At the end, many died or suffered permanent morbidity, and it has been found as the single most important cause of morbidity and mortality in patients whose ruptured aneurysm was successfully treated (Pluta et al., 2009).

Another treatment for ischaemic stroke is mechanical thrombectomy. This alternative therapy method is approved to be safe and effective for acute ischaemic stroke with proximal anterior circulation occlusion within 6 hours after onset (Bourcier et al., 2019, Berkhemer et al., 2015, Saver et al., 2015, Jovin et al., 2015, Campbell et al., 2015). Mechanical thrombectomy is commonly applied in conjunction with recombinant tissue-plasminogen activator (rt-PA) treatment. Pan et al. investigated the benefit conferred by the treatment by estimating the cost per quality-adjusted life-year gained in the long term (30 years) in China and summarized that the mechanical thrombectomy is cost-effective in China and other low-income and middle-income countries (Pan et al., 2018).

2.3 Haemorrhagic Transformation Physiology

Haemorrhagic transformation (HT) is a significant complication of ischaemic stroke, causing bleeding in the brain and is a significant clinical concern (Castellanos et al., 2003). The occurrence of haemorrhagic transformation (HT) is frequently associated with multiple factors including age, historical records of medical conditions such as diabetes or hypertension, previous utilization of antihypertensive medication, along

with the levels of systolic blood pressure (SBP) and glucose in the body (van der Steen et al., 2022, van Kranendonk et al., 2019). However, certain indicators were observed to lack an independent correlation with the incidence of Hematoma Transformation (HT), one example being the presence of enlarged perivascular spaces. (Song et al., 2021)

HT is classified into two types based on the use or otherwise of thrombolytic therapy:

1. Spontaneous haemorrhagic transformation (absence of thrombolytic therapy)
2. Secondary haemorrhagic transformation (treated by thrombolytic therapy)

Both types of HT are due to the disruption of the BBB. Specific differences between these two types of HT are introduced in this section.

Spontaneous haemorrhagic transformation is less well-understood than the second type of HT. Tan et al. reported that the ratio of spontaneous HT was observed in 50 out of 407 patients (12.3%) (Tan et al., 2014). Lindley et al. stated that the overall frequency of spontaneous HT in untreated acute ischaemic patients is 8.5% (Lindley et al., 2004).

Regarding the secondary haemorrhagic transformation, many studies have examined the physiology, the frequency, the severity, the factor, the predictor and the treatment of secondary HT after the thrombolytic therapy. The increment of the symptomatic secondary HT is considered as evidence to the side effects of the thrombolytic therapy, based on research showing that mortality and HT in the actively treated groups increase (Donnan et al., 1996, Trial—Italy, 1995, Group, 1996). As introduced in the last section, rt-PA is the only and efficient drug to treat acute ischaemic stroke within a certain “window” (O'Collins et al., 2006).

Recent studies have suggested that the side effects of rt-PA are due to its signalling function and actions in the neurovascular unit (Wang et al., 2004). rt-PA may enlarge potentially excitotoxic calcium currents by interacting with the N-methyl-D-aspartate type glutamate receptor. At certain concentrations, rt-PA may be vasoactive, at low $1\,nmol/L$ concentrations rt-PA inhibits phenylephrine-induced vasoconstriction, whereas at high $20\,nmol/L$ concentrations rt-PA augmented phenylephrine's effects on vessel tone (Nassar et al., 2004). Phenylephrine can result in the constriction of both arteries and veins (Maeso et al., 1996). By increasing matrix metalloproteinase (MMP) dysregulation after stroke, rt-PA degrades extracellular matrix integrity and increases the risks of neurovascular cell dysfunction, blood-brain barrier disruption and oedema (Wang et al., 2000, Asahi et al., 2001, Rosenberg, 2002). Other studies have hypothesised that the HT is due to the absence of the endothelial basal lamina (Hamann et al., 2002).

Accumulating research suggests that HT after thrombolytic therapy is related to the dysregulated extracellular proteolysis within the neurovascular matrix (Lo et al., 2003, Lo et al., 2004, del Zoppo and Mabuchi, 2003). One study has reported that BBB leakage and haematoma volume can be reduced by knocking out matrix metalloproteinases (MMPs) genes in mice (Asahi et al., 2001). Matrix metalloproteinases (MMPs) work as a mediator and are responsible for modelling the majority of matrix substrates in the brain (Yong et al., 2001, Rosenberg, 2002). Meanwhile, MMP inhibitors can also reduce brain oedema after intracerebral haemorrhage (Rosenberg, 2002).

Knockout MMP mice are widely used to determine the interactions of rt-PA and MMPs. Researchers have found evidence that MMP inhibitors reduce both the frequency and severity of rt-PA associated intracerebral haemorrhage, as shown in Figure 2.8 (Sumii and Lo, 2002, Lapchak et al., 2000). Meanwhile, ischaemic brain MMP-9 levels were found to be reduced in rt-PA knockout mice (Wang et al., 2003).

The interactions of rt-PA and MMPs have also been reported in clinical data. MMP-9 levels were determined to be increased in rt-PA treatment patients and the patients whose MMP-9 level was increasing were found to have more severe brain injuries and worse neurological outcome (Castellanos et al., 2003). The application of MMP inhibitors may thus work as a new approach for combination stroke therapy in the future (Wang et al., 2004).

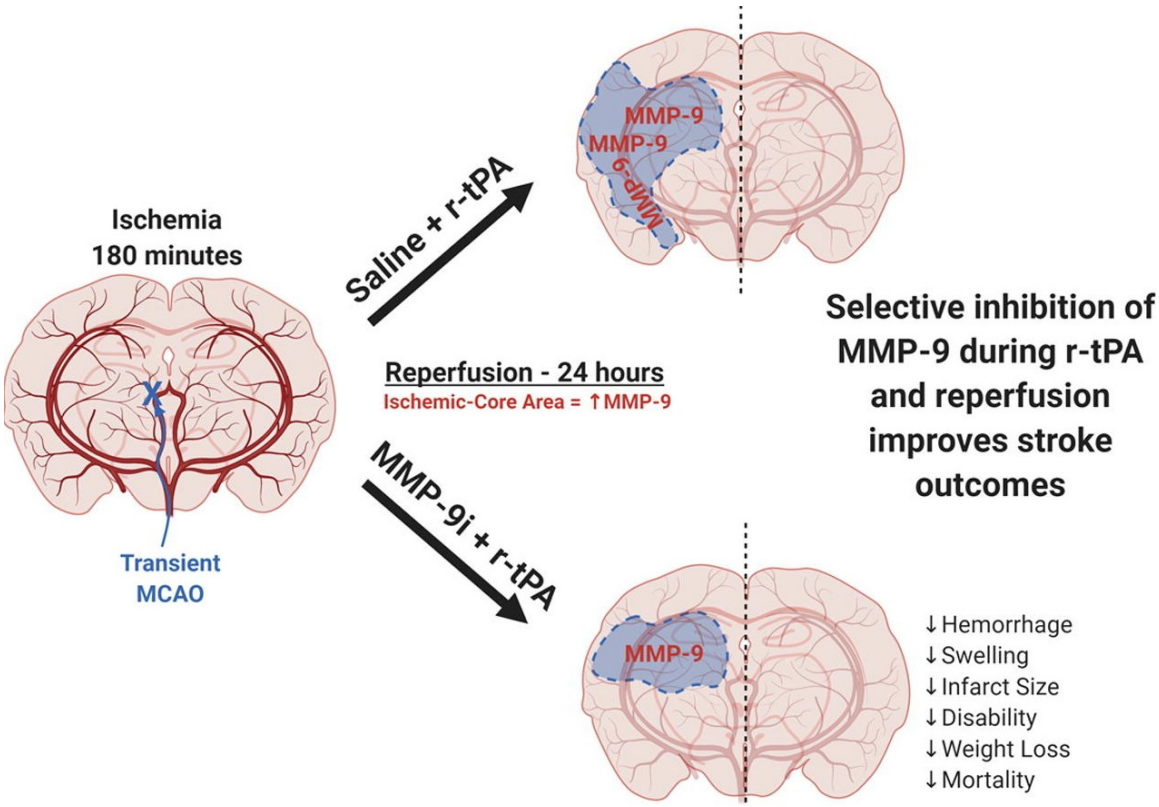


Figure 2.8 MMP-9 inhibitor (MMP-9i) improves stroke outcomes. This figure is reproduced from Saleem et al. (2021).

Regarding the contribution of MMPs to the BBB disruption, as shown in Figure 2.9, promatrix MMP-2 (ProMMP-2) can be activated by membrane-type-1 MMP (MT1-MMP/MMP-14), and the latter can be activated by furin, which is a protease. Promatrix MMP-9 (ProMMP-9) can be activated by MMP-3, rt-PA, proinflammatory factors (e.g., Interleukin 1 beta (IL-1β) and Tumour Necrosis Factor Alpha (TNF-α)), and reactive oxygen species (ROS). Plasmin can activate both MT1-MMP and MMP-3. rt-PA can activate both MMP-3 and MMP-9 through multiple pathways. rt-PA activity can be inhibited by neuroserpin and activated protein C (APC).

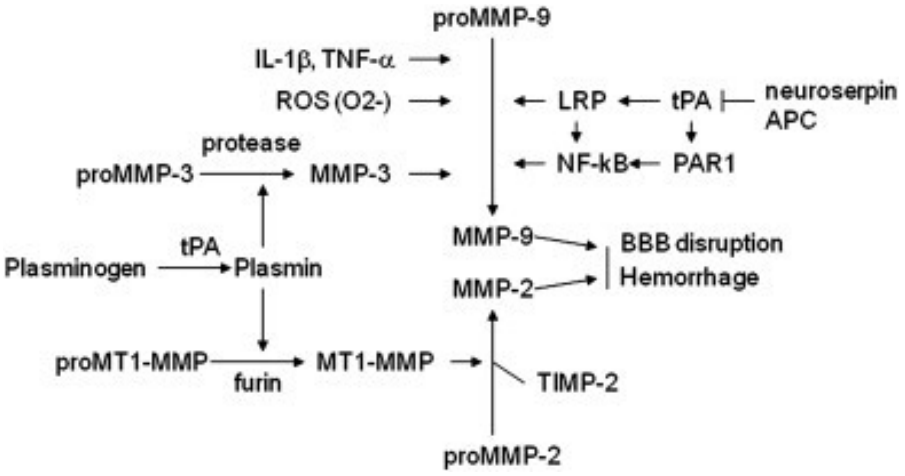


Figure 2.9 Mechanisms of activation of MMPs. Abbreviations: Promatrix MMPs (ProMMPs); Membrane-type-1 MMP (MT1-MMP); proinflammatory factors (e.g., Interleukin 1 beta (IL-1β) and Tumour Necrosis Factor Alpha (TNF-α)); reactive oxygen species (ROS); Activated protein C (APC); Protease activated receptor 1 (PAR1); Receptor-related protein (LRP); Nuclear factor-κB (NF-κB). This figure is reproduced from Jin et al. (2010).

There are various HT classifications methods. First, HT can be classified by the severity of haemorrhage, as proposed by the European Cooperative Acute Stroke Study (ECASS) group, from microcapillary bleeding to extensive haemorrhage (Fiorelli et al., 1999, Del Zoppo et al., 1992):

1. Small petechial haemorrhagic infarction (HI1)
2. Confluent petechial haemorrhagic infarction (HI2)
3. Small parenchymal haemorrhage (PH1, small than 30% of the infarct, mild mass effect)
4. Large parenchymal haemorrhage (PH2, larger than 30% of the infarct, marked mass effect).

The clinical definition is that the petechiae are pinpoint, round spots on the skin as a result of bleeding and the parenchyma is the bulk of functional substances in an organ (brain tissue in this study).

Second, symptomatic and asymptomatic are also considered to describe the different types of HT based on the neurological status (Dzialowski et al., 2007). However, even asymptomatic HT can lead to a reduction of cognition and neurological function assessment (Dzialowski et al., 2007, Park et al., 2012). Motto et al. suggested that this phenomenon is effected by some part to exacerbation of cerebral oedema (Motto et al., 1999). Hence, it is important to reduce the volume of haematoma after HT (Jickling et al., 2014).

Third, Heidelberg Bleeding Classification was established in 2015, which is used to standardize the classification scale for symptomatic intracranial haemorrhages (sICHs) (von Kummer et al., 2015). Heidelberg Bleeding Classification avoids being overinclusive for SICHs and provides a formal method for categorizing the likelihood of an intracranial haemorrhage being symptomatic that can be applied in various trial and care settings.

Table 2.1 Anatomic description of intracranial haemorrhages (Heidelberg Bleeding Classification).

Class	Type
1	Haemorrhagic transformation of infarcted brain tissue
1a	Small petechial haemorrhagic infarction, HI1
1b	Confluent petechial haemorrhagic infarction, HI2
1c	Small parenchymal haemorrhage, PH1 (small than 30% of the infarct, mild

	mass effect)
2	Large parenchymal haemorrhage, PH2, (larger than 30% of the infarct, marked mass effect).
3	Intracerebral haemorrhage outside the infarcted brain tissue or intracranial-extracerebral haemorrhage
3a	Parenchymal haematoma remote from infarcted brain tissue
3b	Intraventricular haemorrhage
3c	Subarachnoid haemorrhage
3d	Subdural haemorrhage

2.4 Vasculature models

2.4.1 Poiseuille's Law

For an individual vessel, the driving force is the pressure difference between the inlet pressure and outlet pressure (Vander et al., 1998). Regarding a network vasculature model, the driving force is the difference between the mean arteriole pressure and mean venule pressure.

The flow resistance R_{res} is defined by the ratio of pressure difference ΔP and the flowrate Q:

$$R_{res} = \frac{\Delta P}{Q} \tag{2.1}$$

The resistance of flow is governed by the Hagen-Poiseuille relationship and depends on the length of the vascular vessel L, blood flow viscosity $\mu$and the diameter of the blood vessel D (Vander et al., 1998):

$$R_{res} = \frac{128 L \mu}{\pi D^4} \quad (2.2)$$

The assumptions of the Hagen-Poiseuille equation are that the flow is incompressible and Newtonian. The blood flow should be laminar and the vessel is assumed to be straight, rigid and a cylinder structure with constant diameter.

The blood flow in the brain can be assumed as laminar flow and the maximum Reynolds number for brain blood flow is approximately 200 (Moore et al., 2005). In tubes where the internal diameter is large compared with red blood cell diameter, blood behaves essentially as a Newtonian (incompressible) fluid. The correlation between vessel diameter and blood viscosity will be discussed in the next section.

2.4.2 Viscosity

Viscosity is essential to a vasculature model. Pries et al. (1992) reported that the viscosity is only proportional to the haematocrit of the blood in large vessel. However, in small vessels, the viscosity is strongly dependent to the diameter of the blood vessels. This viscosity change is due to the same magnitude order of the diameter of red blood cell and diameter of small capillaries in the vasculature model. A small number of blood cells in the small blood vessel leads to interaction between the cells and the vessel wall. It was first reported by Fåhræus and is known as the Fåhræus–Lindqvist effect: when the vessel wall diameter is lower than $1\,mm$, the viscosity decreases but increases in the range of $5-7\,\mu m$(Dintenfass, 1967). To calculate the blood viscosity in small vessels, Pries and Secomb and colleagues developed some empirical equations based on experiments (Secomb and Pries, 2013, Pries et al., 1994).

Figure 2.7 shows the relationship of relative blood viscosity with the vessel diameter and haematocrit based on the empirical relationship given by Eq. (2.3):

$$\mu_{\Re l}=1+\left(\mu_{0.45}-1\right)\frac{\left(1-H_D\right)^C-1}{\left(1-0.45\right)^C-1} \tag{2.3}$$

where

$$\mu_{0.45}=220\,e^{-1.31D}+3.2-2.44\,e^{-0.06\,D^{0.645}} \tag{2.4}$$

and

$$C=\left(0.8+e^{-0.075\,D}\right)\left[-1+\left(1+10^{-11}D^{12}\right)^{-1}\right]+\left(1+10^{-11}D^{12}\right)^{-1} \tag{2.5}$$

Here the unit of elative apparent viscosity $\mu_{\Re l}$ is represented as cp. $D$is the diameter of the blood vessel and H_D is the discharge haematocrit, which is defined when blood enters the venules increasing in haematocrit.

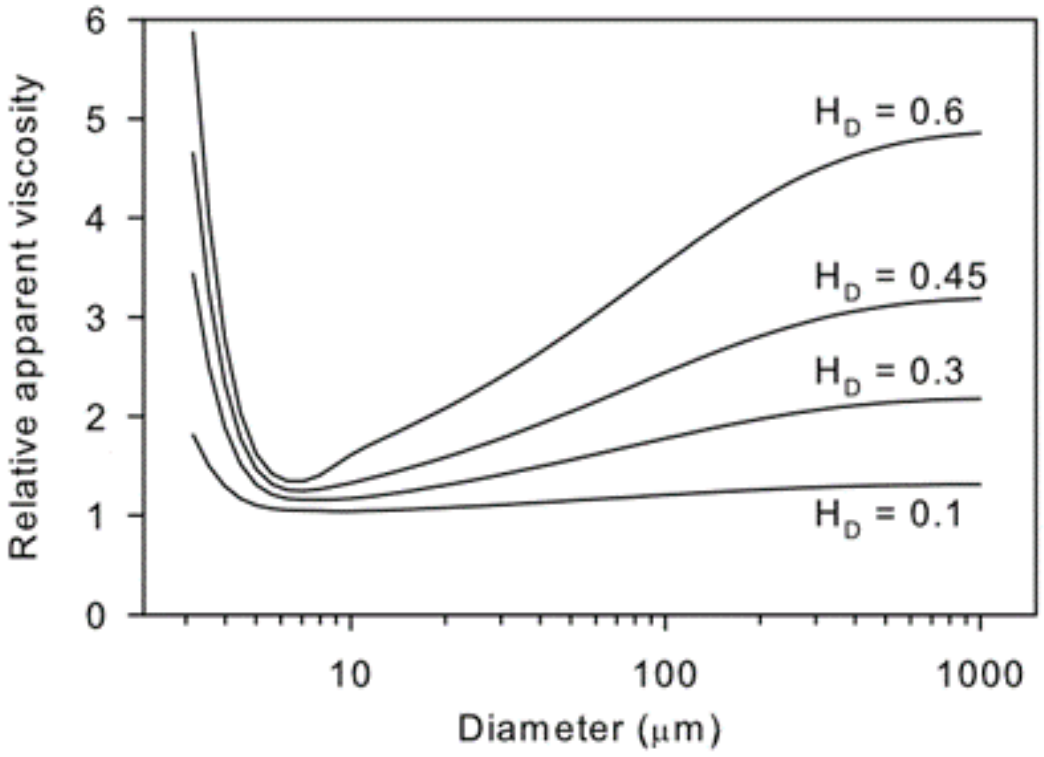


Figure 2.10 Dependence of the blood relative apparent viscosity of vessel diameter and haematocrit (Secomb and Pries, 2013).

2.4.3 Vascular Model

It is perhaps surprising that there is a long history of models of the network of large arterial vessels, despite the difficulties of extracting information from human subjects and of solving the model equations. Early models were mostly developed based on physical analogues (Avman and Bering, 1961, Murray, 1964, Hillen et al., 1988).

Nowadays, the development of a model can be based on patient imaging data. Cebral et al. (2002) used MRI data to reconstruct the anatomy of the Circle of Willis. Moore et al. (2005) developed a Circle of Willis 1D model, including efferent and afferent arteries, as shown in Figure 2.11. A sign convention for flow around the circle is displayed. Afferent and circulus arteriosus are shown with constant resistances, as it is assumed that smooth muscle cell induced constriction and dilation of the artery walls does not occur to a significant degree in large, relatively rigid cerebral arteries. The model uses the Poiseuille flow approximation: the flow rate can be changed significantly due to the change of resistance, which is affected by the diameters of the blood vessels.

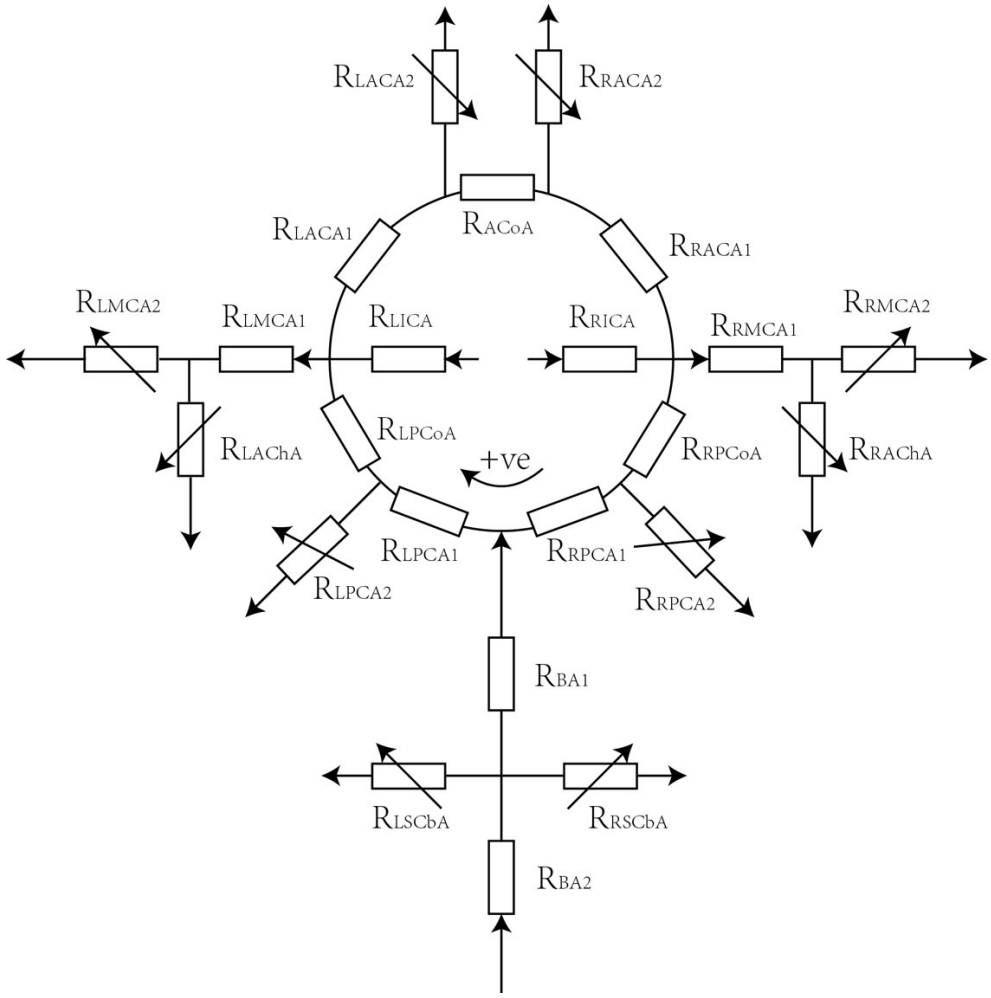


Figure 2.11 Schematic representation of the Circle of Willis for a 1D model. This figure was redrawn from Moore et al. (2005) to improve the resolution.

It is worth noting that the validation process confronts substantial challenges, notably concerning the accuracy of model generation, the wall material properties, and the intricacies of haemodynamics. Thus, recent models have combined the imaging techniques and the simulations of fluid flow by the 3-D Navier-Stokes equation (Moore et al., 2006, Moore and David, 2008, Khodaee et al., 2016, Reorowicz et al., 2014).

It is notable that since some models only consider the large arterial vessels, assumptions need to be set about the remainder of the vasculature. Some models set the outlet

pressure at the end of large arterial vessels and other models set the boundary conditions in a more simplified manner.

An integrated vascular model is described by a set of physical relationships that depict three connected, compliant, vascular compartments (namely the arterial, capillary, and venous compartments) and a constant volume compartment to model the pial venous structure (Buxton and Frank, 1997, Buxton et al., 1998). These models were extended to include an empirical description of vascular compliance in the Windkessel model (Mandeville et al., 1999b, Mandeville et al., 1999a).

The vascular compartments can be described by an analogy to connect a circuit of resistor and capacitor (electrical) elements as depicted in Figure 2.12 (Mandeville et al., 1999b). Cerebral blood volume is equivalent to electrical charge. The flow of charge (i.e., current) models blood flow and is proportional to the blood pressure drop across compartments and inversely proportional to vascular resistance. Nonlinear capacitor elements model the vascular compliance of each compartment and the relationship between the cross-sectional area of a vascular segment and its vascular resistance (Huppert et al., 2007).

The resulting differential equations from the Windkessel model that govern changes in blood flow and volume are caused by the active dilation of the arteries, which reduces the input vascular resistance of the system. The pressure gradient between compartments (analogous to electrical potential difference) drives the flow of blood (equivalent to electrical current) between compartments. As the pressure increases, the vascular compartment expands causing blood volume to increase. The increase in blood

volume in a compartment is equivalent to the build-up of charge on a nonlinear capacitor, whose capacitance decreases as the compartment expands against the pressure of the surrounding brain, leading to a saturating blood volume expansion function. Eventually, the heart and systemic circulation create a constant pressure drop across the entire system and are modelled as a single constant direct current voltage source.

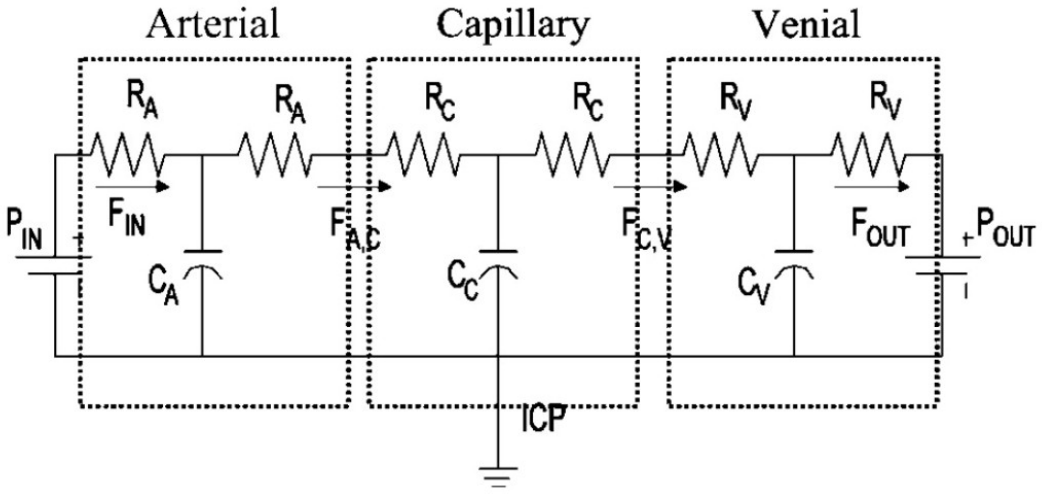


Figure 2.12 Schematic of the Windkessel vascular model: The Windkessel vascular model can be described based on an analogy to the electrical circuit shown here. Cerebral blood volume is equivalent to electrical charge. The flow of charge (i.e., current) models blood flow changes and is proportional to the blood pressure drop across compartments and inversely proportional to vascular resistance. Nonlinear capacitor elements model the vascular compliance of each compartment and the relationship between the cross-sectional area of a vascular segment and its vascular resistance (Huppert et al., 2007).

2.4.4 Microvasculature Models

Microvasculature models have been highly used in haemodynamics simulations over the last ten years. Most of the microvasculature models which were created before that time were limited by the lack of information about the geometry of the network. The

studies that have been performed over the last 10 years can be divided into 1D or 3D. Note that the 1D models do not consider the spatial nature of either the network or the tissue, see for example Niimi et al. (Niimi et al., 2006) and Huppert et al. (Huppert et al., 2007).

A representative segment model of microvasculature has been developed by Boas et al. (2008) based on an earlier geometric model by Quick et al. (2000). The basis for the model is a set of vessels with length and diameter arranged in such a way as to distribute flow with vessels modelled by resistors, as shown in Figure 2.13. Boas uses a two-dimensional branching model with each parent vessel branching into two identical vessels (for arterioles) or the reverse for venules.

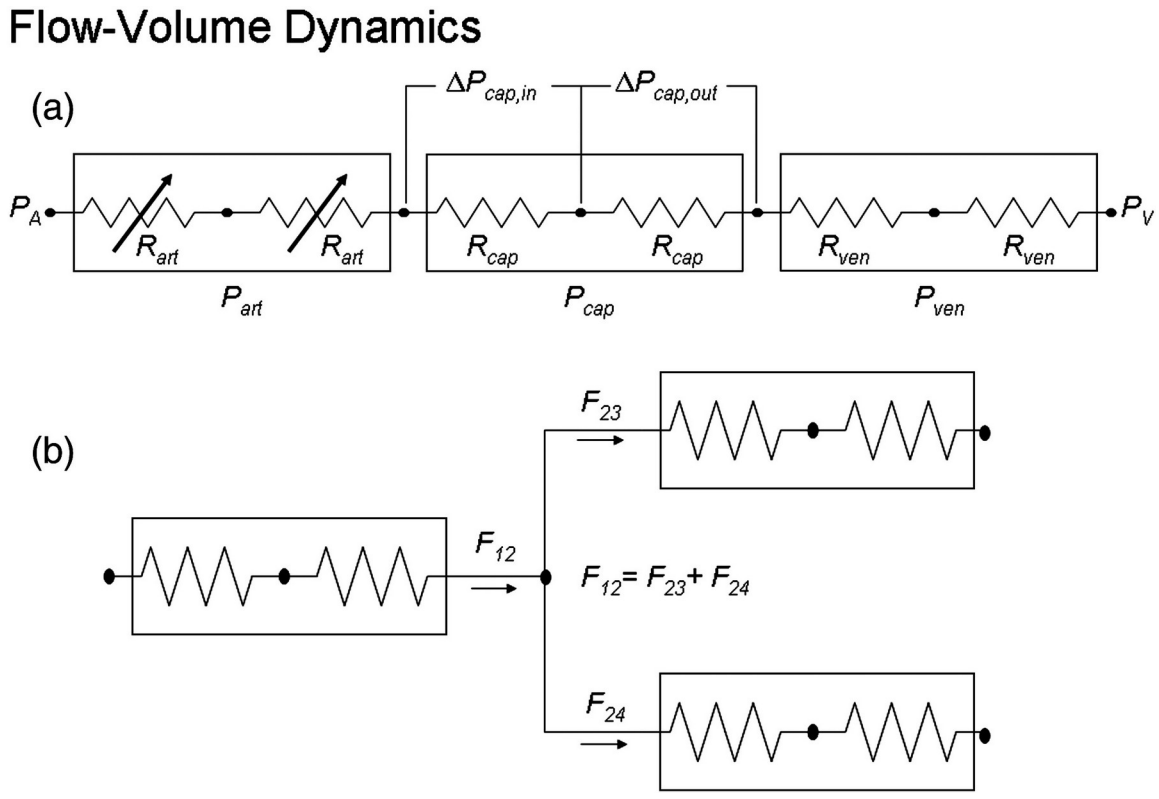


Figure 2.13: Branching resistor showing conservation of flow as voltage and resistors representing vessels from Boas et al. (2008).

The geometry of the Boas model is obtained from experimental data from Zweifach (1974) with a 20% diameter decrease in arterioles per branch. The venule diameter increases by 20% per branch with larger venules than arterioles, representative of the vasculature. The length of capillary vessels is $250\,\mu m$ and of all other vessels $100\,\mu m$. Using this vascular network, it is possible to predict the blood pressure and haemoglobin oxygen saturation at different generations of the arterioles, capillaries, and venules. However, the resulting velocity values are higher than found in vitro.

A similar 1D vasculature model was proposed by Payne and Lucas in 2010 to model oxygen circulation (Payne and Lucas, 2018, Lucas and Payne, 2010). They used the Boas et al. model as a starting point (Boas et al., 2008). As shown in Figure 2.14, 13 generations of blood vessels include 6 arteriolar vessel generations, 1 capillary vessel generations and 6 venule generations (Payne and Lucas, 2018). There are 128 nodes that connect 220 vessels and successive arteriolar generations are referred to A1: A6, capillary C and venule generation V1 to V6. Vessels in the same generation are assumed to have the same mechanical parameters, such as diameter, length, stress, etc. This model will be applied to this haemorrhage model to compare the haemorrhage in different generations in this thesis.

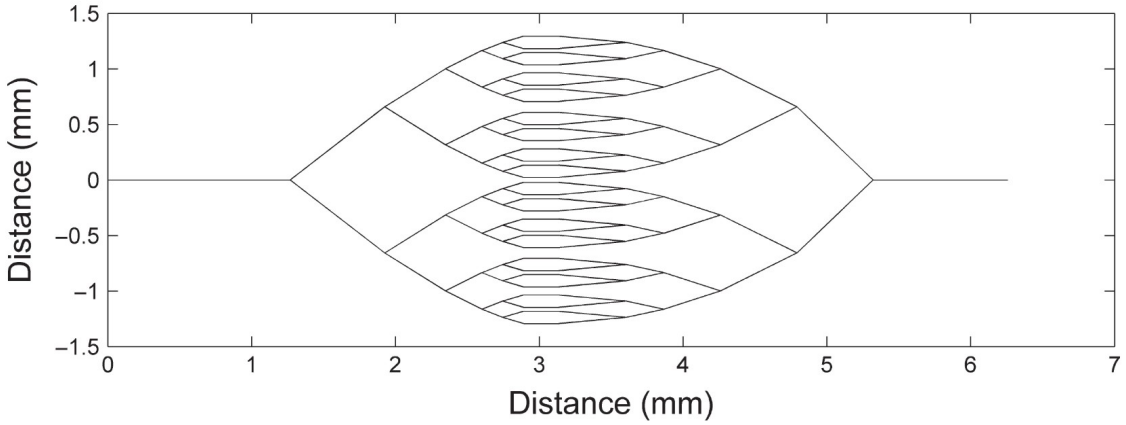


Figure 2.14: Payne and Lucas model of 2D vasculature model to simulate oxygen circulation (Payne and Lucas, 2018).

Pozrikidis and Farrow (2003) developed a model of the vasculature with 4 branching capillaries, one arteriole and one venule to model the fluid flow in tumours. In this simulation, the accurate values of vascular geometry were not considered. Then in 2010, Pozrikidis produced tree-like capillary network models with geometry data and changed the number of generations into three types (Pozrikidis, 2010). However, the limitations of this model are that there are only arterioles and capillary generations without venules, and without the consideration of the interaction of the surrounding vessels.

The purpose of this study requires application of the haemorrhage model on a 3-dimensional capillary network. 3D models in nature tend to come from imaging techniques. This type of model is able to simulate the blood flow within these particular structures and may allow consideration of the interactions affected by surrounding vessels. One limitation of this model type is the difficulty to describe the relationship between the vasculature and the tissue from small samples.

One 3D vasculature model is presented by El-Bouri and Payne in 2015 which comprises a series of 3-dimensional human cerebral microvascular networks applied to multi-scale homogenization methods (cube size from $125\,\mu m$ to $625\,\mu m$) (El-Bouri and Payne, 2015), as shown in Figure 2.15. Another subsequent example of 3D vasculature network is a penetrating vessel model, also produced by El-Bouri and Payne in 2018 to investigate the haemodynamics when there is an occlusion in penetrating vessels (El-Bouri and Payne, 2018), as shown in Figure 2.16. Acosta et al. also produced a method to apply a one-dimensional flow on the distribution of vessels (Acosta et al., 2015). A capillary bed model is developed by a procedure termed 'triangulate-prune-smooth'. Then Voronoi mesh is used to fill the space and modify the network to match the right bifurcation properties and the diameters smoothed. Safaeian et al. (2011) also used a Voronoi mesh in a 2D model and Safaeian and David (2013) later applied this in 3D.

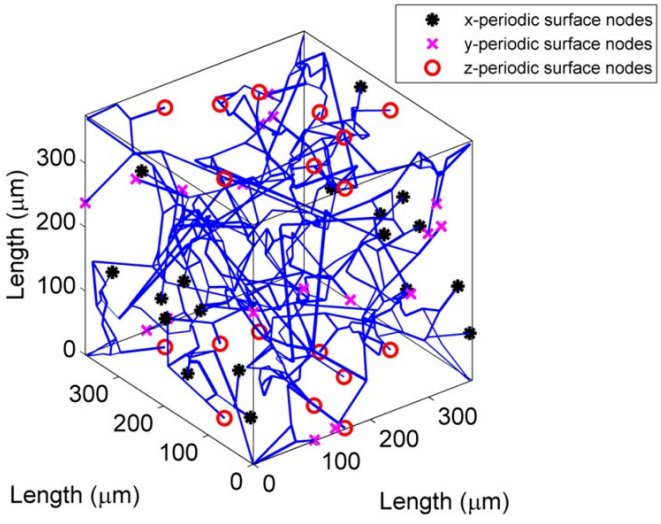


Figure 2.15 Typical cerebral capillary network, generated in a 375 μm cube (El-Bouri and Payne, 2015).

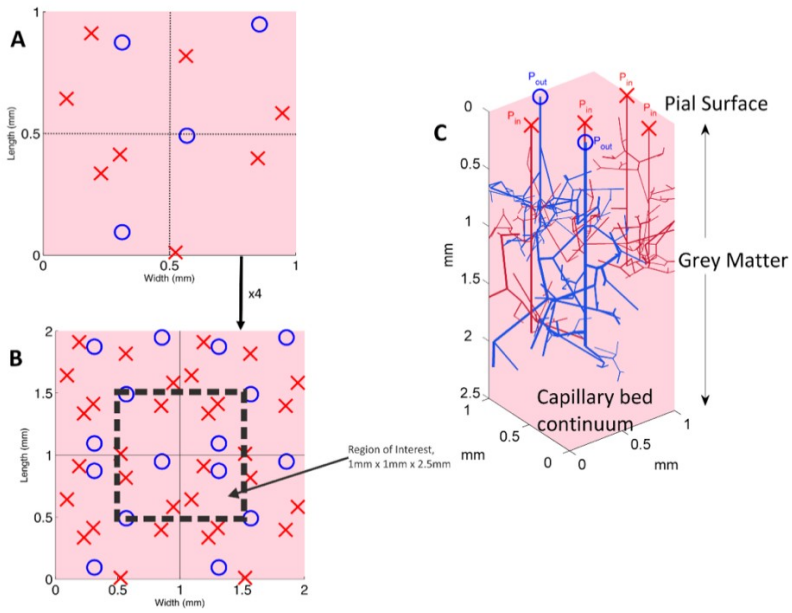


Figure. 2.16 (a) Top-down view of a 1 x 1 x 2.5 mm voxel, split into 4 quadrants each containing 2 arterioles and 1 venule. (b) The same voxel as in (a) repeated 4 times to form a 2 x 2 x 2.5 mm voxel. The region of interest is shown as the black dashed line. (c) An example voxel showing half the penetrating vessels for easier viewing. The penetrating vessels enter from the pial surface into the grey matter, coupling to the capillary bed continuum via the terminal vessels (El-Bouri and Payne, 2018).

2.4.5 Homogenization

A number of vasculature models have been developed, as introduced in previous section. However, the majority of these models are currently only computationally feasible for small tissue sections, other than those of El-Bouri and Payne (2015) and El-Bouri and Payne (2018). Building larger models so that accurate comparisons can be made with imaging data becomes very challenging using current discrete modelling techniques. Boundary conditions of imaged sections are also unknown at present and have been shown to have a strong impact on flow properties (Lorthois et al., 2011). This makes it very difficult to determine the effect of the microvasculature on tissue-scale fluid transport. In order to gain a more comprehensive understanding of the perfusion

and pathophysiological conditions associated with the vasculature, homogenization has been applied.

Homogenization is an averaging technique which derives macro-scale models using micro-scale models, assuming that there is scale separation between the two sizes and that the micro-scale model is periodic. Using such methods results in the discrete micro-scale representation being replaced with averaged integral quantities of the capillary bed valid over the larger region of interest, reducing the computational cost substantially. A key advantage of this continuum approach is that the results are independent of the choice of boundary condition.

Shipley and Chapman (2010) applied these mathematical averaging techniques on a leaky capillary bed to generate an averaged macroscopic Darcy flow model. The permeability tensor of this flow model is what links the capillary-scale topology to macro-scale blood flow model and is the property of interest when scaling up these discrete models. This tensor can be characterized to build larger continuum models of the cerebral microvasculature. The idea of scale separation introduces the concept of a representative elementary volume (REV). This is defined by Bear (1988) as the minimum volume within which the property of interest remains relatively constant. Therefore, determining the REV of a network is important to minimize computation time. The averaging techniques derived by Shipley and Chapman have been previously used by Smith et al. (2014) on a model of non-leaky rat myocardial capillaries. El-Bouri and Payne (2015) thus adapted the discrete model developed by Su (2012) to build periodic,

statistically accurate, 3-dimensional models of the cerebral microvasculature and hence to compute the permeability tensor for the first time.

2.5 Current Brain model

To the best of the author's knowledge, there is no current model describing the HT in a full human brain model. Although 3-dimensional finite element head models have been reasonably widely applied to study the consequences of traumatic brain injury, there are few efforts that have been attempted at the organ (head) scale. For example, Li et al. (2009) used a simplified head model to study the effects of various boundary conditions on the value of ICP, while Mokhtarudin (2016b) used a patient-specific finite element model to validate the mathematical models developed for investigating the effects of ischaemia-reperfusion and the role of a water-transporting protein. However, a direct link between a magnetic resonance informed vasculature and the mechanics of swelling is not fully established.

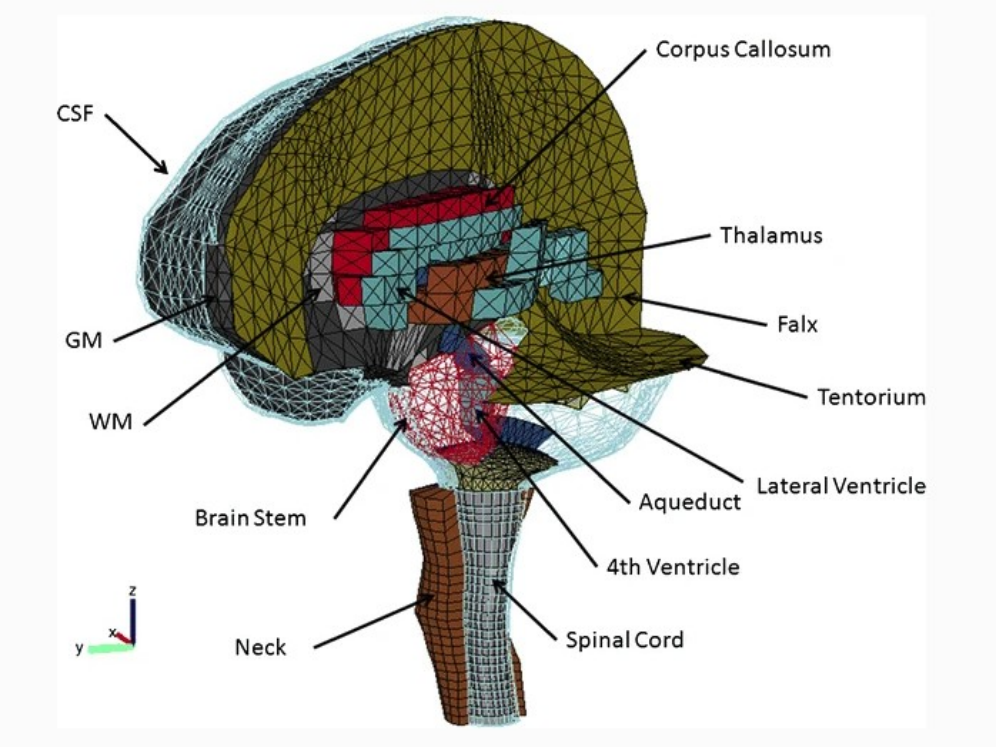


Figure 2.17. A simplified head model produced by (Li et al., 2011)

Various full brain models have been developed, for example, to investigate the correlation between stress and midline shift (MLS) (Bing et al., 2020). One of the most common approaches to study brain tissue deformation is the use of poroelastic theory, which is suitable for modelling long term fluid movement processes (Kyriacou et al., 2002) such as water filtration into the brain interstitial space. Poroelastic theory was first introduced in modelling soil consolidation, which is a process of gradual settlement of soil under loading (Biot, 1941). Further generalisations were made (Biot and Willis, 1957, Biot, 1962a, Biot, 1962b) to incorporate the dynamical behaviour of the porous structure such as the fluid phase acceleration and gravitational forces. Further re-derivations were made (Zienkiewicz, 1982) and also by (Green and Naghdi, 1969), of which the latter is commonly known as mixture theory, to provide alternative

formulations to the constitutive model of the porous solid. Furthermore, the theory was further developed to study the behaviour of fractured rocks that have a double porosity and permeability (Aifantis, 1980), and was later generalised to include multiple porosity and permeability (Bai et al., 1993). The concept of multiple porosity and dynamic behaviour in the poroelastic theory was then applied to study water transport in the cerebral space during hydrocephalus (Tully and Ventikos, 2011). Therefore, this theory is suitable to model brain tissue by assuming the brain tissue to be a homogeneous and linearly elastic material containing water and blood in a porous structure.

The geometry information of the computational brain developed by Bing et al. (2020) was obtained from full-head, high resolution anatomical T1-weighted MR images and TOF MRA images of a 39-year-old healthy female. Using Amira and the FMRIB software library (FSL) (FMRIB Software Library: www.fmrib.ox.ac.uk/fsl; The versions of these algorithms were: BET v. 1.1 from FSL v. 1.3; BSE v. 2.09; AFNI v. 2.29), the structures of the head were segmented (Smith, 2002). The T1-weighted MR images were processed by the Brain Extraction Tool 2 in FSL to extract the inner and the outer skull surfaces which were used as a guideline for the skull segmentation (Smith et al., 2004, Jenkinson et al., 2005). The remaining structures were further segmented manually by Bing et al. (2020) into brainstem, cerebrospinal fluid (CSF), cerebellum, flax cerebri, grey matter, ventricles and white matter. The skin, scalp, muscles and eyes were excluded from the model to save computational time. However, the stroke simulation by using this brain model was compared to a rat model (Garcia-Gonzalez et al., 2018), as shown in Figure

2.18, which was suggested that it could be validated with real clinical image data in the future.

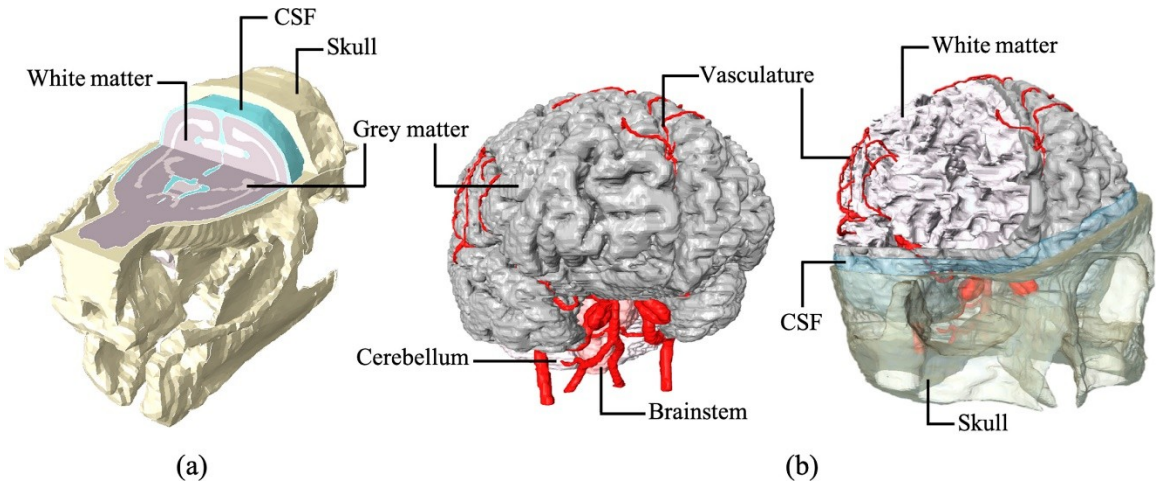


Figure 2.18 Numerical models of rat (a) and human (b) heads. This figure is reproduced from Bing et al. (2020).

Another study of each part of the brain with different constitutive relationships and material properties was proposed by Weickenmeier et al. (2017). They used the ScanIP software environment (Simpleware Ltd. 2006 ScanIP, +ScanFE and +ScanCAD software v. 2.0) to process, segment and reconstruct the magnetic resonance images of an adult female brain to develop the brain model with finite elements. However, this model assumed a homogeneous brain microstructure, homogeneous connective tissue, and a homogeneous cerebrospinal fluid, which could very well display regional variations that will result in heterogeneous effects.

A fully automated workflow was developed by Pierpaoli et al. (2010), Modat et al. (2010), Fang and Boas (2009). The method proposed by Fang and Boas (2009) is shown in Figure 2.19. Each connection in the figure represents an atomic subtask to process and convert the image or mesh into the target state along the work-flow. Three

highlighted paths (red lines and a blue line) represent the high-level processing wrapper subroutines provided by this package, which directly convert volumetric binary/grey-scale images into surface or volumetric meshes.

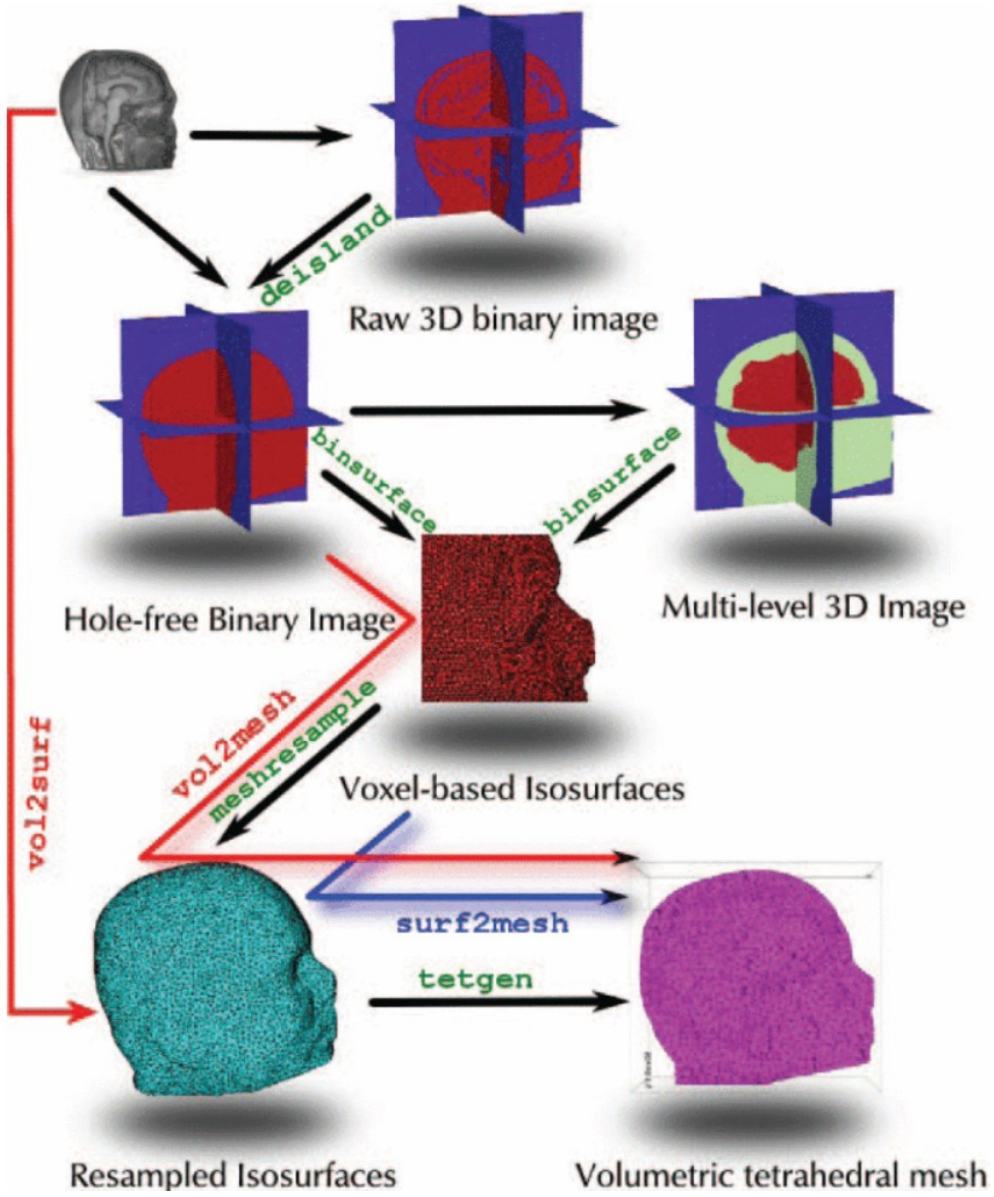


Figure 2.19 Mesh generation work-flow diagram (Fang and Boas, 2009).

The process of mesh generation can be divided into two subsequent steps. In the first step, triangular iso-surfaces with the specified density are extracted from the input 3D

image. Imaging data can be obtained from two-photon microscopy scan, MRI and digital breast tomosynthesis. When there is an iso-surface not closed, Fang and Boas (2009) calculate the surface edges located on the bounding box of the volume and add piecewise linear complex to form a closed surface. Optionally, a mesh repairing process is applied to the resulting surface to remove isolated vertices, duplicated elements and non-manifold vertices. In the second step, tetrahedral elements are filled for the sub-volumes bounded by the previously extracted iso-surfaces. Holes or sub-regional labels can be supplied so that the resulting finite element method mesh may carry hollow structures or sub-domains that correspond to different tissue types. The use of this work-flow has proved popular, for example, to explore the risk factors associated with the early stages of Alzheimer's disease (Guo et al., 2018).

Padmos et al. (2021) simulated a tissue perfusion model by further developing the brain mesh proposed by Garcia-Gonzalez et al. (2017). A one-dimensional intracranial blood flow model and a method to couple this to a brain tissue perfusion model for patient-specific simulations was presented in their study. Image-based patient-specific data on the anatomy of the Circle of Willis were combined with literature data and models for vessel anatomy not visible in the images, to create an extended model for each patient from the larger vessels down to the pial surface, as shown in Figure 2.20. This model, therefore, is able to accurately predict perfusion territories.

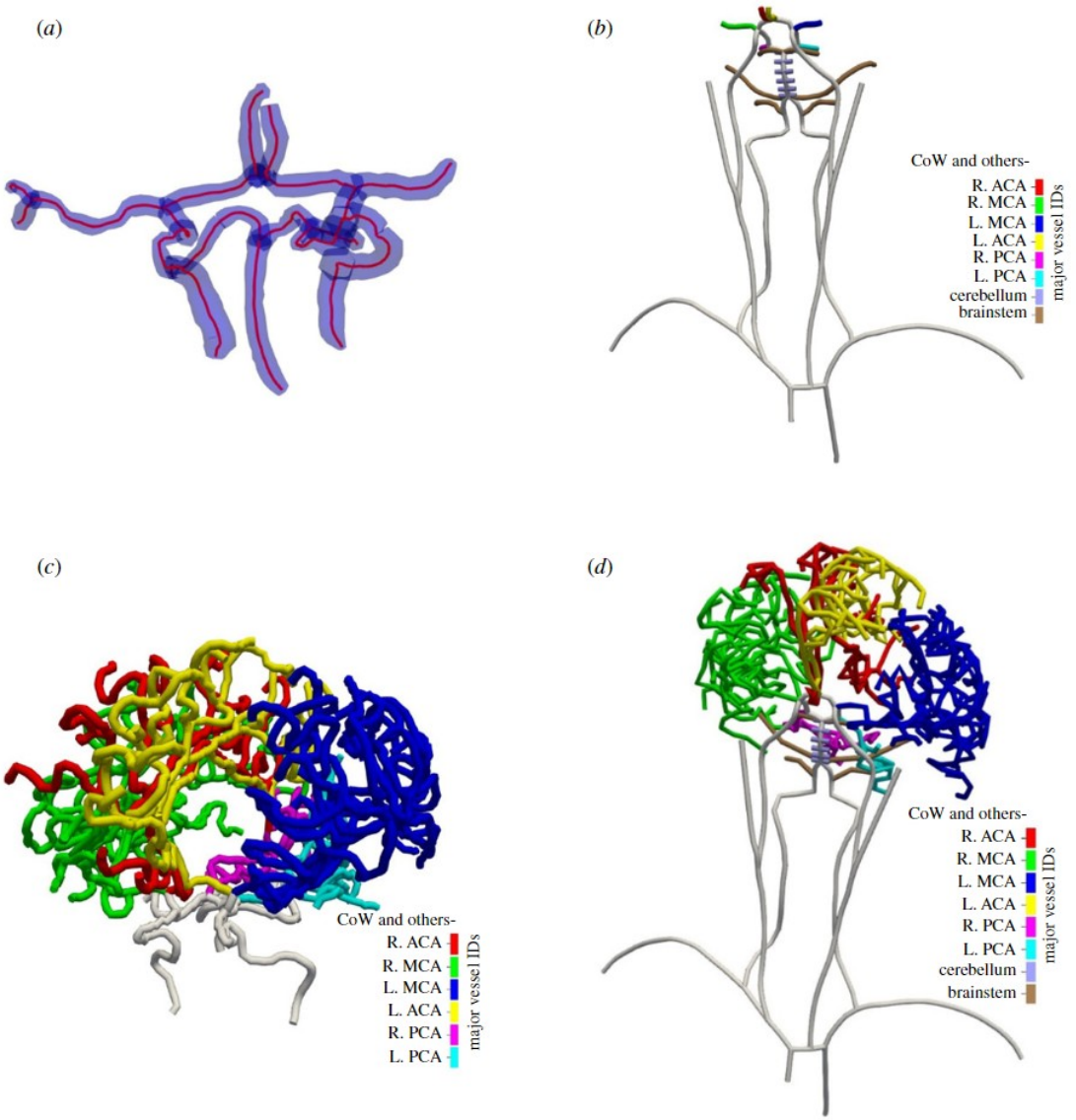


Figure 2.20 (a) Segmentation from a CT angiography from a stroke patient in blue. (b) The large arteries, starting from the heart leading up to and including the patient-specific Circle of Willis. Smaller vessels to the brainstem and cerebellum are also included. (c) One of the centreline segmentations from the BraVa dataset (ID: BG18). (d) The final patient-specific arterial network. This figure was reproduced from Padmos et al. (2021)

2.6 Measurements

2.6.1 Measurements of Blood flow

In this section, the principal methods to quantify cerebral blood flow are described. An increasing number of studies have compared quantitatively non-invasive measurements and minimally invasive measurements for CBF. Transcranial Doppler and several of the main imaging modalities and methods that have been widely used in humans are described in this section. Summary of all measuring methods is presented in Table 2.2.

Flow velocity instruments are applied to determine the flowrate of blood. Transcranial doppler ultrasound probes are most commonly used to measure blood velocity. Initially, two probes were placed in a vessel and the velocity determined by the difference between emitted and reflected frequencies by probes (Haywood et al., 1981, Bishop et al., 1986). Aaslid et al. (1982) were the first to perform this in intracranial vessels non-invasively. Their contribution was to use a lower insonation frequency of 1-2 MHz, compared to earlier usage of 5-10 MHz, and to insonate above the temporal bone, where the skull bone is thinner. These two factors enabled the ultrasound to penetrate within the brain tissue in a way that had not previously been possible.

Several imaging modalities are used to measure cerebral blood flow, four of which are described briefly here: positron emission tomography (PET), single-photon emission computed tomography (SPECT), computed tomography (CT) and magnetic resonance imaging (MRI). It is important to note that all imaging measurement theories are based on the movement of a tracer, which is transported around the brain in the vasculature (Payne, 2017). All tracer kinetic theory is thus fundamentally based on a compartment

theory. The concept of compartment theory can be based on one or more compartments as desired given a certain volume in the brain.

CT works by using a sequence of detectors, which are placed opposite an X-ray tube. The X-ray tube rotates around the head continuously to collect the data. The development of CT allows creating a full 3D image of perfusion and was first used in the 1970s. By obtaining multiple images scanned from different angles, a full 3D image can be reconstructed. A method named Xenon-CT is commonly used to determine the cerebral blood flow and is a non-invasive technique.

Single-photon emission computed tomography (SPECT) uses a gamma-emitting radioisotope, which is injected into patients' bloodstream in very small quantities. Then the gamma-rays can be emitted around the body and detected by gamma cameras that are rotated around the patients(Payne, 2017). SPECT can provide true 3D information which is presented as across-sectional slices.

Position emission tomography (PET) is also based on radioisotope injections, similar to SPECT. The commonly used tracers in PET for CBF measurements are $^{15}O_2$, $C^{15}O_2$ and $H_2{}^{15}O_2$. PET uses two gamma-rays with 551keV energies each, following annihilation with an electron in brain tissue. The drawbacks of PET are the extremely high cost and the high radiation during the test.

Magnetic resonance imaging (MRI) is one of the most popular methods to detect CBF. The advantages for MRI include no ionizing radiation, superior soft tissue contrast and proper spatial resolution down to less than 1 mm. The method of detection by MRI is based on measuring the signals from protons in water. When there is no magnetic field

applied to protons, the orientations of the protons are random. Hence, the sum is equal to zero. However, when there is a static magnetic field, named B_0, each proton rotates around the direction of this magnetic field at a certain frequency, known as the Larmor frequency. This frequency is proportional to the strength of the field.

After this static magnetic is applied, a short radiofrequency created by the other magnetic field (B_1) pulse is applied at 90° to the first field. The pulse is governed by two-time constants: T_1 (spin-lattice relaxation) and T_2 (spin-spin relaxation). In practice, T_2 is sometimes named T_2^* to incorporate the effects due to the non-uniformity of the B_0 field and local variations in magnetic susceptibility.

There are three main types of perfusion MRI: T1-weighted DCE-MRI, T2/T2*-weighted DSC-MRI and ASL. Zhang et al. compared the measurements of CBF recorded simultaneously using ^{15}O-water PET and ASL in a 3 T MR-brain PET scanner in young healthy male volunteers (Zhang et al., 2014). They concluded that the results for CBF were found to exhibit a statistically significant correlation, although the absolute global values have a significant difference (43.6±6.1 ml/100g/min and 51.9±7.1 ml/100g/min for PET and ASL respectively).

Table 2.2. Summary of blood flow measurement.

Principle methods	Species	Description
Transcranial doppler ultrasound probes	Humans	These two factors enabled the ultrasound to penetrate within the brain tissue in a way and obtain the blood flow velocity.
Positron emission tomography (PET)	Humans	PET is based on radioisotope injections. Two gamma-rays with 551keV energies each are used, following annihilation with an electron in brain tissue.
Single-photon emission computed tomography (SPECT)	Humans	By injecting a gamma-emitting radioisotope to patients' blood stream, the gamma-rays can be emitted around the body and detected by gamma cameras.
Computed tomography (CT)	Humans	The X-ray tube rotates around the head continuously to collect the data. The development of CT allows creating a full 3D image of perfusion. Xenon-CT is commonly used to determine the cerebral blood flow.
Magnetic resonance imaging (MRI).	Humans	The method of detection by MRI is based on measuring the signals from protons in water.

2.6.2 Measurements of Blood Volume

The cerebral blood volume (CBV) is one of the most essential factors associated with the cerebrum and a key clinical intraoperative monitor during surgery (Barker, 1998, Haruna et al., 1998). Nowadays, studies show patients with aneurysmal subarachnoid haemorrhage (SAH) are at risk for circulatory volume depletion, which is a risk factor for

delayed cerebral ischaemia (DCI). Correspondingly, Hoff et al. suggested that fluid management guided by daily measurements of blood volume could reduce the risk of severe hypovolemia (Hoff et al., 2008).

Accumulating studies have developed a number of methods to measure blood volume over the last 70 years. At early stages, the blood volume was measured directly by injecting a tracer, blood sampling and tracer concentration analysis. The first two standard indicators were a radioactive iodine and Evans blue dye (Bentivoglio and Goldberg, 1988). However, these two tracers can remain in the blood for days although they have minor side effects. Then in 1956, Fox and Brooker developed a new dye named indocyanine green (ICG), which reacts with plasma proteins and distributes in body blood circulations (Fox, 1956). One of the benefits of ICG is that it can be eliminated exclusively by the liver and does not accumulate in the body over days (Cherrick et al., 1960).

Imaging modalities are also able to measure cerebral blood volume. Positron emission tomography (PET) and DSC-MRI are commonly used today. The advantage of these imaging instruments is having the ability to detect cerebral blood volume and cerebral blood flow simultaneously (Martin et al., 1987). As discussed in section 2.6.1, by applying tracers in the vasculature, both CBV and CBF can be measured. All these methods rely on using a model of CBF and CBV to fit the experimental data.

Iijima et al. (1997) used PET measured the arterial fraction of CBV was 37%. Normal human CBV database was measured by Ito et al. (2004). It is shown that CBV=

$3.8 \pm 0.7\, ml/(100\, ml\, tissue)$. Jain et al. (2013) compared the CT perfusion parameters for a control group and a HT group: the mean reduction rate of CBV is $19 \pm 6.8\,\%$.

Relative cerebral blood volume (rCBV) is also widely measured by PET and MRI. rCBV is calculated clinically from data collected on the ipsilateral side compared with the contralateral (healthy) side. Then the rCBV values are normalized to the rCBV in a reference region such as normal-appearing white matter when a more quantitative assessment of rCBV is required (Bedekar et al., 2010).

Recent studies have suggested a non-invasive method, called pulse oximetry to measure the blood volume by monitoring arterial blood oxygen saturation (Severinghaus and Honda, 1987). Furthermore, another advanced method modified by pulse oximetry, named pulse spectrophotometry or pulse dye densitometry, can allow clinicians to measure the ratio of the arterial haemoglobin concentrations to ICG continuously (Iijima et al., 1997, Hoff et al., 2008). Haruna et al. (1998) reported the clinical accuracy of a new noninvasive bedside blood volume measurement test that used pulse spectrophotometry (the pulse method). They found that in most patients, the pulse method provides bedside measurement of blood volume without blood sampling (except for haemoglobin determination), with an estimated error less than 10%.

Summary of all measuring methods is presented in Table 2.3.

Table 2.3. Summary of blood volume measurement.

Principle methods	Species	Description
Tracer concentration analysis	Humans	Tracers could be radioactive iodine, Evans blue dye and indocyanine green (ICG)
Positron emission tomography (PET) and DSC-MRI	Humans	They two types of common Imaging modalities, which are able to measure the CBV and CBF simultaneously.
Pulse oximetry, Pulse spectrophotometry	Humans	It is used by monitoring arterial blood oxygen saturation

2.6.3 Measurements of Haematoma Volume

Only a few studies have investigated the micro-haematoma caused by a single capillary vessel or within a small vasculature network. van Kranendonk et al. (2020) reported that the haemorrhage sizes for HI1 and HI2 are 0.17ml (0-1.7) and 3.2ml (1.7-6.1) respectively. Most clinical, anatomical, and imaging studies focus only on significant and macroscopic haematomas (size presented of the order of cm^2 or ml). Typical measured macroscopic haematoma volumes are listed in Table 2.4. As shown in Table 2.4, the size of haematoma is commonly found to be in the range from 20ml to 61.3ml. According to Kuramatsu et al. (2011), older people have larger haematomas.

The most common technique to determine the haematoma volume is using a CT scan. However, the regions of haematoma are all manually chosen, which may result in the standard of the circled haematoma range being different due to different imaging

equipment and human factors. Since there is no clinical standard of haematoma boundary, neither based on pressure field nor on blood fraction in tissue, these difficulties are unlikely to be overcome in the near future. In addition, due to the thickness of imaging slices, the estimation of haematoma volume probably leaves out geometry information in the gap between imaging slices.

Table 2.4 Macroscopic haematoma volumes from literature.

Haematoma Volume	Method	Reference
<70 years: 26.2 ml(median); 70-80 years: 37 ml(median); >80 years: 61.3 ml(median)	Formula of ellipsoids (ABC/2 (Kothari et al., 1996)) and head computed tomography (CT scan)	(Kuramatsu et al., 2011)
Median intracerebral haemorrhage (ICH) volume: 27 ml (0.05–88 ml)	Manual segmentation and head computed tomography (CT scan)	(Kleinman et al., 2011)
Median intracerebral haemorrhage (ICH) volume: 20 ml (0.01–77ml)	Formula of ellipsoids (ABC/2 (Kothari et al., 1996)) and head computed tomography (CT scan)	(Kleinman et al., 2011)
Median spontaneous haematoma volume: 27ml	CT planimetry and haematoma was defined as the region of increased density	(Statham and Todd, 1990)
Mean chronic subdural haematoma volume: 119.6 (SD 62.2) ml (range, 19.5–343.8 ml)	Computed tomography (CT scan), PACS imaging display software (Centricity RA1000, GE Healthcare, Taipei, Taiwan) and hand-traced by the radiologist	(Huang et al., 2014)
Hemorrhage volume:	CT scan	(van Kranendonk et al.,

PH1: 6.3ml (4.2-12.9) PH2: 46.8ml (18.7-100.7)		2020)

2.7 Verification, validation& uncertainty quantification

Scientific computing frequently relies on mathematical models that are essentially interconnected systems of nonlinear partial differential equations. These models are utilized to generate results, commonly known as simulations, which are often subject to associated numerical approximation errors. Despite the significant evolution of scientific computing, there's typically a notable gap between these simulations and their practical applications. While simulations are primarily deterministic, biomedical engineering applications are fraught with uncertainty. These uncertainties stem from various factors such as individualized brain geometries, patient-specific haemodynamic variations, and external environmental influences.

There thus has been a recent surge in interest surrounding the verification, validation& uncertainty quantification (VV&UQ)-also known as verification and validation (V&V)-of large-scale simulations, as well as in modelling and quantifying uncertainty. The U.S. Defence Modelling and Simulation Office (http://www.dmso.gov), part of the Department of Defence, has been at the forefront of this movement, developing key concepts and terminology for verification and validation. In 1994, the Defence Modelling and Simulation Office formulated and published definitions of these terms, which have since been widely accepted and utilized by other professional engineering

bodies, including the American Institute of Aeronautics and Astronautics (e.g., see AIAA 1998 Committee (1998)).

The definitions of verification and validation proposed by the Defence Modelling and Simulation Office is very specific:

- Verification ensures that a model's algorithms are correctly implemented and that its numerical solutions converge to the exact ones. It uses simplified systems with "fabricated" solutions as exact ones are often unknown for real systems.
- On the other hand, validation assesses if the model accurately represents the real world by comparing its results with experimental data. Essentially, verification checks if the equations are solved correctly, while validation ensures the right equations are solved.

Uncertainty in scientific computing falls into two categories: (a) aleatory, which is the inherent variability of a quantity expressed through a probability density distribution, and (b) epistemic, stemming from a lack of knowledge by those involved in modelling, analysis, or validation. This lack of knowledge can relate to system modelling, simulation errors, or data scarcity. Uncertainties, whether purely aleatory, purely epistemic, or a mix, can arise from various sources including model inputs, the model's structure, and numerical approximation errors (Roy and Oberkampf, 2011).

Quantifying uncertainties presents a significant challenge (Karniadakis, 2009). In the field of biomedical engineering, one such uncertainty lies in determining the elasticity of vessel walls, a vital factor in accurately depicting the interaction between blood flow and arterial walls. Medical handbooks provide average values for certain essential

properties like the modulus of elasticity and Poisson ratio for main arteries. However, considerable variability exists even among patients of the same gender, age, or background. This variability is exemplified by a study where the Cauchy stress was measured in five patients, anticipated to have a similar response (Maier et al., 2010). The study revealed significant differences in response and elastic properties despite identical test conditions.

Roy and Oberkampf (2011) suggested a framework for verification, validation, and uncertainty quantification (VV&UQ) applied to air flow in a hypersonic wind tunnel. The crucial steps involve:

1. Identifying all uncertainty sources.
2. Characterizing these uncertainties.
3. Estimating the numerical approximation uncertainty.
4. Propagating input uncertainties through the model.
5. Estimating model form uncertainty.
6. Assessing the total uncertainty in system response quantities.

The outcome indicates that to ensure a 95% certainty against condensation in the test section (i.e., Temperature $\geq$ 80 K), the nominal stagnation temperature needs raising, as presently it only offers a 75% assurance.

Pathmanathan and Gray (2014) also employed the principles of VV&UQ in their research to verify computational models used in cardiac electrophysiology. In this study, verification can be divided into two phases: code verification and calculation verification. Code verification involves assembling evidence to support the accuracy of

the software implementation. In the process of calculation verification, the objective is to determine the potential errors in simulations relevant to the field of interest. This takes into consideration the finalized model and numerical parameters, specifically focusing on the chosen mesh resolution.

The underlying principle of VV&UQ is to meticulously distinguish between aleatory and epistemic uncertainties in input values, while precisely addressing numerical solution errors and model form uncertainty with respect to the anticipated system response quantities. This method provides the decision maker with a clear and unmistakable understanding of the uncertainties associated with the predicted outcomes.

For a comprehensive understanding of Verification, Validation, and Uncertainty Quantification (VV&UQ), refer to Oberkampf et al. (2004), Council (2012), Oberkampf and Roy (2010) and the references included therein.

2.8 Summary

In this literature review, the physiological, mathematical and vessel geometrical background information, which is relevant to the simulations presented below, has been introduced and discussed. Background brain physiology including the brain circulation and blood vessel structure has been described in detail. The pathologies of stroke have also been introduced here. This information can help in the development a circulation network model and a leakage model in the haemorrhagic transformation simulations, which will be presented in the next chapter. As the final part of this chapter, a method called Verification, Validation & Uncertainty Quantification (VV&UQ) is introduced. This

1 approach provides researchers with a comprehensive understanding of the
2 uncertainties linked to the anticipated outcomes of their models. Further discussion on
3 Verification, Validation & Uncertainty Quantification is presented in Chapter 6.

Chapter 3: Mathematical modelling of haemorrhagic transformation after ischaemic stroke

The work presented in this chapter is produced from: Jiayu Wang, Stephen J. Payne, Mathematical modelling of haemorrhagic transformation after ischaemic stroke, Journal of Theoretical Biology, Volume 531, 2021, 110920, ISSN 0022-5193, https://doi.org/10.1016/j.jtbi.2021.110920.

Contributor Roles Taxonomy:

Jiayu Wang: Methodology, Software, Validation, Writing - Original Draft, Visualization.

Prof. Stephen J Payne: Supervision, Conceptualization, Writing - Review & Editing.

3.0 Abstract

With an increasingly elderly population globally, the impacts of cerebrovascular diseases, such as stroke and dementia, become increasingly significant. Haemorrhagic transformation (HT) is one of the most common complications of ischaemic stroke that is caused by dysfunction of endothelial cells in the blood-brain barrier (BBB) and that can be exacerbated by thrombolytic therapy. Recent studies also suggest that HT can lead to an increase in intracranial pressure (ICP) and result in capillary compression. The aim of this study is to develop a mathematical model that can be used to simulate the consequence of HT over a range of vasculature length scales. A 2-dimensional vasculature model is used to investigate the severity of HT with different vascular geometry. The resulting model shows that the haematoma radius is approximately constant across different length scales ($100-1000\,\mu m$) and in good agreement with the available experimental data. In addition, this study identified that the effects of capillary compression do appear to have a significant impact on the leakage fraction of blood and hence act to restrain the development of a haematoma.

3.1 Introduction

The brain is a highly dynamic system that needs a continuous and sufficient supply of oxygen, nutrients and other substances to maintain healthy functioning. With an increasingly elderly global population, the importance of cerebrovascular diseases continues to grow, with resulting significant clinical challenges. In particular, stroke is one of the most severe and important causes of damage to brain tissue and is a leading cause of death and disability (Payne, 2017).

Two main types of stroke are classified based on their pathology: ischaemic stroke and haemorrhagic stroke. In the context of ischaemic stroke, it is important to investigate haemorrhagic transformation (HT), since this is a common complication after ischaemic stroke onset (Álvarez-Sabín et al., 2013). HT can be divided into two types, spontaneous HT and secondary HT. Both types of HT are due to the disruption of the blood-brain barrier (BBB) and can cause significant damage to brain tissue. Secondary HT is a side-effect of the use of thrombolytic therapy that uses recombinant tissue-plasminogen activator (rt-PA) to treat ischaemic stroke. This drug can change the BBB permeability sufficiently to cause the leakage of blood into the surrounding brain tissue. Spontaneous HT is rarer than secondary HT, with Tan et al. reporting that the proportion of spontaneous HT is observed in just 50 out of 407 patients (12.3%¿ (Tan et al., 2014).

BBB breakdown is one of the crucial aspects of HT, caused by the loosening of tight junctions (TJs). The functionality of the BBB is mainly provided by endothelial cells that are attached to each other by TJs. The BBB is responsible for regulating essential nutrients, ions, neurotransmitters, macromolecules and neurotoxins (Abbott et al.,

2010). It is formed by three cellular components of the brain microvasculature: endothelial cells, astrocyte end-feet, and pericytes (PCs) (Ballabh et al., 2004). Any disruption of the BBB can result in leakage of blood to brain tissue, leading to damage and hence functional impairment.

A key question to answer is whether HT can be predicted after ischaemic stroke, i.e., can researchers and clinicians identify those patients who are most at risk of HT, based on available imaging data and other clinical parameters. Meanwhile, one current clinical challenge is that clinicians cannot always identify which patients are most at risk from treatment by rt-PA, which may lead to severe HT. Thevathasan et al. (2018) have shown that the cortical involvement rate is 93% for HT patients. Adequate data of the architecture of the microvasculature in the human cortex is now available, and a large number of studies have been carried out to investigate the structure and connectivity of the cerebral microvasculature network, from arterioles and venules on the surface pial vessels, down to capillary network in the grey matter (Cassot et al., 2006, Lauwers et al., 2008, Cassot et al., 2010, Francis et al., 2009, Lorthois et al., 2014). Thus, by creating a cortical scale haemorrhage model, predicting intracerebral haemorrhage could be more accurately.

To the best of the author's knowledge, there are currently no models of HT in the human vascular network. Computational models of BBB permeability have, however, been investigated at the molecular level, cellular level, tissue level and organ level (Shityakov and Förster, 2018). A mathematical model has also been established by Lang et al. (2017) to investigate how an increase in BBB permeability affects vasogenic

oedema. In their model, the sensitivity of capillary hydraulic permeability to the system is emphasised. However, the effects of capillary compression are mentioned but not considered in their model. Pozrikidis and Farrow (2003) simulated blood flow across the BBB in tumours: in their model, a single vessel is considered to display the integrated theoretical model. The exterior interstitial pressure field is calculated by solving Laplace's equation. Chapman et al. (2008) subsequently improved this model by applying it to a 3D network and Pozrikidis (2010) then further developed the single vessel model into a general theoretical framework.

In this study, a model is proposed which is able to simulate the severity of haemorrhage over a range of length scales. The model developed by Pozrikidis and Farrow (2003) was used to simulate fluid flow in tumours as a starting point. This mechanical model is applied on a 2-dimensional bifurcating vasculature model over multiple generations (Payne and Lucas, 2018). Properties such as blood leakage fraction and haematoma volume are calculated to describe the severity of the haemorrhage. Capillary compression is also considered due to an increase in intracranial pressure (ICP) (Bordoni et al., 2020) and a comparison of HT parameters with both constant vessel diameter and variable diameter is discussed. Meanwhile, a new method is developed to calculate vasculature permeability by using the permeability-surface area product, KPS, which can be measured in acute ischaemic stroke in humans using MRI (Merali et al., 2017).

3.2 Materials and Methods

3.2.1 Governing equations

The simplest model for one isolated vessel is considered as a starting point, by using the model proposed by Pozrikidis and Farrow (2003) to simulate fluid transport in tumours.

This permeability simulation is similar to this HT model in that vascular walls are highly permeable in both cases. They used a configuration where the middle fifth of a straight capillary vessel is leaking and other parts of the vessel remain impermeable. In contrast, the whole vessel is assumed to be permeable to simplify the calculations in this study: this assumption is also appropriate here since the aim is primarily to obtain an understanding of how the vascular geometry affects the development of a haematoma, using a simple network model.

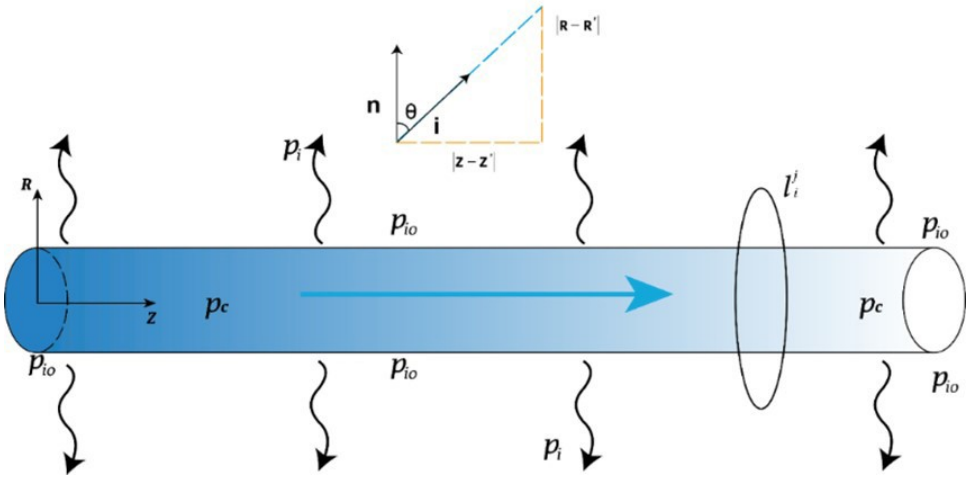


Figure 3.1. Schematic of permeable vasculature model. p_c: capillary pressure; p_{io}: exterior interstitial pressure; p_i: tissue pressure distribution. **Z** axis is the direction along the capillary and **R** axis is the vertical direction. **i** is a unit vector with arbitrary directions and **n** is a normal unit vector. θ is the included angle between i and n. The origin for **i** and **n** vector can be any position in the tissue region and the origin of the **Z** and **R** coordinate system is located at the inlet point of the vessel centreline.

In Figure 3.1, one capillary vessel is divided into Ne_h cylindrical elements, where $j=1,\ldots,Ne_h$. Meanwhile, the surrounding tissue is also divided into Ne_v elements along its vertical axial direction, where$i=1,\ldots,Ne_v$. l is the length measured along the

centreline from an arbitrary origin. Throughout this study, $Ne_h=100$ and $Ne_v=100$ are set to give a good balance between model accuracy and computational expense.

3.2.1.1 Leakage Fraction γ

Vascular blood flow Q_c can be calculated using Poiseuille's law if the blood flow is assumed to be laminar and steady and that blood is incompressible (Sevick and Jain, 1989):

$$Q_c=\frac{-\pi r^4(l^j)}{8\mu}\frac{d\,p_c(l^j)}{dl} \tag{3.1}$$

where r denotes the (variable) vessel radius, μ is the fluid viscosity, and $p_c(l^j)$ is the position-dependent capillary pressure along the vessel as a function of l^j, as defined above.

The extravasation flux through the vessels wall can then be described by Starling's law:

$$q_e(l^j)=L_p(l^j)[p_c(l^j)-p_{io}(l^j)]n \tag{3.2}$$

where $q_e(l^j)$ is the leakage flux vector that is normal to the capillary, $L_p(l^j)$ is the position-dependent vascular permeability, which can vary with axial position, and n is the unit vector radially outward normal to the vessel wall.

Then mass conservation of fluid in the leaking vessel can be applied:

$$\frac{dQ_c}{dl^j}+2\pi r(l^j)q_e(l^j)n=0 \tag{3.3}$$

Then Eq. (3.1) and Eq. (3.2) can be substituted into Eq. (3.3):

$$\frac{d^2p_c(l^j)}{dl^{j2}}+\frac{4}{r(l^j)}\frac{dr(l^j)}{dl^j}\frac{d\,p_c(l^j)}{dl^j}=\frac{16\,\mu L_p(l^j)}{r^3(l^j)}\left[p_c(l^j)-p_{io}(l^j)\right] \tag{3.4}$$

Meanwhile, mass conservation can also be described by:

$$-k\frac{d\,p_{io}(l^j)}{d\,l^j}=-n\nabla p_{io}(l^j)\approx q_e(l^j)=L_p(l^j)[p_c(l^j)-p_{io}(l^j)] \tag{3.5}$$

where k denotes hydraulic conductivity, as derived by Pozrikidis and Farrow (2003), and q_e is the leakage flux.

Pozrikidis and Farrow (2003) calculated the leakage rate by obtaining the inlet and outlet flows instead of applying Eq. (3.2):

$$Q_a=\frac{\pi r^4}{8\,\mu L}[\alpha_a(L_p,k)\Delta P_{av}+\beta_a(L_p,k)\Delta P_{at}] \tag{3.6}$$

$$Q_v=\frac{\pi r^4}{8\,\mu L}[\alpha_v(L_p,k)\Delta P_{av}-\beta_v(L_p,k)\Delta P_{at}] \tag{3.7}$$

where $\Delta P_{at}=P_a-P_o$ denotes the pressure difference between inlet arterial pressure P_a with brain tissue ambient pressure P_o and $\Delta P_{av}=P_a-P_v$ denotes the pressure drop along the vessel, L denotes the capillary length. The hydraulic conductivity parameters, α_a,α_v,β_a and β_v (defined below) are dependent on hydraulic conductivity k and vascular permeability L_p (Chapman et al., 2008).

Thus, leakage fraction $\gamma$and leakage flow rate Q_{flux} can be determined from the inlet and outlet flow rates:

$$Q_{flux}=Q_a-Q_v=\frac{\pi r^4}{8\,\mu L}¿ \tag{3.8}$$

$$\gamma=\frac{Q_a-Q_v}{Q_a}=(\alpha_a-\alpha_v)\Delta P_{av}+\frac{(\beta¿¿a+\beta_v)\Delta P_{at}}{\alpha_a\Delta P_{av}+\beta_a\Delta P_{at}}¿ \tag{3.9}$$

Note that the leakage fraction γ denotes the ratio of the leakage rate from one vessel relative to the inlet flow rate of blood in this vessel.

Chapman et al. (2008) defined dimensionless hydraulic conductivities $\alpha_a, \alpha_v, \beta_a$ and β_v in terms of R_{es}, q' and ϵ':

$$\alpha_a = \frac{\omega}{\sinh \omega}, \qquad \alpha_v = \omega \coth \omega \tag{3.10}$$

$$\beta_a = \frac{\omega}{\sinh \omega}(\cosh \omega - 1), \qquad \beta_v = \frac{\omega}{\sinh \omega}(\cosh \omega - 1) \tag{3.11}$$

where $\omega^2 = R_{es}/(1 - \tau\epsilon \log(\epsilon'))$ and $\epsilon' = r/L$.

Meanwhile, Chapman et al. (2008) listed other two dimensionless parameters to denote a measurement of flow resistance inside the capillary, R_{es}, and the length scale times the length of each capillary length, τ:

$$R_{es} = \frac{16 \mu L_p L^2}{r^3}, \qquad \tau = \frac{L_p L}{k}, \tag{3.12}$$

Hence, the leakage fraction γ and leakage flow rate Q_{flux} can be obtained by calculating dimensionless hydraulic conductivities $\alpha_a, \alpha_v, \beta_a$ and β_v.

3.2.1.2 Blood Pressure in Vessels, p_c

The next parameter to be calculated is the capillary pressure, p_c, which is calculated based on Eq. (3.4).

In this simulation, vessel diameter varies with axial length. The second term in Eq. (3.4) can be neglected since it is of order 0.1 as determined numerically. Thus, Eq. (3.4) reduces to a linear second-order equation:

$$\frac{d^2 p_c(l^j)}{dl^{j2}} = \frac{16 \mu L_p(l^j)}{r^3(l^j)} \left[p_c(l^j) - P_o \right] \tag{3.13}$$

where $j = 0$ denotes the capillary entrance point and $j = Ne$ corresponds to the capillary end point. Then Eq. (3.13) can be solved to give (Pozrikidis and Farrow, 2003):

$$p_c(Z)=P_o+\left(\frac{1}{e^{\lambda}-e^{-\lambda}}\Delta P_{av}+\frac{e^{\lambda}-1}{e^{\lambda}-e^{-\lambda}}\Delta P_{at}\right)e^{\frac{-Z}{\delta}}-\left(\frac{1}{e^{\lambda}-e^{-\lambda}}\Delta P_{av}+\frac{e^{-\lambda}-1}{e^{\lambda}-e^{-\lambda}}\Delta P_{at}\right)e^{\frac{Z}{\delta}} \quad (3.14)$$

where $\delta=L/\left(4\sqrt{\frac{\mu L^2 L_p}{r^3}}\right)$, $\lambda=4\sqrt{\frac{\mu L^2 L_p}{r^3}}$ and Z denotes the horizontal distance of x (field point) from the vessel entrance point (shown in Figure 3.1).

3.2.1.3 Tissue Pressure Distribution, p_i

To obtain the tissue pressure distribution, the exterior interstitial pressure p_{io} is needed to be determined. Brain tissue is assumed to be an isotropic porous medium such that Darcy's law can be applied:

$$u=-k\nabla p_{io} \quad (3.15)$$

where u is the fluid velocity along the capillary and k is the interstitial hydraulic conductivity. Here, the hydraulic conductivity in tissue is assumed to be constant and, since blood flow is incompressible, this yields:

$$\nabla\cdot u=-k\nabla^2 p_{io}=0 \quad (3.16)$$

Pozrikidis and Farrow (2003) used a Green's function approach for the Laplace equation to solve Eq. (3.16):

$$p_{io}(x)=P_0-\iint_S G(x',x)n\times\nabla p_{io}\,dS'+\iint_S (p_{io}-P_0)n\nabla G(x',x)\,dS' \quad (3.17)$$

where $G(x',x)=\frac{1}{4\pi}\frac{1}{|x'-x|}$ and S' is the surface area of the vessel.

In this particular scenario, Eq. (3.17) can be rewritten as:

$$\sum_{j=1}^{Ne}[¿\delta_{nj}-2B_j(l_i)+\frac{2}{k}L_p{}^j A_j(l_i)]\,p_{io}{}^j=\frac{2}{k}\sum_{j=1}^{Ne}L_p{}^j p_c{}^j A_j(l_i)+P_o[1-2\sum_{j=1}^{Ne}B_j(l_i)]¿ \quad (3.18)$$

where $A_j(l_n)=\int_{E_j} G(x',x)dS$, $B_j(l_n)=\overset{PV}{\int_{E_j}} n\nabla G(x',x)dS$ and δ_{nj} is Kronecker's delta function. This can be solved numerically to calculate the exterior interstitial pressure. PV denotes the principal value of the double-layer potential and E_j denotes the cylindrical surface of the jth element.

The next step is to calculate the tissue pressure distribution by applying Green's function. Eq. (A.3.8) can be used to give:

$$p_i(x')=\int_S [\,p_i(x')\nabla' G(x,x')]dS' \tag{3.19}$$

Note that here the equations presented here are not obtained from the tumour model proposed by Pozrikidis and Farrow (2003).

Finally, the boundary conditions are applied, which are $p_i(x')=P_o$ when $|x|\to\infty$ and $p_i(x')=p_{io}$ when $|x|=r(l_o)$, to give:

$$p_i(x)=P_o+\int_S [\,p_{io}(x')\nabla' G(x,x')]dS' \tag{3.20}$$

According to Pozrikidis (2011):

$$\nabla' G(x,x')=\frac{1}{4\pi}\frac{(x-x')}{|x-x'|^3}=\frac{1}{4\pi}\frac{1}{|x-x'|^2}i=\frac{1}{4\pi}\frac{1}{(Z-Z')^2+(R-R')^2}i \tag{3.21}$$

where i is a unit vector towards any direction, $(Z-Z')$ denotes the distance along the vessel and $(R-R')$ denotes the vertical distance of the field points. Hence:

$$p_i(x)=P_o+\int_s p_{io}(x')\frac{1}{4\pi}\frac{1}{|x-x'|^2}i\,dS' \tag{3.22}$$

where S' is the surface area of capillary and with normal direction, $dS'=d\pi DZ'n$

$$p_i(x) = P_o + \int_s p_{io}(x')\, i\, \frac{1}{4\pi} \frac{1}{(Z-Z')^2+(R-R')^2}\, d\pi DZ'\, n \tag{3.23}$$

$$p_i(x) = P_o + \frac{D}{4}\int_s p_{io}(x')\, i\cdot n \frac{1}{(Z-Z')^2+(R-R')^2}\, dZ'\,' \tag{3.24}$$

$$p_i(x) = P_o + \frac{D}{4}\int_s p_{io}(x')\, |i\cdot n| \cos(\theta) \frac{1}{(Z-Z')^2+(R-R')^2}\, dZ' \tag{3.25}$$

where θ is the included angle between i and n.

Then Eq. (3.25) is substituted to give:

$$p_i(x) = P_o + \frac{D}{4}\int_s p_{io}(x') \frac{|R-R'|}{\left(|Z-Z'|^2+|R-R'|^2\right)^{\frac{3}{2}}}\, dZ' \tag{3.26}$$

Eq. (3.26) then can be integrated numerically to solve for interstitial pressure within the tissue region.

3.2.1.4 Haematoma Volume V

To determine the volume of the haematoma, the haematoma surface boundary needs to be defined. However, there is as yet no clear definition of the haematoma boundary. In previous studies, researchers have defined regions of the haematoma manually to compute haematoma volume (Rodriguez-Luna et al., 2016, Wang et al., 2013). In particular, Schrag et al. (2010) combined both anatomical and imaging analysis to investigate the haematoma caused by individual vessel.

Leaking blood is transported in tissue by convective and diffusive extravasation due to the pressure difference between the exterior capillary surface and the surrounding tissue (Pozrikidis and Farrow, 2003). In this study, the tissue pressure distribution is used

to define the haematoma surface boundary. Once the haematoma boundary pressure is defined, the haematoma radius can be calculated using Eq. (3.26).

To define the surface boundary of the haematoma, two methods are used. The first definition is the point at which tissue pressure has dropped by $99\,\%$ from p_{io} to P_o,

$$P_{99} = p_{io} - 99\,\%\left(p_{io} - P_o\right) \tag{3.27}$$

The other definition is the point at which tissue pressure has dropped to a fixed value: here the values $15.1\,mmHg$ and $15.5\,mmHg$ were used, being $0.1\,mmHg$ and $0.5\,mmHg$ above the far-field interstitial pressure respectively. These two values are arbitrary but used here as a first metric in the absence of any 'gold standard'. Finally, after the radius of the haematoma in jth element, R_j, are obtained, the volume of haematoma can then be determined by summation:

$$V = \sum_{j=1}^{Ne_h} \frac{L}{Ne}\left(R_j^{\,2} - r_j^{\,2}\right)\pi \tag{3.28}$$

where R_j denotes position-dependent haematoma radius.

3.2.2 Physiological parameter

In this model, two key parameters, vascular permeability L_p and hydraulic conductivity k are required. The hydraulic conductivity in particular is difficult to measure in vivo (Chapman et al., 2008). Some experiments that have listed the values of hydraulic conductivity in various tissues are given in Table 1. Hydraulic conductivity k thus appears to lie in the range 1×10^{3} to $1\times10^{6}\,\mu m^{3}\,s\,kg^{-1}$. All values of k in this range were tested and the sensitivity of leakage fraction to k is found to be not significant, compared with

Lp. Thus, in this study, a baseline value has been selected as k of $5 \times 10^5 \, \mu m^3 \, s \, kg^{-1}$ (approximately the median value in the range above).

Table 3.2 Values of hydraulic conductivity k in different tissues, as quoted by other authors.

Tissue	Hydraulic Conductivity k $\mu m^3 \, s \, kg^{-1}$
Dog squamous cell tissue (Guyton et al., 1971)	1.8×10^6
Hepatoma 5123 in vivo (Swabb et al., 1974, Guyton et al., 1971)	$2.9 \times 10^3 - 8.4 \times 10^3$
Rat squamous cell tissue (Swabb et al., 1974)	6.4×10^3
Hepatoma 5123 in vitro (Swabb et al., 1974)	3.1×10^4
Rat hepatic carcinoma tissue in vitro and in vivo (Baish et al., 1997)	$0.3 \times 10^5 - 1.5 \times 10^5$
Mouse mammary carcinoma MCa-IV (Jain et al., 2007)	1.8×10^5

Based on Sevick and Jain (1991), vascular permeability is calculated by measuring the capillary filtration coefficient, CFC:

$$L_p = \frac{CFC}{A'} = \frac{J_f / \left(p_c(l^j) - p_{io}(l^j) \right)}{A'} \tag{3.29}$$

where A' denotes vascular surface area of exchange vessels per 100g of tissue and J_f denotes transcapillary filtration rate. In this model, J_f is assumed to equal the value of permeability-surface area product, KPS that lies in the range

$1.2-1.8\,mL/(100\,g\,tissue)/min$ (Merali et al., 2017), where $A^{'}=5000\,cm^2/(100\,g\,tissue)$ for vascular surface area (Cassot et al., 2006).

Blood viscosity in this model varies with the vessel radius and the haematocrit due to the Fåhræus-Lindqvist effect (Fahraeus and Lindqvist, 1931). The viscosity in the network is in the range of $1.2-1.7\,mPa\cdot s$. The empirical solutions that are used to determine the viscosity can be found in Appendix 3.B.

3.2.3 Network models

The vasculature model used in this simulation is taken directly from Payne and Lucas (2018). In this network, they calculated the generation geometry in 13 generations of blood vessels including 6 arteriolar vessel generations, 1 capillary vessel generation and 6 venule generations. The one change to this model is that the vessel diameter can vary along the blood vessel, due to changes in tissue pressure (to simulate the effects of capillary compression). Bordoni et al. (2020) describe the correlation between changes of fractional perfused volume (FPV) and ICP in mice:

$$\frac{d(FPV)}{d(ICP)}=-2.16\,\%/mmHg \tag{3.30}$$

Thus, relative changes of vessel diameter and tissue pressure can be quantified:

$$\frac{d(D)}{d(p_{io})}=-\sqrt{\left|\frac{d(FPV)}{d(ICP)}\right|}=-1.47\,\%/mmHg \tag{3.31}$$

where it is assumed that $p_{io}=ICP$.

A schematic of the method of calculation of the vasculature and haemodynamics parameters is shown in Figure 3.2, showing that the basic vascular parameters (length, the baseline of diameter and etc.) are produced by Payne and Lucas (2018), the

haematoma volume can be found by tissue pressure distribution, the leakage fraction can be determined by the corrected diameter and the vascular permeability, and the remaining parameters can be calculated iteratively using experimental data and Eq. (3.9), Eq. (3.14), Eq. (3.26), Eq. (3.28) and Eq. (3.31). A pseudo-algorithm is presented in Appendix 3.D.

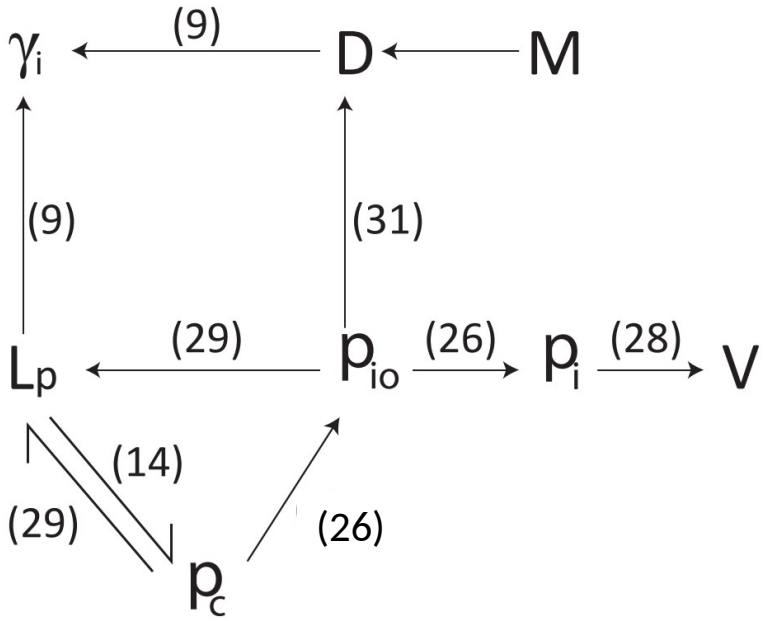


Figure 3.2 Schematic of method of calculation of pressure and vascular parameters: (9)= Eq. (3.9); (14)= Eq. (3.14); (26)= Eq. (3.26); (28)= Eq. (3.28); (31)= Eq. (3.31); M= Model reproduced by Payne and Lucas (2018). Further explanations are presented in Appendix 3.D.

3.3 Results

3.3.1 Leakage fraction

According to Eq. (3.18), the exterior intersititial pressure increases rapidly when HT occurs at these generations. Blood vessels are compressed by increased exterior pressure; in this way, an arteriolar vessel can be reduced to zero area due to high exterior interstitial pressure (as shown for the A1 generation in Figure 3.3). Note that in

this simulation, the potential for vascular collapse based on elevated pressure is not considered separately from other generations.

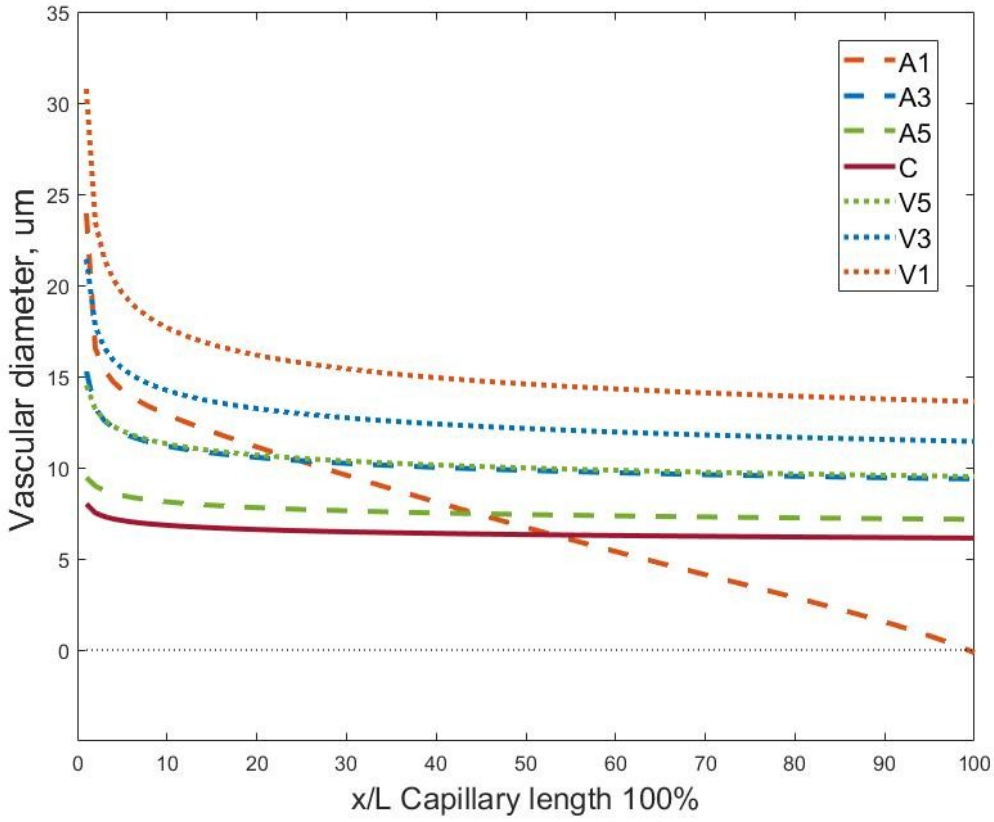


Figure 3.3. Vascular diameter variation with axial length. Only a few generations are shown in this figure for reasons of clarity.

Figure 3.4 shows a comparison of vascular permeability with both constant vessel diameter (dashed lines) and variable diameter (solid lines). Vascular permeability with constant diameter is calculated by assuming that there is no relationship between ICP and vessel diameter. It can be seen that vascular permeability reduces when the vessels are compressed by an increase of exterior interstitial pressure (as shown by comparison between Figure 3.4 and Figure 3.5), as expected. The venule generations are affected by increased exterior interstitial pressure more significantly due to their greater

compliance. Figure 3.5 shows that the variation in p_{io} for the A1 generation rises to a peak substantially and dwindles to approximately zero due to collapse.

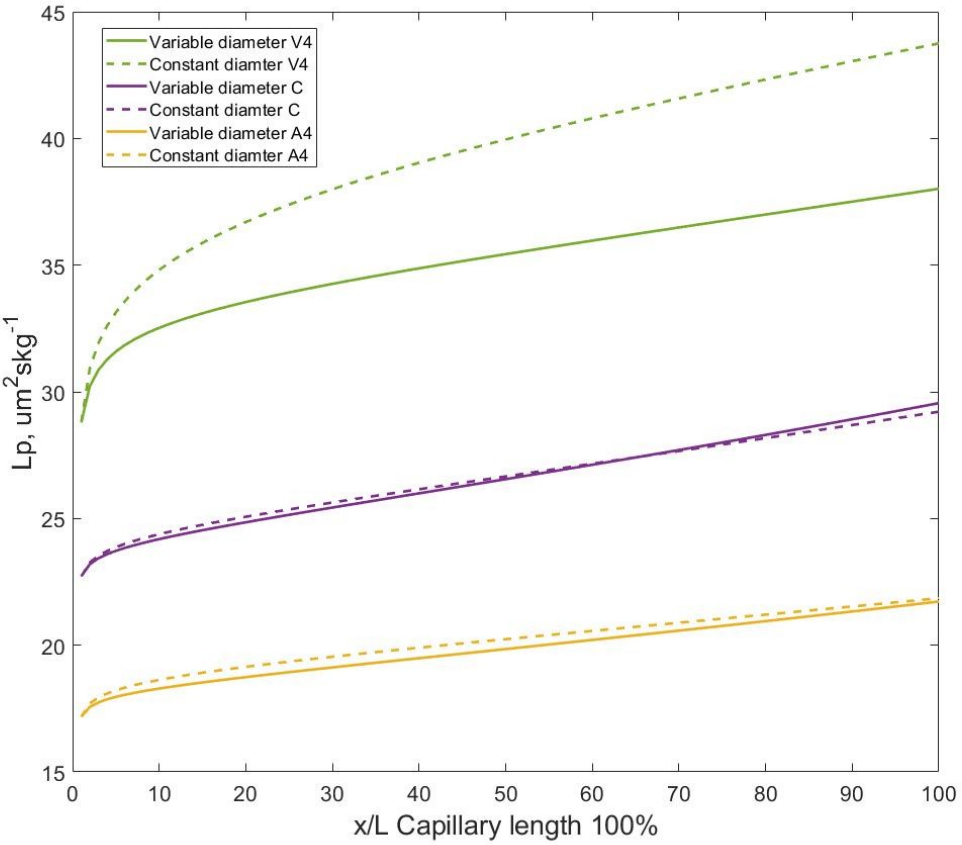


Figure 3.4. Comparison of vascular permeability with constant vessel diameter (dashed lines) and variable diameter (solid lines). Only a few of generations are plotted in this figure for reasons of clarity.

To the best of the author's knowledge, there are currently no experimental data available for HT vascular permeability in brain tissue. Based on calculations, the order of magnitude of L_p is in the range of $10-350\,\mu m^2 s\,kg^{-1}$ for HT. Rippe et al. (1978) investigated Lp in healthy rat hindquarter tissue and measured a value of $2.3\pm0.65\,\mu m^2 s\,kg^{-1}$, Jain et al. (2007) reported a value of L_p in mouse mammary carcinoma MCa-IV of $186\,\mu m^2 s\,kg^{-1}$ and Sevick and Jain (1991) obtained a value of $L_p$in

R3230AC mammary adenocarcinoma in the range of $45-170\,\mu m^2\,s\,kg^{-1}$. This indicates that HT vascular permeability is approximately 10-100 times higher in HT tissue than healthy tissue and about the same as the value of L_p in tumour tissue.

Finally, the leakage fraction can be obtained in each generation as shown in Figure 3.6. In this simulation, the order of magnitude of the leakage fraction is found about $0.1-1\%$.The increased exterior interstitial pressure leads to lower leakage fraction due to lower vascular permeability than of the constant diameter scenario without correlation. In addition, the leakage fraction in the A1 generation with variable diameter is significantly higher than surrounding generations due to its collapse. Note the peak for generation V6 is due to the longer length of this vascular generation than neighbour generations.

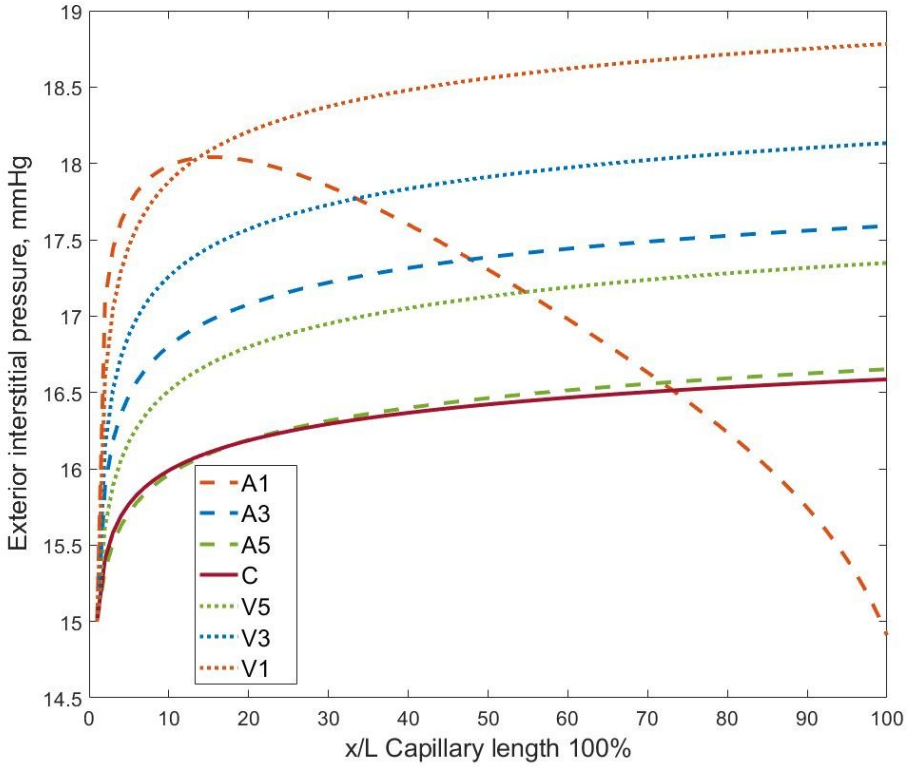


Figure 3.5. Exterior interstitial pressure distribution for every generation. Only a few of generations are displayed in this figure for reasons of clarity.

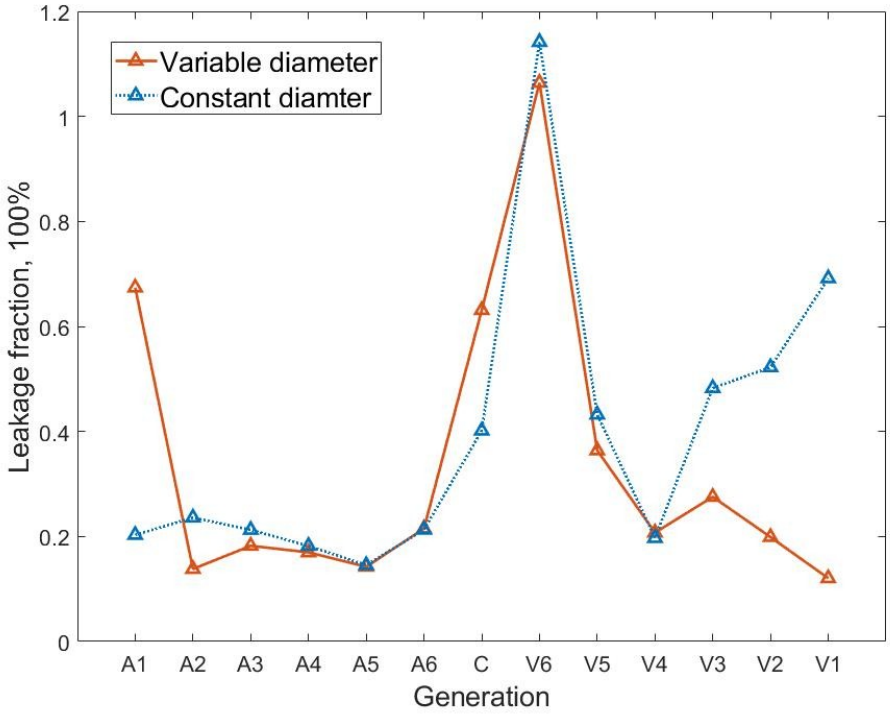


Figure 3.6. Leakage fraction for every generation.

3.3.2 Haematoma volume

Simulations are next performed to model a haematoma after HT. In order to calculate the haematoma volume, the full tissue pressure distribution is required. Based on Eq. (3.18) and Eq. (3.26), a tissue pressure distribution is developed for each generation, as shown in Figure 3.7 for one typical simulation. Ambient tissue pressure in this simulation is set as $15\,mmHg$ and it is assumed that one of the boundary conditions is that tissue pressure drops to this ambient pressure in the far field from the leaky vessels. The other boundary condition is that the tissue pressure surrounding the vessel is equal to the exterior interstitial pressure p_{io}.

In the p_{io} simulation, the results in Figure 3.5 show that p_{io} for every generation except the A1 generation rises rapidly before reaching a near-constant value along the axial

length. Arterioles give rise to higher values of p_{io} due to higher capillary pressure. The A1 generation has the highest exterior interstitial pressure at the beginning but then decreases towards ambient pressure due to the collapse of this generation.

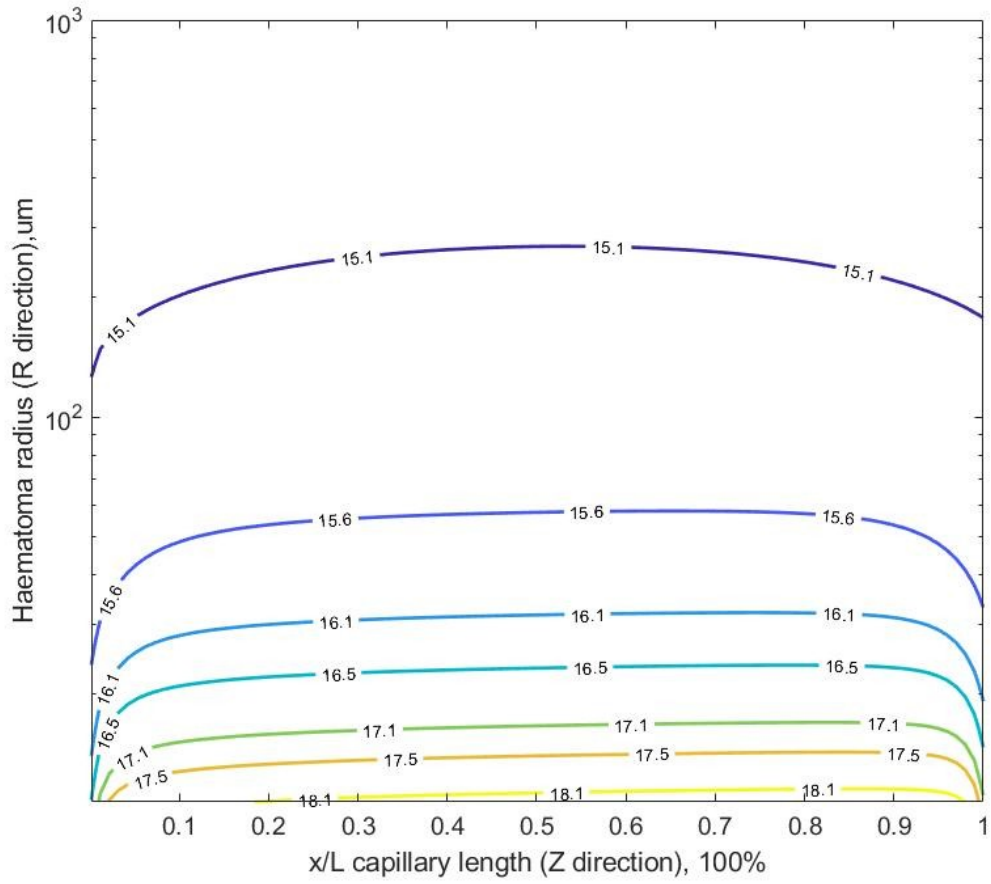


Figure 3.7. Tissue pressure distribution in V3 generation. The units are mmHg.

It is the time to define the surface of the haematoma now. In order to compare the haematoma radius difference between constant diameter vessels and variable diameter vessels, the results from both simulations are shown in Figure 3.8. Earlier, three approaches were proposed to assume the surface pressure. When the surface area is set at $P_{15.1}$ or $P_{15.5}$, the radius of hematoma in the arterioles is found that it does not

increase due to the faster flow rate and the increase of capillary pressure. The haematoma radius reduces along the generations from the A4 generation to the C generation and then keeps a nearly constant value for the middle three generations. The radius then increases slightly. Variable diameter vessels always cause a lower haematoma radius compared to constant diameter vessels.

When the surface pressure is set to P_{99}, since the P_{99} values for the arterioles are higher than those for the middle generations, the tissue pressure drops more rapidly to the surface pressure. Thus, the radius of the haematoma for arteriolar vessels is lower than the haematoma radius of the following generations (A5, A6). Generations C and V6 with smaller vessel diameters exhibit a lower haematoma radius.

Another surprising phenomenon when the haematoma surface pressure is set based on P_{99} is that the haematoma radius for variable diameter vessels is higher than those for constant diameter vessels, which is contrary to what can be found when the surface area is set to $P_{15.1}$ and $P_{15.5}$ in Figure 3.8. When the surface pressure is set to be P_{99}, two boundary conditions are different (exterior interstitial pressure and haematoma surface pressure) for the constant and variable diameter scenarios, making it hard to compare the pressure drop trends for two scenarios without at least one boundary condition being the same.

In these simulations, the radius of the microscopic haematoma is consistently of the order of $10^2 \mu m$. Jenkins et al. (1989) measured the distance between the edge of haematoma and related, damaged vessels to be $700\ \mu m$. In a macroscopic haemorrhagic region, however, it should be noted that there are a large number of damaged vessels

leaking, where permeability is changed by medical treatments or spontaneous lesion transformation. It is important to note that only a single vessel generation leaking is considered in this preliminary study, whereas clinical studies are very likely to have multiple leaky vessels.

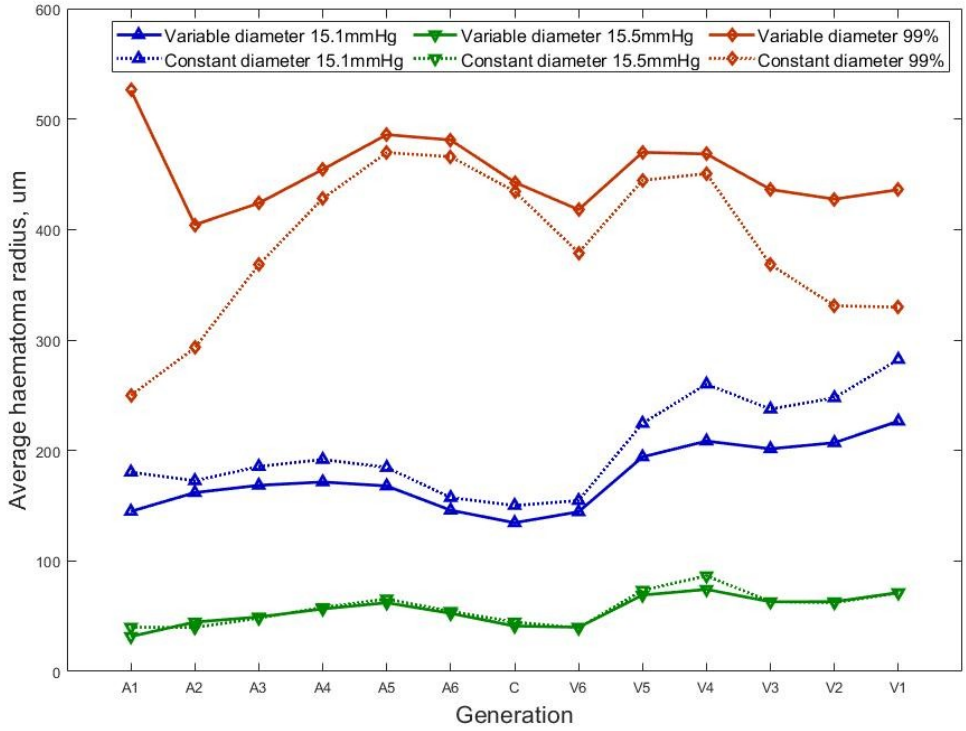


Figure 3.8. Comparison of average haematoma radius for each generation with constant vessel diameter (dashed lines) and variable vessel diameter (solid lines).

Finally, Eq. (3.28) is applied to calculate the haematoma volume. Figure 3.9 shows that the arterioles lead to larger haematoma volume and then the haematoma volume declines along the generations from A1 to the smaller blood vessels before increasing sharply from capillary to venules. However, since that the haematoma radius for every generation in the network is approximately constant, the haematoma volume in Figure 3.9 varies predominantly as a function of the vessel length. Thus, generation length

appears to be the most significant parameter that affects the volume of a haematoma, with the radius being more invariant with geometry.

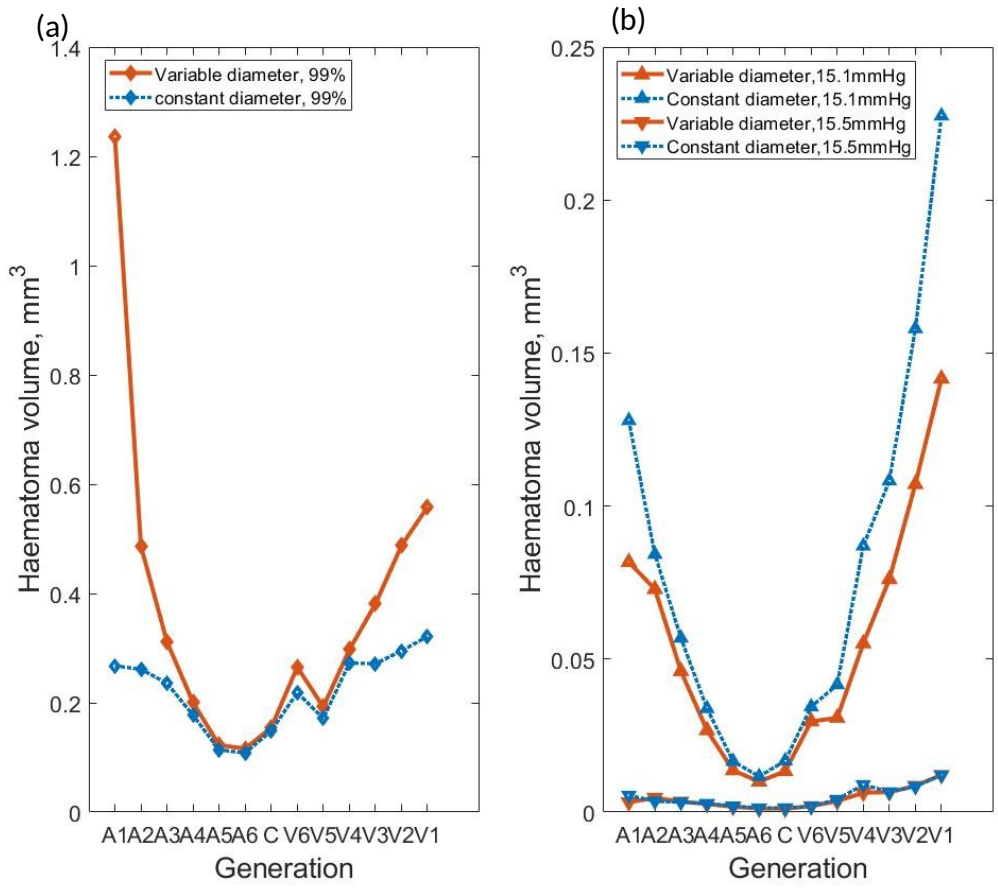


Figure 3.9. Comparison of haematoma volume with constant vessel diameter (blue dashed lines) and variable vessel diameter (orange solid lines). (a): when the haematoma pressure boundary is set as P_{99} ; (b): when the haematoma pressure boundary is set as $P_{15.5}$ and $P_{15.1}$.

3.4 Discussion

A mathematical method is developed here to investigate how changes in vascular geometry can affect the severity of haemorrhagic transformation. This model at this stage is a simple simulation which is applied to a 1D vasculature model with 13 generations. The schematic of calculation steps of key parameters is shown in Figure

3.2. Due to some parameters affecting each other, such as vessel diameter with vascular permeability, an iterative approach was used to determine them.

A mathematical method has been proposed in this study to determine the HT vascular permeability L_p, whereby values ofL_p can be calculated along the vasculature based on specific experimental data of ischaemic stroke in brain. How changes in driving pressure ($p_c - p_{io}$¿can lead to variations of L_p along the vasculature without the effect of increased ICP has been shown in Figure 3.4. Although the BBB permeability can be measured by using dynamic contrast-enhanced T1-weighted MRI (Cramer and Larsson, 2014), the values of KPS obtained from Merali et al. (2017) are taken from macroscopic tissue samples instead of focusing on an individual vessel. There remain technical limitations to imaging the behaviour of individual vessels at this length scale, which makes the use of a mathematical model critical in understanding this type of behaviour.

Comparing the values of L_p used by Chapman et al. (2008), which are in the range 4.5×10^{1}¿$1.7 \times 10^{2}\,\mu m^2\,s\,kg^{-1}$ in tumour tissue, and the values of L_p in this simulation, it can be seen that the BBB permeabilities in a damaged vessel after HT onset are close to the lower limit of L_p found in tumour tissues. Thus the values of blood leakage fraction from this simulation are able to be compared with the values from tumour modelling. Pozrikidis and Farrow (2003) suggested that the values of leakage fraction γ are of the order 10^{-1}. Jain (1987) and Chapman et al. (2008) demonstrated that the values of leakage fraction γ were in the range 6% to 14%. These combined results suggest that the blood leakage fraction in BBB breakdown vessels after HT onset is an order of magnitude lower than is found in tumour tissue.

Eq. (3.30) and Eq. (3.31) were used to describe the capillary compression due to an increase of ICP in HT. How reductions in the vascular diameter can lead to a decrease in L_p, leakage fraction and haematoma volume has been shown in this study. The effect of capillary compression in venules is more significant than arterioles and capillary vessels, as shown in Figure 3.4, 3.6 and 3.8. Note that venules have greater compliance, as shown in Figure 3.4. However, there are some limitations to this method. It is worth noting that an increase of ICP could lead some arterioles to collapse, as shown in A1 generation in Figure 3.3. A higher blood flow rate and higher internal pressure in A1 generation lead to a higher leakage rate of blood and higher exterior interstitial pressure than the following generations. The A1 generation could thus become fully constricted under this condition. This possibility still requires further validation but provides a good justification for considering only the vessels in this simulation.

It is worth noting that Eq. (3.30) is derived based on mice experiments by Bordoni et al. (2020). In their method, they set cerebral perfusion pressure (capillary pressure in this HT case) to be $38.4\,mmHg$. However, in this simulation, the capillary pressure changes along with the vessel generations. The validity of Eq. (3.30) thus needs further investigation. However, to the best the author's knowledge, there is as yet no other current experimental data that describe the correlation of ICP with blood flow volume. Meanwhile, the human brain has an autoregulation mechanism for changes in blood flow and interstitial pressure. There is still some uncertainty in the literature as the mechanism of autoregulation in HT (Strandgaard et al., 1973). Further experiments should be carried out to determine the effects of autoregulation in HT. In this

simulation, one of the assumptions is that the formation of haematoma is fast enough that haemostasis does not occur. The solutions to quantitatively compare time scales of the formation of haematoma and haemostasis are shown in Appendix 3.C. However, the process of haemostasis still should be considered in the following stages since localized vasoconstriction occurs before primary haemostasis (Armstrong and Golan, 2011). In this simulation, the geometry of blood vessels is one of the critical aspects.

In this model, the tissue pressure field has been solved, which can be used to investigate the haematoma radius. However, there is no clear definition of the haematoma boundary, and clinical image researchers have added or removed regions of the haematoma manually in previous studies (Rodriguez-Luna et al., 2016, Wang et al., 2013). To quantify the haematoma surface boundary, two definitions of surface pressure were set (tissue pressure drop to a certain value and drop by a certain proportion). This study has shown that haematoma radius reduces due to the effects of capillary compression when the surface pressure is set to $P_{15.1}$ and $P_{15.5}$. However, this effect reverses when the surface pressure is set to P_{99}. There thus remains some uncertainty how best to quantify the haematoma radius by setting P_{99}.

To the best of the author's knowledge, there is limited current experimental data that describes the development of a haematoma for an individual capillary after HT onset. Jenkins et al. measured the distance in mice between the edge of haematoma and related, damaged vessels to be $700\,\mu m$ (Jenkins et al., 1989), which is in very good agreement with the values obtained here. In a macroscopic haemorrhagic region, there

are a large number of damaged vessels leaking, where permeability is changed by medical treatments or spontaneous lesion transformation.

It is necessary to discuss the differences between animal and human model. The blood pressure range of mice and humans exhibits a degree of similarity, with mice typically exhibiting a systolic pressure of 122 $mmHg$ and a diastolic pressure of 102 $mmHg$, compared to the human average of approximately 120/80 $mmHg$ (Mattson, 2001). However, despite these numerical similarities, significant physiological and scale-based distinctions persist between the two species that merit scrutiny. For instance, mice generally exhibit a significantly faster heart rate, often ranging from 500-700 beats per minute, in stark contrast to the human average of around 60-100 beats per minute. Meanwhile, the blood vessel thickness in mice and humans differs significantly due to the differences in body size and scale. For instance, in humans, the aorta (the main and largest artery in the human body) can have a wall thickness of 4 mm (Yoon et al., 2016). In comparison, the aortic wall in mice registers a thickness on the order of 10-100 μm (Wheeler et al., 2015). These physiological distinctions, particularly the marked discrepancy in the thinness of the blood vessel wall, suggest a more pronounced severity of Hematoma Transformation (HT) in mice relative to humans.

This HT model proposed here was established by making a series of assumptions in order to simplify calculations and to be able to obtain key parameters. The vasculature network was reproduced by Payne and Lucas (2018) to develop an oxygen delivery model. Two major assumptions are made in this network. One underlying approximation is that each parent vessel branches into two child vessels (and that two

vessels with the same geometry combine in one venous vessel). However, based on anatomical studies, capillaries have a more web-like than tree-like structure. In addition, the geometries of child vessels are assumed to be the same. However, vessel branches have various diameters, length, wall thickness, etc, which will introduce additional variability into the model results.

In the haemorrhage scenario in the brain, multiple vessels can of course leak simultaneously. The haemorrhage caused by one microvascular vessel could be affected by the surrounding circulations and tissue displacement. In this simulation, brain tissue is assumed to be homogeneous. Thus, in calculations, the hydraulic conductivity k is the same for haemorrhage in the tissue region. The interactions between the neighbouring vessels should be considered carefully when enlarging the model scale. The haemorrhage model applied in different cerebral regions should also be adjusted and modified due to spatially varying mechanical parameters of the tissue.

It will be thus necessary to extend this model to an enlarged vasculature length scale. The next vasculature models that will be used are a series of 3-dimensional human cerebral microvascular networks (cube size from $125\,\mu m$ to $625\,\mu m$) presented by El-Bouri and Payne (2015). By assuming the inlet blood pressure and blood flowrate and combining the geometric properties, the haemodynamics of blood flow can be determined. Meanwhile, the interaction of the tissue pressure distribution between neighbouring blood vessels needs to be considered. This interaction will also require multiple simulations due to the statistical nature of the network. It is necessary to explore the effects of increased interstitial pressure on the flow in surrounding vessels,

i.e., whether one leaky vessel is enough to start to block flow in the surrounding circulation. This will be the subject of a future study.

3.5 Conclusion

Through the development of a mathematical model to simulate the severity of HT in the microvasculature, it is possible to simulate the severity of HT and the effects of capillary compression. This study has identified that the haematoma radius is largely invariant of the vessel geometry. The model thus indicates that arterioles and venules are able to cause larger volumes of haematoma than the capillary generation. One of the more significant findings to emerge from this study is that capillary compression has been shown to have a greater impact on venules than on arteriole and capillary generations. Meanwhile, this study has found that capillary compression is able to reduce the leakage fraction of blood flow and hence to restrain the development of a haematoma. The solutions and insights gained from this study may be of assistance to assess the impact of the HT on a 3D tissue region and at a whole-brain scale.

3.6 Evaluating the Model: Advantages and Limitations

It is necessary to discuss whether the three main goals of this whole study (from a modelling perspective, a physiology perspective, and a clinical perspective) have been answered. In addition, a summary of assumptions for this chapter is listed in Table 1.1.

Table 3.2. Model accomplishments and limitations

Model:	HT in the microvasculature
Objectives:	Modelling objective
Completed aspects:	• Governing mathematical equations to describe HT in a single vessel has been developed. This model can work as a starting point for the whole HT model.
Unfinished aspects and limitations:	• Key clinical indicators, for example, cerebral blood volume, are challenging to acquire from this model and compare with clinical data.
Objectives:	Physiology objective
Completed aspects:	• Breakdown of BBB in a HT model in a single vessel has been described by a mathematical model. • Tissue mechanics are considered into the model.
Unfinished aspects and limitations:	• The BBB breakdown is assumed to be a uniform process, with an evenly distributed leakage. Further study for simulation of BBB breakdown needs to be down from microscopic view. • The tissue is assumed to be a homogeneous material. Variation of tissue mechanics, such as tissue pressure, needs to be investigate in the future study. • The interaction of the tissue pressure distribution between neighbouring blood vessels needs to be considered. Implementation of a vasculature model is suggested for future investigations to facilitate validation with clinical data. • To integrate this model within an expanded vasculature

	model or alternative blood vessel model, it should be considered that certain specific input parameters fluctuate among distinct blood vessels. These parameters, including vessel geometries, blood flow rate, blood inlet pressure, tissue pressure, among others, highlight the requisite adaptation that is needed when applying the model to various vascular contexts. • One of the most crucial parameters, the definition of haematoma surface pressure, presents a significant challenge for validation.
Objectives:	Clinical objective
Unfinished aspects and limitations:	• The current model is limited to be assist clinicians to predict HT after stroke yet, unless the model is presented in a whole brain model in future.

3.7 Appendix

Appendix 3.A Supplementary for the Green's Function

Green's function is applied again to simulate the pressure drop from the capillary to the tissue. Begin with the divergence theorem (Katz, 1979):

$$\int_V \nabla A \, dV = \int_S A \, d\hat{\sigma} \tag{A. 3.1}$$

Then it yields,

$$A = \varphi \nabla \psi - \psi \nabla \varphi \tag{A. 3.2}$$

$$\nabla A = \varphi \nabla^2 \psi - \psi \nabla^2 \varphi \tag{A. 3.3}$$

Then Eq. (A. 3.3) is plugged into the divergence theorem yields

$$\int_V (\varphi \nabla^2 \psi - \psi \nabla^2 \varphi)\, dV = \int_S (\varphi \nabla \psi - \psi \nabla \varphi)\, d\hat{\sigma} \qquad \text{(A. 3.4)}$$

The next step is let the linear differential operator $L_o = \nabla^2$ and based on definition of Green's function (Bayın and Bayin, 2006):

$$L_o G(x, x') = \nabla^2 G(x, x') = \delta(x - x') \qquad \text{(A. 3.5)}$$

Then $\psi(x') = G(x, x')$ is confirmed and Eq. (A. 3.5) is substituted:

$$\int_V [\varphi(x')\delta(x - x') - G(x, x')\nabla'^2 \varphi(x')]\, dx' = ¿$$

$$\int_S [\varphi(x')\nabla' G(x, x') - G(x, x')\nabla' \varphi(x')]\, dS' \qquad \text{(A. 3.6)}$$

Rewrite Eq. (A.6) and set $\varphi(x')$ at one side yields

$$\varphi(x') = \int_V G(x, x')\nabla'^2 \varphi(x')\, dx' + \int_S [\varphi(x')\nabla' G(x, x') - G(x, x')\nabla' \varphi(x')]\, dS' \qquad \text{(A. 3.7)}$$

In this model, $\varphi(x') = p_i(x')$.

$$p_i(x') = \int_V G(x, x')\nabla'^2 p_i(x')\, dx' + \int_S [p_i(x')\nabla' G(x, x') - G(x, x')\nabla' p_i(x')]\, dS' \qquad \text{(A. 3.8)}$$

where

$$\int_S G(x, x')\nabla' p_i(x')\, dS' = \int_V G(x, x')\nabla'^2 p_i(x')\, dx' = \int_S \delta(x - x')\, d^3 x' = 1 \qquad \text{(A. 3.9)}$$

Appendix 3.B Viscosity vs. haematocrit

To calculate the blood viscosity in small vessels, Pries and Secomb (2005) developed empirical equations based on experimental data:

$$\mu_{vitro} = \mu_p \left[1 + (\mu_{0.45} - 1)\frac{(1 - H_D)^C - 1}{(1 - 0.45)^C - 1}\right] \qquad \text{(B. 3.1)}$$

where

$$\mu_{0.45} = 220\, e^{-1.31D} + 3.2 - 2.44\, e^{-0.06\, D^{0.645}} \quad \text{(B. 3.2)}$$

and

$$C = \left(0.8 + e^{-0.075\, D}\right)\left[-1 + \left(1 + 10^{-11} D^{12}\right)^{-1}\right] + \left(1 + 10^{-11} D^{12}\right)^{-1} \quad \text{(B. 3.3)}$$

$$\mu_{vivo} = \mu_{vitro}\left(\frac{D}{D_{eff}}\right)^{4} \quad \text{(B. 3.4)}$$

where $\mu_p$denotes blood plasma viscosity ($1.2\, mPa \cdot s$), μ_{vitro} is the in-vitro blood viscosity and $\mu_{vivo}$is the in-vivo blood viscosity. $D$is the diameter of the blood vessel and H_D is the discharge haematocrit (0.45) (Linninger et al., 2013, Guibert et al., 2012).$\mu_{0.45}$ is the relative blood viscosity for blood haematocrit of 0.45 and D_{eff} denotes and the thickness of the endothelial surface layer.

Appendix 3.C Haematoma formation time vs. haemostasis

Haematoma formation time can be calculated based on the value of k, hydraulic conductivity, which is equal to $5 \times 10^5\, \mu m^3 s k g^{-1}$ in this model, to calculate the time for blood to reach the boundary of the haematoma:

$$u = \frac{\Delta P \times k}{R} \quad \text{(C. 3.1)}$$

where $u$denotes the average velocity of blood flow in tissue, ΔP denotes the pressure difference between the central and exterior surfaces of the haematoma and R denotes the haematoma radius.

$$u = \frac{\Delta P \times k}{R} = \frac{4\, mmHg \times 5 \times 10^5\, \mu m^3\, s k g^{-1}}{150\, \mu m} = 1.78\, \mu m/s \quad \text{(C. 3.2)}$$

The formation time, T, can then be estimated as:

$$T = (\Delta P \times k)^{-1} = \frac{R}{u} = \frac{150\,\mu m}{1.78\,\mu m/s} = 84.4\,s = 1.4\,mins \qquad \text{(C. 3.3)}$$

Thus, the approximate haematoma formation time in this model is concluded of order 1 minute.

Nekludov et al. (2007) measured the IVY bleeding time of both traumatic brain injury (TBI) patients ($674\,s \pm 230\,s$, approximately $11.2\,mins$) and healthy controls ($320\,s \pm 95\,s$, approximately $5.3\,mins$), and Tsitsopoulos et al. (2020) used less than $600\,s$ of bleeding time as a threshold of normal bleeding time. These measurements of haemostasis are at least 3 times slower than the formation time of a haematoma.

In addition, secondary HT is a side-effect of the use of thrombolytic therapy that uses recombinant tissue-plasminogen activator (rt-PA) to treat ischaemic stroke. rt-PA has been shown to inhibit the platelet aggregation that will increase the haemostasis time significantly and to lead to an increased bleeding risk (Stricker et al., 1986, Tanne et al., 2006, Loscalzo and Braunwald, 1988). Montoney et al. (1995) found that tissue-type plasminogen activators prolong primary bleeding to double the baseline values in their rabbit model. Mihara et al. (2005) also showed that a high dose of rt-PA significantly prolonged bleeding time, approximately $15\,mins$, with a ratio of 2.3 when compared to healthy pigs.

Thus, in the HT simulations presented here that haematoma formation occurs sufficiently fast enough that haemostasis does not occur until equilibrium is obtained. Under conditions of rt-PA treatment, the time to haematoma formation is found of order 10 times faster than haemostasis.

Appendix 3.D Pseudo-algorithms

Input: Microvasculature Model (M) reproduced by Payne and Lucas (2018) and mesh
Output: { $p_c(l^j)$ }, {D}, {blood flowrate}, { L }, { μ } (all parameters here are in health condition)

Initialize: Guess a leakage rate { γ } in a reasonable value & guess { $p_{io}(l^j)$} with a constant value=15 mmHg

For loop with the intention of iterating $\{L_p\}$ $i = 1\ to\ 10$:

- Output: D, blood flowrate, L, μ (all parameters here are in bleeding condition)
- Compute: {pressure drop}, $\{\delta\}$, $\{\lambda\}$ with equation (3.14) and Model (M)
- Compute: $\{p_c(l^j)\}$ using equation (3.14)
- Compute: $\{L_p\}$ using equation (3.29)
- Output: New $\{p_{io}(l^j)\}$ using equation (3.18)
- Output: New $\{L_p\}$ using equation (3.29)

End for loop

Input: New $\{L_p\}$
Output: New $\{\gamma\}$ using equation (3.9)
Compute: tissue pressure distribution after HT $\{p_i(\boldsymbol{x})\}$ using equation (3.26)

// Equation (3.26) can be coded as:

$$// \ p_i(\boldsymbol{x}) = P_o + \frac{D}{4}\sum_{j=1}^{Ne} \frac{R \times p_{io\,j}}{\left[(Z-Z_j')^2+R^2\right]^{1.5}} \quad \text{(D.3.1)}$$

Input: the definition of haematoma surface pressure ($\{P_{15.1}\}$, $\{P_{15.5}\}$ & $\{P_{99}\}$)
For loop with the intention of computing haematoma radius $\{R_j\}$, $i = 1\ to\ Ne$

- Find the Haematoma boundary by using min (abs ($p_i(\boldsymbol{x})$- the definition of haematoma surface pressure))

End for loop

Compute: $\{V\}$ using equation (3.28)

// Note #1: The computational cost is about 5 mins to 1 blood vessel (1 NVIDIA GeForce 3070 Ti)
// Note #2: The discussion of the convergence is discussed in next chapter (#4) since the governing equations and key algorithms are the same.

1

Chapter 4: Mathematical modelling of haemorrhagic transformation within a multi-scale microvasculature network

The work presented in this chapter is reproduced from: J. Wang, K. R. van Kranendonk, W. El-Bouri, C. B. Majoie, and S. J. Payne, "Mathematical modelling of haemorrhagic transformation within a multi-scale microvasculature network," Physiological Measurement, 2022.

Contributor Roles Taxonomy:

Jiayu Wang: Methodology, Software, Validation, Writing - Original Draft, Visualization.
Dr. Katinka R. van Kranendonk: Investigation, Writing - Review & Editing.
Dr. Wahbi El-Bouri: Software, Writing - Review & Editing.
Prof. Charles B. L. M. Majoie: Supervision, Writing - Review & Editing.
Prof. Stephen J Payne: Supervision, Conceptualization, Writing - Review & Editing.

4.0 Abstract

Objective

Haemorrhagic transformation (HT) is one of the most common complications after ischaemic stroke caused by damage to the blood–brain barrier (BBB) that could be the result of stroke progression or a complication of stroke treatment with reperfusion therapy. The aim of this study is to develop further a previous simple HT mathematical model into an enlarged multi-scale microvasculature model in order to investigate the effects of HT on the surrounding tissue and vasculature. In addition, this study investigates the relationship between tissue displacement and vascular geometry.

Approach

By modelling tissue displacement, capillary compression, hydraulic conductivity in tissue and vascular permeability, a mathematical model is established to describe the change of intracranial pressure (ICP) surrounding the damaged vascular bed after HT onset applied to a 3D multi-scale microvasculature. A voxel-scale model is used to compare

this HT simulation with available clinical imaging data for perfusion and cerebral blood volume (CBV) in the multi-scale microvasculature network.

Main results

It is shown that the haematoma diameter and the maximum tissue displacement are approximately proportional to the diameter of the breakdown vessel. Based on the voxel-scale model, perfusion reduces by approximately $13-17\%$ and CBV reduces by around $20-25\%$ after HT onset due to the effect of capillary compression caused by increased interstitial pressure. The results are in good agreement with the limited experimental data.

Significance

This model, by bridging the gap between the microvascular scale and clinically measurable parameters, provides a foundation for more detailed validation and understanding of HT in patients.

Connections to prior research

This model builds upon previous HT studies by evolving from a 2D vasculature network to a 3D penetrating network model. This advancement allows the researchers to investigate the interactions between a ruptured blood vessel and its neighbouring vessels, as well as validate their findings with accessible clinical indicators, such as perfusion and CBV.

4.1 Introduction

Stroke was ranked as the second leading cause of death across the world in 2010 (Lozano et al., 2012, Iadecola et al., 2020). With an increasingly elderly global population, the incidence of stroke is predicted to increase. Ischaemic stroke and haemorrhagic stroke are classified as the two main types of stroke based on their pathology. According to a study by Snarska et al. (2016), the ratio of ischaemic stroke to haemorrhagic stroke is $4.8:1$. In the context of ischaemic stroke however, it is also important to consider haemorrhagic transformation (HT), since this is a frequent, often asymptomatic, complication after acute ischaemic stroke onset (Álvarez-Sabín et al., 2013), and one that can lead to long-term morbidity and mortality (Marsh et al., 2013). Tan et al. (2014) reported that spontaneous HT was observed in 50 of 407 patients (12.3%) and HT was observed in 29 patients (12%) in the study by Terruso et al. (2009). HT is usually classified according to the European Cooperative Acute Stroke Study II (ECASS II) classification based on radiological appearance (Milloy and Wood, 2015). This classification divides HT into four types: haemorrhagic infarction type 1 (HI1), which is defined as small petechiae along the peripheral margins of infarct; haemorrhagic infarction type 2 (HI2), defined as confluent petechiae within the infarcted area but without mass effect; parenchymal hematoma type 1 (PH1) as blood clots in $\leq 30\%$ of the infarcted area with some slight mass effect; and parenchymal hematoma type 2 (PH2) as blood clots in $¿30\%$ of the infarcted area with substantial mass effect (Milloy and Wood, 2015).

HT is caused by disruption of the blood–brain barrier (BBB) and can result in significant damage to brain tissue. However, HT can also occur as a complication of stroke treatment with thrombolytic therapy (Group, 1996) and often BBB breakdown can be caused by the combination of severe ischaemic stroke and thrombolytic therapy (Lakhan et al., 2013). The functional outcome of patients with HT varies, however patients with large hematomas are most likely to have a poor functional outcome (van Kranendonk et al., 2019).

A key question to answer is whether HT can be predicted accurately after ischaemic stroke, based on available imaging data and other clinical parameters. Wang and Payne (2021) recently proposed a mathematical model that aimed to compare the severity of haemorrhage over a range of length scales and to investigate the effects of capillary compression on HT as the first step towards this objective. They established this simulation on a 2D vasculature model and assumed that the geometries of vessels in the same generation were the same. However, based on anatomical studies, capillaries have been shown to have a more web-like than tree-like structure. In addition, in the previous model, only one isolated vessel was assumed to be permeable and the effect of HT on neighbouring vessels was not considered.

It is thus necessary to extend this model to an enlarged vasculature length scale since it can be used to compare this HT model more accurately with the human vasculature. Various small-scale models (length scale order $\leq 100\,\mu m$) have been developed based on both human and rat cerebral vasculatures (Fang et al., 2008, Secomb et al., 2000, Su et al., 2012, Safaeian and David, 2013). However, these small models are limited by the

difficulties of validation with clinical imaging, which is obtained at a voxel length scale (order 1 mm). In turn, large-scale models are mostly based on animal models (Gagnon et al., 2015, Schmid et al., 2017, Gould et al., 2017). Many differences between animal and human vasculatures exist. For example, there are more penetrating venules than penetrating arterioles in the rat cortex, while human brains have the opposite ratio (Blinder et al., 2010, Schmid et al., 2019).

Human microvasculature models are still poorly understood, due to the lack of physiological data and limited high-resolution imaging data. One blood flow model was generated by Lorthois et al. (2011) based on human cerebral data (Cassot et al., 2006) and it was shown that the simulation of blood flow highly depends on the prescribed boundary conditions of the vascular architecture. In addition, Linninger et al. (2013) also used the same cerebral data to develop a large-scale vasculature model. In their simulation, the penetrating vessels were not generated by direct physiological data. El-Bouri and Payne (2018) thus subsequently developed a multi-scale microvasculature model of the human cerebral cortex based on morphological data. They validated this model by calculating the cerebral blood flow (CBF) for voxels.

The aim of this study is to develop a model which is able to simulate the severity of haemorrhage in penetrating networks. The previous mathematical model proposed by Wang and Payne (2021) is used as a starting point to simulate the haematoma formed from a single straight vessel. This mechanical model is then applied to the vasculature model generated by El-Bouri and Payne (2018). Properties such as cerebral blood volume (CBV) and perfusion rate are estimated and compared with clinical imaging

data. Due to the increase in intracranial pressure (ICP) after HT, the effects of capillary compression are also considered in the vasculature, both in the damaged vessel and in other healthy vessels (Bordoni et al., 2020). In addition, tissue displacement caused by the breakdown of BBB is calculated, using the methods proposed by Mokhtarudin and Payne (2015).

4.2 Materials and methods

The steps to simulate HT in this model are most conveniently split into two parts. In the first part, a simple model for one isolated penetrating vessel is considered as a starting point. This first part deals with the governing equations to investigate the mathematical modelling of both the penetrating vessels and the haematoma. The second part concerns the effects of the network haemodynamics, including the behaviour of CBV, perfusion and tissue displacement.

4.2.1 Model formulation

4.2.1.1 Haemodynamics

An isolated vessel is considered at the beginning, following the approach set out in Wang and Payne (2021). They simulated HT in a vascular model by assuming that blood vessels are completely permeable. In contrast, only the middle third of the vessel is assumed permeable in this study since the whole vessel is not thought to be leaky in HT and this also avoids the edge effects at the connections with neighbouring vessels. Fundamentally, this assumption allows the haematoma to form with having to worry about the effects of vessel connections (where it would be difficult to make sensible

assumptions about the vessel behaviour). In clinical reality, every segment of the blood vessel possesses the potential to become permeable and result in haemorrhage.

Hence, this assumption can be used to investigate the effect of capillary compression on the impermeable left third and right third due to increasing ICP, as shown in Figure 4.1. The vessel is divided into $3 \times Ne_h$ cylindrical elements, where $j = 1, \ldots, Ne_h, \ldots, 2Ne_h, \ldots, 3Ne_h$. In addition, the surrounding tissue is divided into Ne_v elements along its axial direction, where $i = 1, \ldots, Ne_v$. Pozrikidis and Farrow (2003) selected 96 elements for a capillary vessel. Thus, in this simulation, $Ne_h = Ne_v = 100$ is set to obtain a good balance between computational expense and model accuracy: this keeps the impact of adjustment of the node coordinate points in the penetrating network to fit the grid intersection to less than 1% (this adjustment will be discussed later in this section). In this simulation, the HT in arterioles with different diameters, from $15\,\mu m$ to $250\,\mu m$ but with the same length is modelled to quantify haematoma volume and tissue displacement. The depth of cerebral cortex is suggested approximately to be $2.5\,mm$ (Duvernoy et al., 1981). Thus, a typical penetrating vessel length is chosen to be $1.25\,mm$ in this simulation.

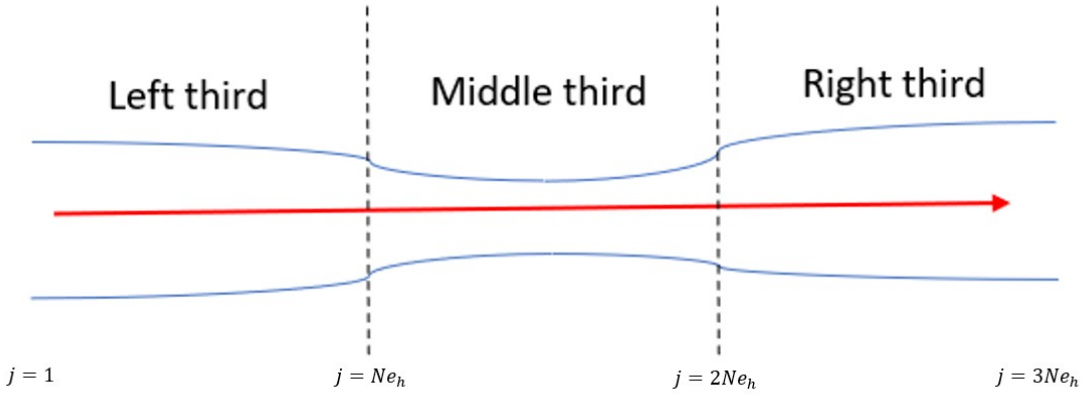


Figure 4.1. Schematic of single vessel model. The middle third of the vessel is assumed to be permeable with the remainder assumed impermeable. The resulting convexity of the capillary is due to the effects of capillary compression, as shown previously (Wang and Payne, 2021). Red arrow denotes the direction of blood flow.

Wang and Payne (2021) established a series of governing equations to calculate blood flowrate Q, capillary pressure p_c and tissue pressure distribution p_i (Eq. 4.1) for HT in an isolated permeable vessel and identified the haematoma boundary through setting a pressure boundary condition:

$$p_i(x) = P_o + \frac{D}{4}\int_s p_{io}(x') \frac{|R - R'|}{\left(|Z - Z'|^2 + |R - R'|^2\right)^{\frac{3}{2}}} dZ' \tag{4.1}$$

where P_o denotes the far-field interstitial pressure, D denotes the diameter of the vessel, S denotes the surface area of the vessel, p_{io} denotes the exterior interstitial pressure, point x in tissue can be defined as $x = (Z, R, \theta)$ and thus, $x' = (Z', R', \theta')$, where the **Z** axis is the direction along the capillary, the R axis is the radial direction and θ is the angle of rotation. The origin of the coordinate system is set at the inlet centre point of the vessel. In addition, the definition for the haematoma boundary used here is based on that proposed by Wang and Payne (2021): thus, a value set at 0.1 mmHg

above P_o ($P_o = 15\,mmHg$). This definition of haematoma is chosen as it gives results that seem to be the closest to the experimental data measured by Jenkins et al. (1989) in that the distance in mice between the edge of a haematoma and related damaged vessels is approximately $700\,\mu m$.

4.2.1.2 Capillary compression

Wang and Payne (2021) discussed the effects of capillary compression based on experimental data (Bordoni et al., 2020). However, this approach is less suitable to determine the capillary compression for large arterioles ($D > 25\,\mu m$). Arteriolar diameters are typically found in the range $15-240\,\mu m$ and venule diameters in the range $20-125\,\mu m$ (Duvernoy et al., 1981). Thus, the more general relationship between pressure and cross-sectional area of the capillary (collapse equation) developed by Drzewiecki et al. (1997) is used here to simulate vessel compression:

$$\Delta P = \frac{-E\,h_b^{\,3}}{9\,r_{mb}^{\,3}}\left[\left(\frac{A_b}{A}\right)^n - 1\right] \tag{4.2}$$

where $\Delta P = p_c - p_{io}$ denotes transmural pressure, E denotes wall elastic modulus, h_b denotes vascular wall thickness at maximum compliance point, r_{mb} denotes the vessel lumen radius at its maximum compliance point, A_b denotes the vessel lumen cross-sectional area at its maximum compliance point, A denotes vascular lumen cross-sectional area and n denotes the constant that defines the degree of curvature of the pressure-area relationship. In this simulation, measurements from the canine carotid artery and jugular vein have been selected to determine the compression model for arterioles and venules in penetrating networks, as shown in Table 4.1.

Table 4.3 Vascular measured characteristics

Vascular Type	E	h_b	n
Canine carotid artery (Drzewiecki et al., 1997)	$29.2\,mmHg$	$0.787\,mm$	3.380
Canine jugular vein (Drzewiecki et al., 1997)	$9530.0\,mmHg$	$0.401\,mm$	0.137

4.2.1.3 Tissue displacement

To determine the tissue displacement after HT onset, the equations developed by Mokhtarudin and Payne (2015) were used, assuming quasi steady state based on the fact that the tissue displacement process occurs slowly with negligible inertial effects (Terzaghi, 1943):

$$\nabla^2 U - \omega \nabla p_i = 0 \tag{4.3}$$

$$\omega = \alpha^w / ¿ \tag{4.4}$$

where U denotes tissue displacement, α^w denotes the Biot parameter for water, G is the shear modulus and v' is Poisson's ratio. ω can thus be calculated to be $0.001\,Pa^{-1}$. The values used here are given in Table 4.2.

Table 4.4 List of parameters and their baseline value for the proposed model.

Parameter	Model values	Reference
Biot parameter for water network, α^w	1	Tully and Ventikos (2011)
Shear modulus, G	$216.3\,Pa$	Mokhtarudin and Payne (2015)
Poisson's ratio, v'	0.35	Drake et al. (1996)

4.2.2 Network model

The penetrating network model used in this simulation is directly taken from El-Bouri and Payne (2018). They used a statistically representative large-scale model

$(1 \times 1 \times 2.5\,mm)$ to investigate the effects of a penetrating vessel occlusion on blood flow and blood pressure in the human cortex. To extend this model, a $1 \times 1 \times 2.5\,mm$ voxel is repeated 4 times to give a final volume of $2 \times 2 \times 2.5\,mm$ in order to fully present the appearance of the haematoma in the network (this is required since the maximum haematoma radius obtained by Wang and Payne (2021) is larger than $500\,\mu m$), as shown in figure 4.2.

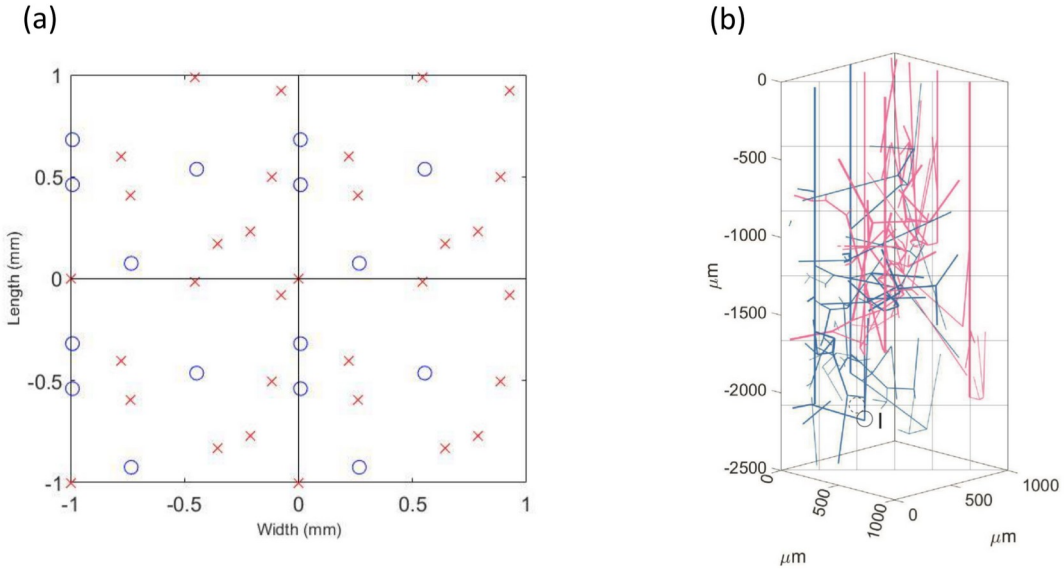


Figure 4.2. (a) Top-down view of a $2 \times 2 \times 2.5\,mm$ voxel, split into 4 quadrants each containing 8 arterioles and 4 venules. Red crosses represent arterioles and blue circles represent venules. (b) A fourth example voxel show half the penetrating vessels for easier viewing. The penetrating vessels enter from the pial surface into the grey matter. The diagonal length of the horizontal plane is $\sqrt{2}\,mm$

The penetrating vessels descend into the cerebral cortex from the pial surface. Arteriolar pial pressure is assumed to be $90\,mmHg$ and venule pial pressure is set to be $25\,mmHg$, since arteriole pial pressure is in the range $65-90\,mmHg$ and venule pial pressure in the range 15 to $25\,mmHg$ (Stromberg and Fox, 1972, Tamaki and Heistad,

1986). Thus, $90\,mmHg$ and $25\,mmHg$ are chosen here to show a relatively severe scenario. The total pressure drop for arterioles is assumed to be $35\,mmHg$, and for venules, the total pressure drop is assumed to be $15\,mmHg$ (Zweifach and Lipowsky, 1977). In each $1\times1\times2.5\,mm$ voxel, it is assumed that there are 12 starting points of penetrating vessels in the ratio 2:1 arterioles-to-venules, all randomly distributed across the surface.

In this simulation, the height of the $2\times2\times2.5\,mm$ voxel is divided into $6\times Ne_h$ elements since the height of the voxel is double the length of the single vessel simulated previously. Taking the central axis of the cuboid as the centre, the $\sqrt{2}\,mm$ radius (diagonal length in figure 4.2(b)) is divided into Ne_v elements. Each node in the vasculature is adjusted slightly to fit the grid intersection. For example, node I (solid black circle) in figure 4.2(b) is adjusted to the dashed black circle above. The impact of this adjustment can be neglected, since the results of CBV and perfusion rate are both found to change by less than 1% based on these simulations (results not shown).

It is then assumed that HT occurs in the penetrating arteriole in the centre of the $2\times2\times2.5\,mm$ voxel. This is based on the results of Thevathasan et al. (2018) who have shown that the cortical involvement rate is 93% for HT patients, i.e., that the rate that HT occurs in the penetrating network is high, indicating to assume that the HT occurs in the largest vessel in this model. The middle third of this vessel is set to be permeable with the remainder impermeable, to be consistent with the previous model. In this simulation, the diameter of arterioles and venules are set to be $40\pm8\,\mu m$ and $110\pm16\,\mu m$ respectively. Ten geometrically representative voxels were used to calculate

the changes in perfusion rate and CBV in response to HT. These two parameters were selected as they can be measured at a voxel length scale using a number of imaging modalities, such as computed tomography perfusion (CTP).

The perfusion, F can be calculated by using the pressure drop and total resistance:

$$F = \frac{Q \times 60 \times 100}{V_t \times \rho} \tag{4.5}$$

where Q denotes the blood flow rate, calculated by summing the blood flow leaving the voxel (El-Bouri and Payne, 2016), V_t denotes the volume of tissue, ρ is cerebral tissue density $\left(0.96\, g\, cm^{-3}\right)$ (Dekaban and Sadowsky, 1978, Lüders et al., 2002), and factors of 60 and 100 are used in the equation to convert seconds to minutes and g to $100\, g$, respectively. Based on Eq. (4.2), the vascular diameter distribution D^jin each voxel can be determined. Then the CBV can be calculated:

$$CBV = \sum \left(D¿¿^j/2 \right)^2 L \times \frac{6\, Ne_h}{V_t \times \rho}¿ \tag{4.6}$$

where L denotes each vascular length in the voxel and $j = 1, \ldots, 6\, Ne_h$. In this simulation, haematoma is assumed to be of the form with no mass effect. The changes in CBV and F are due to capillary compression caused by increased ICP.

4.3 Results

4.3.1 Single vessel model

Using Eq. (4.1), the tissue pressure distribution p_i can be calculated for each vessel with diameters ranging from $15\, \mu m$ to $250\, \mu m$. By applying the proposed definition of the haematoma boundary, i.e., 15.1 mmHg, the haematoma radius and volume for each

simulation can be determined. Haematoma radius and volume were found to increase rapidly with vessel diameter, as shown in figure 4.3(a) and figure 4.3(c). When the vessel diameter is set to $15\,\mu m$, the maximum haematoma radius is $290.7\,\mu m$. The maximum haematoma radius for a $250\,\mu m$ diameter vessel is calculated to be $5.1\,mm$. Figure 4.3(b) shows, however, that the ratio of haematoma radius to vascular diameter is nearly constant for different diameter vessels: the ratio is approximately 20 over the leaky part of the vessel.

In this simulation, the haematoma volume is found to be $0.097\,mm^3$ when the arteriole diameter is set to $15\,\mu m$ and is calculated to be $62.3\,mm^3$ for $250\,\mu m$ arteriole diameter, showing a very wide range of values and a very strong sensitivity to the vessel diameter. The characteristic length of the haematoma is shown in figure 3(d): characteristic length increases sharply between the small and large vessels, diameter ¿$25\,\mu m$ (slope¿22780) and ¿$200\,\mu m$ (slope ¿6100) but remains approximately constant over the diameter range $25\,\mu m$ to $150\,\mu m$, as shown in Figure 4.3(d).

As shown in figure 4.3(e), larger arteriolar diameter leads to larger maximum tissue displacement, as would be expected. In this simulation, the maximum tissue displacement for each vessel is in the order of $10^0\,\mu m$. The slope of the maximum tissue displacement and vessel diameter is close to 0.04 ($R^2 = 0.995$). Combinations of vector and contour plots of tissue displacement are also shown in figure 4.4(b), 4.4(e) and 4.4(h) to show the distribution of tissue displacement for different arteriolar diameters. Tissue displacement, as expected, is found to point from high pressure positions to low pressure positions. Note that tissue displacement is a vector that follows the same

direction as the pressure field. It can be seen, therefore, that the tissue displacement is not perfectly radial to the vessel surface at the junction of the leaky part and non-leaky part, hence showing the need for a full 3-D simulation. Dimensionless tissue displacement for the $15\ \mu m$ diameter vessel is also shown in Figure 4.5.

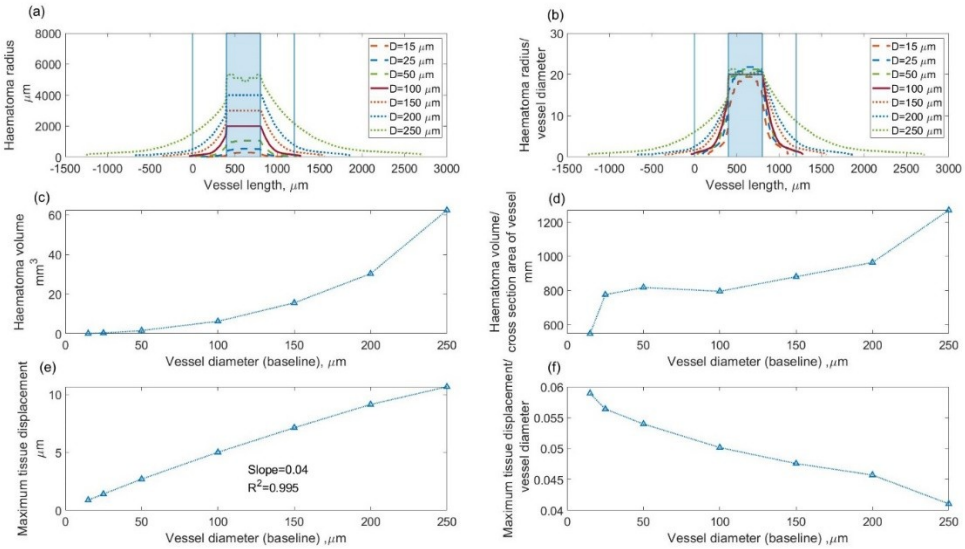


Figure 4.3. (a) Haematoma radius variation with axial length. The isolated vessel starts from $0\ \mu m$ to $1200\ \mu m$ and permeable section from $400\ \mu m$ to $800\ \mu m$. (b) The ratio of haematoma radius to vessel diameter varies with axial length. (c) Haematoma volume variation with vessel diameter. (d) Characteristic length variation with vessel diameter. (e) Variations in maximum tissue displacement in vessel diameter. (f) Ratio of maximum tissue displacement to vessel diameter behaviour with variable vessel diameter.

Figure 4.4(a), 4.4(d) and 4.4(g) show comparisons of variable vascular diameter along the axial length based on Eq. (4.2) for three different sized vessels. Larger vessels are compressed more due to larger exterior interstitial pressure (Wang and Payne, 2021). In addition, the vessel sections before and after the junctions of the leaky and non-leaky parts are also found to be compressed. The tissue pressure distributions are shown in

figure 4.4(c), 4.4(f) and 4.4(i) for different vessel diameters: $15\,\mu m$, $100\,\mu m$ and $250\,\mu m$, respectively. Larger leaky vessels lead to higher tissue pressure surrounding the vessel: presssure scale varies from $15-21\,mmHg$, $15-49\,mmHg$ and $15-76\,mmHg$ for different vessel diameters: $15\,\mu m$, $100\,\mu m$ and $250\,\mu m$, respectively.

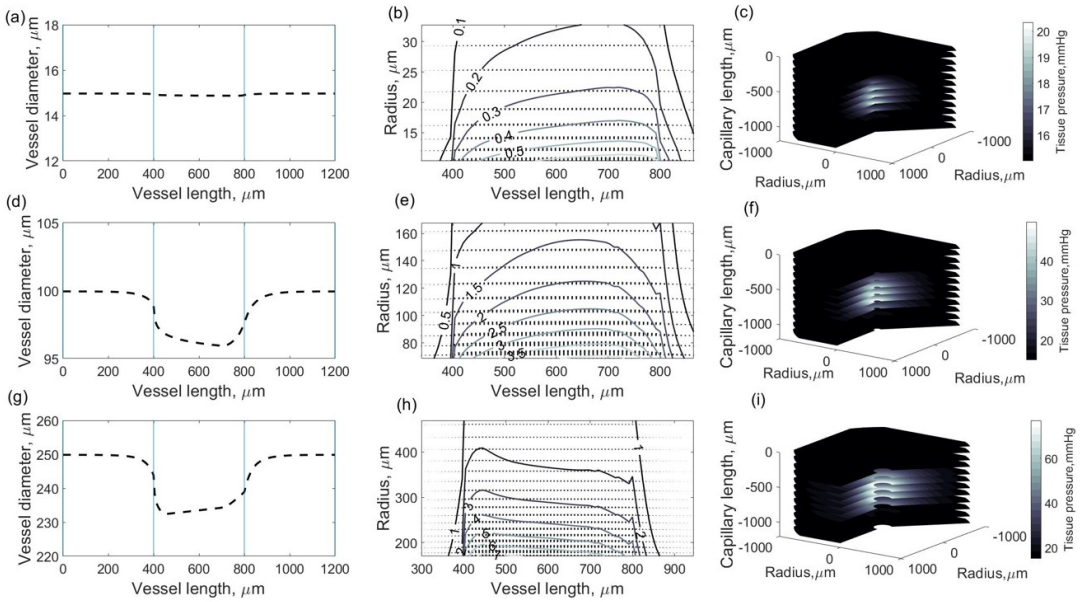


Figure 4.4. (a), (d) and (g): Vessel diameter variation with axial length, baseline diameter=$15\,\mu m$, $100\,\mu m$ and $250\,\mu m$ respectively. (b), (e) and (h): Combinations of vector and contour plots of tissue displacement, baseline diameter=$15\,\mu m$, $100\,\mu m$ and $250\,\mu m$ respectively. y axis represents the radial direction. The units for these contour plots are μm (c), (f) and (i): Slices of the pressure map, baseline diameter=$15\,\mu m$, $100\,\mu m$ and $250\,\mu m$ respectively. Note that the pressure axis is different in each simulation for ease of viewing.

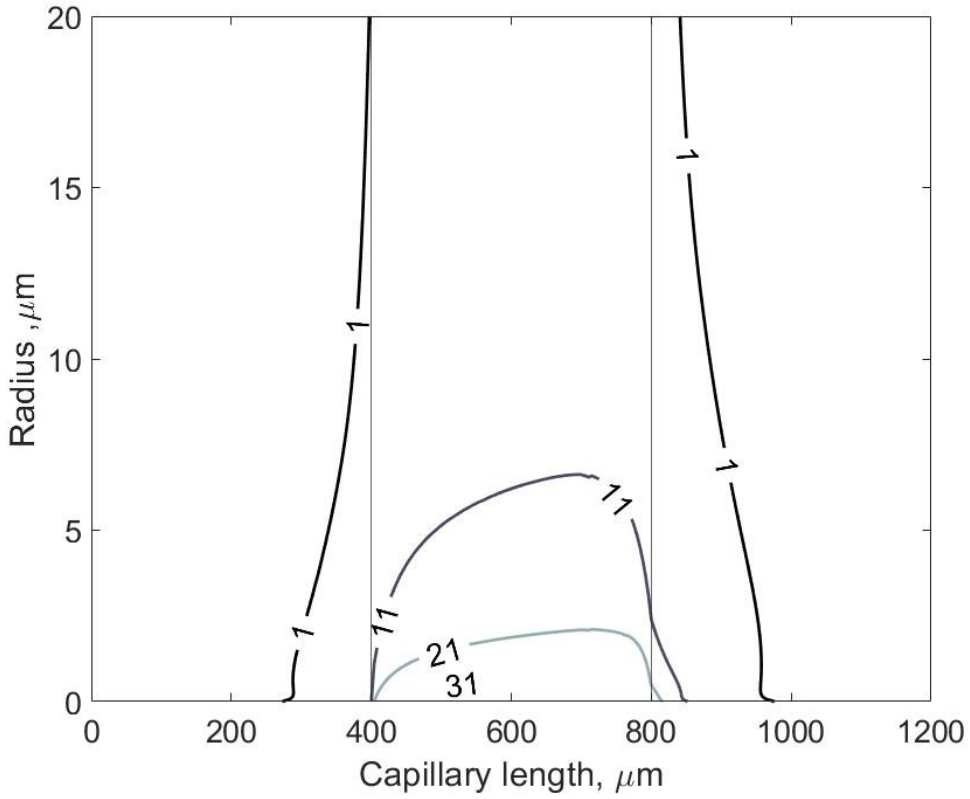


Figure 4.5. Contour plot of dimensionless tissue displacement. Values are given in percent.

4.3.2 Network model

HT in the voxel containing 32 arterioles and 16 venules are next simulated, an example of which is shown in figure 4.6. Ten simulations based on statistically accurate voxels of the penetrating vessels were run to determine the growth of HT. This $2 \times 2 \times 2.5\,mm$ voxel is found fully to contain the haematoma. In this voxel, the middle third of the central vessel is assumed to be permeable and this is the case for all simulations across the different vasculature networks in the different voxels.

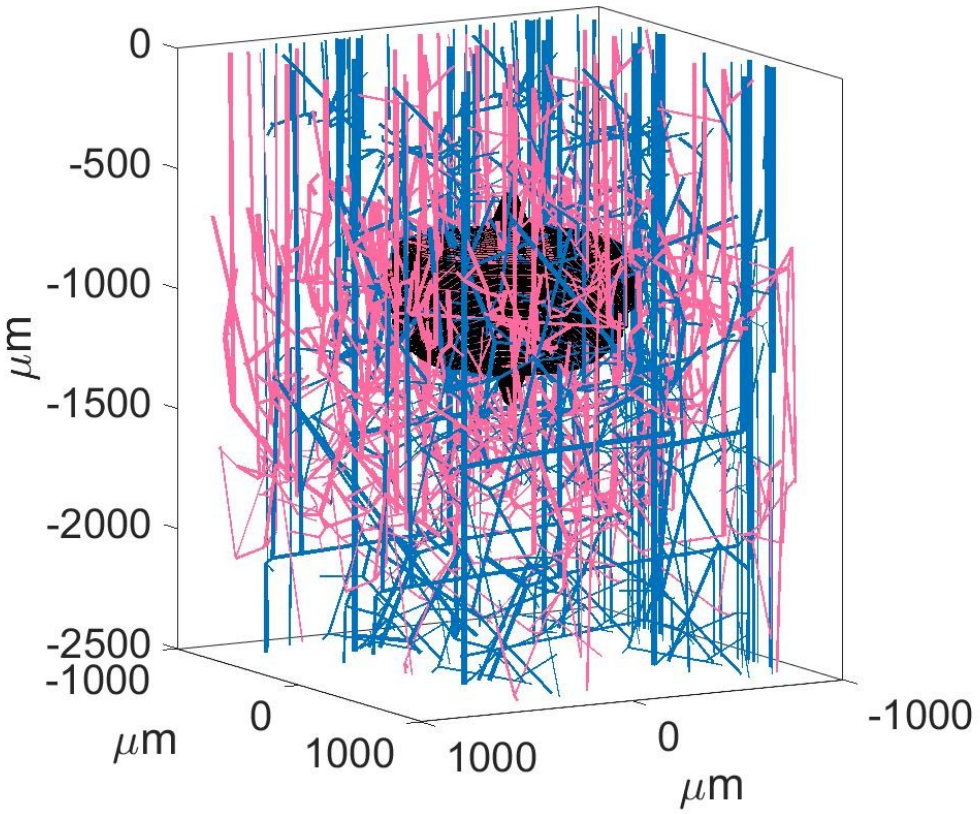


Figure 4.6. An example voxel showing a haematoma located at the middle third of the central penetrating arteriole. Red vessels represent arterioles and blue vessels denote venules. The penetrating vessels enter from the top pial surface into the grey matter, coupling to the capillary bed continuum via the terminal vessels.

In these simulations, the ranges of CBV before HT and after HT in these voxels are found in the range of $15-32 mL/100\,g$ and $11-23\,mL/100\,g$ respectively. As shown in figure 4.7(b), CBV reduces by around $20-25\,\%$ after HT onset. Perfusion is calculated by summing the flow leaving the terminal arterioles within the voxel boundary. Figure 7(b) shows that perfusion reduces by approximately $13-17\,\%$ after HT onset in the voxel, which is a smaller change than that exhibited by CBV.

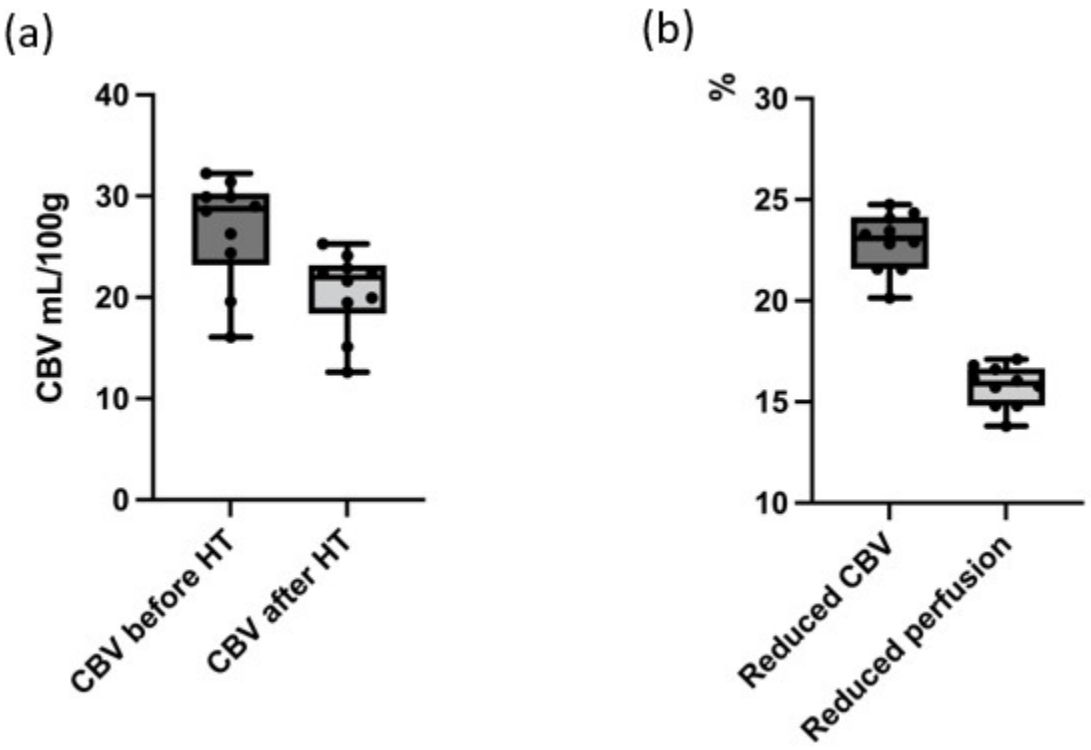


Figure 4.7. (a) Comparison of CBV before and after HT in voxel. (b) The percentage change of CBV and perfusion after HT.

4.4 Discussion

A HT model has been developed here in a microvasculature network model to investigate how cerebral haemodynamics can be affected after HT onset. This simulation is based on the model proposed by Wang and Payne (2021) that presents a mathematical model of HT after ischaemic stroke. They focused on how changes in vascular geometry can affect the severity of HT, thus they assumed that the whole vessel was permeable. To develop further these simulations, in the first part of this model only the middle third of the vessel is assumed to be permeable to determine the effect of HT on the remaining healthy vasculature. The haematoma diameter and the maximum tissue displacement are found approximately proportional to the diameter of

the breakdown vessel. Then in the second part of this simulation, changes in haemodynamics after HT onset in the 3D microvasculature were quantified, as these directly relate to parameters that can be measured at this voxel length scale. Based on the voxel-scale model, the prefusion is found to reduce by approximately $13-17\,\%$ and CBV is found to reduce by around $20-25\,\%$ after HT onset in a single penetrating vessel.

In the simulation for the single vessel, the left third and the right third of the vessel are both surrounded by the haematoma, i.e., blood diffuses to the tissue around healthy parts of blood vessels following the direction of high pressure to low pressure. Vessels with a larger diameter result in a larger haematoma radius and hence a longer diffusion path than smaller vessels, which also indicates that the high tissue pressure field volume is larger in larger leaky vessels than in smaller vessels. A larger high tissue pressure field volume seems to aggregate more blood and to cause a severe space-occupying effect. These results are similar to the results shown by Wang and Payne (2021), who concluded that the arterioles cause a larger haematoma radius and a larger leakage flowrate compared to capillaries. This result might help to explain the variable behaviour of HT, i.e., why some patients have HI1/HI2 and why other patients have PH1/PH2, dependent upon the type of leaky vessel. More work will be required to explore this effect and to link the model predictions with clinical imaging, however, following on from the classification proposed by von Kummer et al. (2015).

To the best of the author's knowledge, there are limited available experimental data that describe the development of a haematoma for an individual capillary after HT

onset. Jenkins et al. (1989) measured the distance between the haematoma boundary and related damaged vessels as $700\,\mu m$ in mice, which is well within this simulation's range of haematoma radius. The ratio of haematoma radius to vascular diameter is found to be approximately constant for the leaky part over a wide range of vessel radius, as shown in figure 4.3(b). However, the ratio is found to be larger for the tissue around the impermeable part of larger vessels than for smaller vessels.

The methods to investigate the capillary compression has been improved in this simulation compared with the model developed by Wang and Payne (2021), who used the experimental data by Bordoni et al. (2020). In their experiment, they set the cerebral perfusion pressure (capillary pressure in this HT case) to be $38.4\,mmHg$. Nevertheless, in this simulation, the capillary pressure is set to vary along the vessel and the inlet capillary pressure (arteriole pial pressure) to be $90\,mmHg$. In addition, Wang and Payne (2021) found that based on these experimental data, larger vessels (diameter ¿$23.97\,\mu m$) with higher blood flow rates have a higher leakage rate of blood and higher exterior interstitial pressure than smaller vessels, such that this situation may result in larger vessels becoming fully constricted. Even a mild constriction is able to cause a large effect on flow, due to the strong non-linearity in the viscosity-diameter relationship (Pries and Secomb, 2005).

Hence, the transmural pressure and cross-section area relationship for collapsible blood vessels proposed by Drzewiecki et al. (1997) is used here in this simulation. However, this method still contains limitations: in particular, the proposed model has yet to consider an autoregulation mechanism for variations in perfusion rate and interstitial

pressure. To the best of the author's knowledge, the mechanism of autoregulation in HT remains very poorly understood or quantified, and there is no model yet of how autoregulation behaves at this length scale, making it difficult to incorporate within this HT model (Strandgaard et al., 1973, Nakagawa et al., 2011). In particular, the balance between autoregulation in the arteriolar network and the capillary bed remains controversial and much more detailed experimental data will be required to understand better the response at an individual vessel scale. However, once more is known about the behaviour of autoregulation at this length scale, it will be possible to incorporate this within this HT model relatively straightforwardly.

The order of magnitude of maximum tissue displacement is about $1-10\,\mu m$ and the maximum dimensionless tissue displacement is approximately 30%. However, the experimental data of tissue displacement in HT are extremely limited. Mokhtarudin and Payne (2015) proposed that the maximum tissue displacement under condition of ischaemia–reperfusion varies from 0.97 to $7.21\,mm$ and that the dimensionless tissue displacement is approximately in the range of $0-25\,\%$, values which are in very good agreement with the those that is obtained here.

As shown in figure 4.7(b), a reduction in CBV is found following HT, in the range of $20-25\,\%$ and the perfusion also reduces by approximately $13-17\,\%$ after HT onset. Jain et al. (2013) compared the CT perfusion parameters for a control group and a HT group: the mean reduction rate of CBV is $19\pm6.8\,\%$ and the mean reduction rate of relative cerebral blood flow (rCBF) (reduction rate of perfusion in this HT case) is $10\pm4.3\,\%$, both of which are in reasonably good agreement with the results that is presented here. Seki

et al. (1985) proposed that a reduction in CBF to $50\,\%$ of normal could be considered as a critical value for HT development. Thereafter, they found CBF decreased rapidly. This indicates that in the next stages of model development, it will be important to include the time dynamics in the HT simulation.

In this study, results are found to be within the range of CBV and perfusion values found from experiments but lie within the top half of this range. It is suggested that this is the case because the arterioles are set to be leaky in this study, which can cause more severe HT since the blood pressure here is higher compared to the capillary and venous circulations. rCBF is calculated clinically from data collected on the ipsilateral side compared with the contralateral (healthy) side. Perfusion change in this study is calculated by the change in perfusion after HT onset compared with the healthy state. Perfusion and rCBF can therefore be assumed to directly equivalent in this case.

When haemorrhage occurs in a patient's brain, multiple vessels probably leak simultaneously and the leaky regions along the vessels are not certain. In this simulation, the middle third of the vessel is set to be permeable and the remainder to be healthy to develop further the model proposed by Wang and Payne (2021), where it was assumed that the whole vessel was leaky. It is straightforward to relax this assumption, but the main aim of this study is to determine how HT in a single vessel can affect the surrounding vessels and tissue. Pozrikidis and Farrow (2003) also used the same approach (the middle third of vessel being permeable) in their tumour simulations, which makes it easier to compare results from this study with those of Pozrikidis. Meanwhile, the middle third is chosen to avoid edge effects at the nodes

between blood vessels. The necessity of modelling the implications of this assumption for the entirety of the model is minimal, given that the progression of HT will not significantly alter due to variations in the length of right and left vessels deemed non-permeable, as long as edge effects are effectively mitigated. In addition, the haemorrhage caused by one microvascular vessel can be affected by the surrounding circulation. However, the tissue surrounding the penetrating network is assumed to be homogeneous. The haemorrhage model applied in different regions should be adjusted due to the spatially varying mechanical parameters of the tissue.

In this simulation, the formation of haematoma is assumed to be fast enough such that haemostasis does not occur. Wang and Payne (2021) calculated that the time to haematoma formation is of order 10 times faster than haemostasis. However, haemostasis should certainly be considered in the following stages of model development due to localized vasoconstriction occurring before haemostasis starts (Armstrong and Golan, 2011). Localized vasoconstriction caused by haemostasis could be another source of the compression of vessels since only capillary compression due to increasing ICP is considered.

By transforming earlier 2D model to a 3D model in this study, the HT damage to the surrounding tissue and healthy vessels can now be estimated. It can be seen that the geometry of the 3D network is highly complex and that it would not be straightforward to derive an equivalence between this model and the earlier 2D model, although it is noted that with adequate and detailed clinical data, the 2D model could allow clinicians to model the consequences of HT. Meanwhile, in future research, this HT model will be

applied in a full-brain 3D model in order to validate with clinical imaging data, since although the CT image is 2D, clinicians calculate the haematoma volume by overlapping the slices of CT images to create a 3D brain map.

Regarding the identifiability aspects of the model, nearly all the parameters used here are likely to vary from one patient to another (to a greater or lesser degree). However, vascular permeability is suspected to be the most likely to vary most significantly from one patient to another and, based on results from this study, this means that this parameter would seem to be the most readily identifiable. However, this remains to be confirmed in future work. It should be noted that the values of CBV and perfusion given here do not match directly to a specific dataset.

The aim of this work is thus to identify those patients who are most at risk of haemorrhage based on imaging data (and other non-imaging parameters). In the previous study, Wang and Payne (2021) proposed a mathematical model to simulate HT and extended this model to a penetrating network in this study. They have investigated how the different geometry and haemodynamics affect the consequences of haemorrhage. By using cerebral angiography, clinicians are able to predict the locations of potential vulnerable vessels and severity of HT, in order to assist them in selecting which patients who are not suitable for rt-PA treatment.

It will be thus necessary to extend this model to an enlarged vasculature length scale and to apply it in other regions in the brain. This model cannot replicate the extent of spatial length scales in the whole brain, particularly when taking into account that a normal brain volume ranges from 1173 to 1626 mL (Filipek et al., 1994). The penetrating

network incorporated within this model, having a volume of merely 10 mm^3, falls significantly short of emulating the complexity and expansive nature of the whole brain. In addition, in the next stage of the model development, more leaky random vessels should be introduced. van Kranendonk et al. (2020) measured median haemorrhage volume to be $3.37\,ml$ based on imaging data, which is in the order of magnitude of 10^2 times larger than one leaky vessel in this study. This higher value of haematoma volume is to be expected, due to multiple vessels likely being leaky in HT. Thus, in real scenarios, a first estimate would be that approximately 100 vessels exhibit leakage, which is a relatively large number. Thus, it will be necessary to simulate multiple permeable vessels in the vasculature and to investigate the interaction of these vessels with the surrounding vessels. This will be the subject of a future study. Meanwhile, by using a full brain model, clinicians can stratify vulnerable patients more accurately using CT imaging data. The risk and consequences of HT caused by the different locations of stroke can thus be identified.

4.5 Conclusion

Through the development of a mathematical model to simulate the HT within a multi-scale microvasculature network, it is possible to simulate the severity of HT and haemodynamics after HT onset. This study has identified that the haematoma radius is approximately proportional to the diameter of the vessel. This model indicates that larger vessel breakdown leads to larger haematoma radius, higher tissue displacement and higher ICP. These results may be able to explain the different categories of HT that have been found clinically. One of the more significant highlights is that this model is able to be compared based on the reductions in both cerebral blood volume and perfusion. A reduction in CBV in the range of $20-25\%$ and in perfusion of approximately $13-17\%$ after HT onset are determined. The solutions and insights gained from this study may be of assistance in future to assess the impact of the HT on an enlarged 3D tissue region and at a whole-brain scale.

4.6 Evaluating the Model: Advantages and Limitations

The question about whether the three main goals of this whole study (from a modelling perspective, a physiology perspective, and a clinical perspective) have been answered is discussed in the following table. A summary of highlights and assumptions for this study is listed in Table 1.1.

Table 4.3. Model accomplishments and limitations

Model:	Penetrating network model
Objectives:	Modelling objective
Completed aspects:	• Governing mathematical equations to describe HT in a penetrating network has been developed. This model works as the second step for the whole study. • The interaction of the tissue pressure distribution between neighbouring blood vessels has been considered. • Key clinical indicators, for example, cerebral blood volume, are able to be acquired and comparable with clinical data.
Unfinished aspects and limitations:	• This model hasn't been extended to a whole brain model, which indicates it still is limited to assist the clinicians to assess and predict HT. • The validation with clinical imaging data is missing.
Objectives:	Physiology objective
Completed aspects:	• Breakdown of BBB in a HT model in a penetrating network has been described by a mathematical model. • Tissue mechanics are considered into the model.
Unfinished aspects and limitations:	• The BBB breakdown is assumed to be a uniform process,

	with an evenly distributed leakage. • The tissue is assumed to be a homogeneous material. Tissue pressure is assumed as a constant value. • For the incorporation of this model into an extended vasculature model or whole brain model, it's important to acknowledge that some specific input parameters exhibit variation from one blood vessel to another. These parameters can include aspects such as vessel geometries, the blood flow rate, the inlet blood pressure, the surrounding tissue pressure, etc. • One of the most important parameters, the definition of haematoma surface pressure is challenged to be validated by using this network.
Objectives:	Clinical objective
Unfinished aspects and limitations:	• The current model is limited to be assist clinicians to predict HT after stroke yet, unless the model is presented in a whole brain model in future.

4.7 Appendix

Appendix 4.A Animal model

Within this model, numerous crucial parameters are derived from experimental data acquired from animal models. Consequently, it becomes imperative to deliberate on the

disparities between the parameters applicable to humans and animals, in order to ensure the validity and applicability of our results.

In the context of this model, several pivotal parameters are derived from canine studies. These include the wall elastic modulus (E), the vascular wall thickness at the point of maximum compliance (h_b¿, and the degree of curvature of the pressure-area relationship (n). Procuring these parameters from human experiments presents considerable challenges.

Given these challenges, direct comparison of each parameter between canines and humans is complex and arduous. Therefore, a more efficient approach might be to evaluate the final impact of capillary compression, which can be seen as a cumulative result of these parameters. Taking into account that canine blood pressure, as measured by Weiser et al. (1977), typically ranges from 130-180 mmHg and is higher on average than that of humans, the influence on capillary compression due to pressure change may be less significant in canines than in humans.

Hence, considering that the blood pressure has the ability to impede bleeding, the eventual haematoma size, if inferred based on canine data, may exceed what would be expected utilizing human data.

Appendix 4.B Algorithm and convergence

The computational expenditure associated with this research is approximately 60 minutes per penetrating network model (NVIDIA Geforce 3070 Ti & Parallel tool [MATLAB R2022a])

The principal coding utilized in this study closely mirrors that of Chapter 3 (a pseudo-algorithm is introduced in Appendix 3.D), with the penetrating network coding obtained from El-Bouri and Payne (2018).

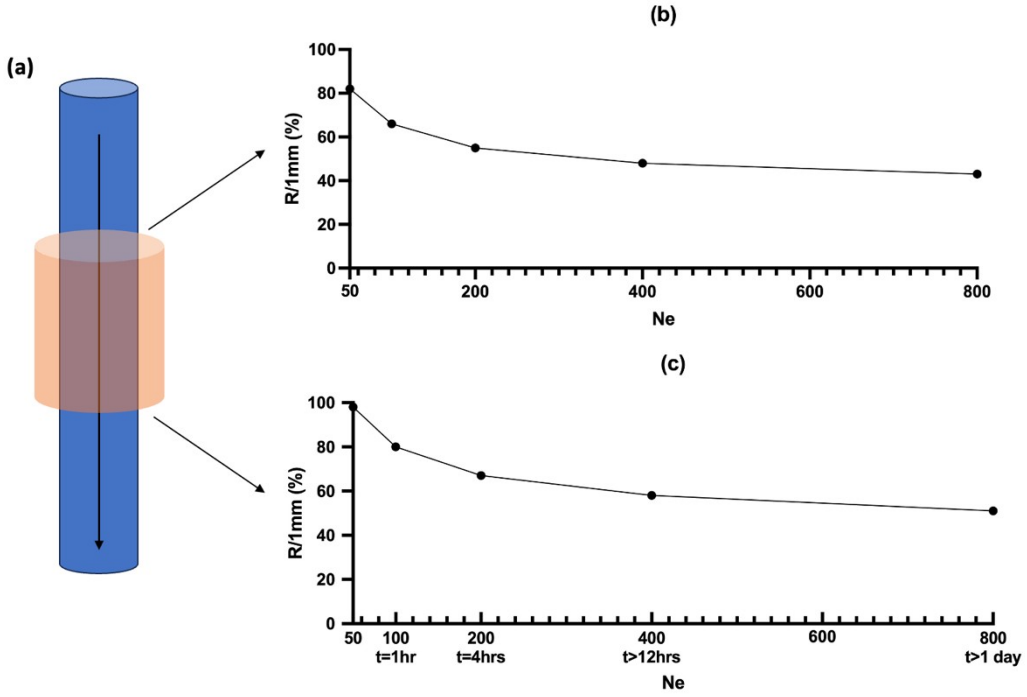


Figure 4.8 Convergence test. R: Haematoma radius; 1mm: penetrating network cuboid width; Ne: number of elements; t: computational time. (a): Schematic of permeable vessel model (only the mid third of the vessel is permeable). (b) describes the relationship between the haematoma radius/cube and the grid size at the entry point of the permeable vessel. Similarly, (c) demonstrates the correlation between the haematoma radius/cube and the grid size at the exit point of the permeable vessel.

Figure 4.8 illustrates the convergence test conducted in this study. The choice of $Ne=100$ is made to obtain a balance between calculation precision and computational

time. The error introduced by the mesh size can be minimized by leveraging more powerful computational resources.

Appendix 4.C Sensitivity analysis

Figure 4.9 presents the sensitivity analysis conducted in this study. It reveals that the three primary parameters influencing the hematoma outcome are the transcapillary filtration rate, the inlet capillary pressure in the permeable vessel, and the vessel length (Other significant parameters such as vessel diameter and vessel wall thickness are discussed in Section 3.3 of Chapter 3). Specifically, a 50% increase in the transcapillary filtration rate (from 1.2 mL/100g tissue/min to 1.8 mL/100g tissue/min) results in a 19% increase in hematoma volume an escalation of 80% in inlet capillary pressure results in a 44.5% growth in hematoma volume; When vessel length is amplified by 700%, there is an 840% escalation in the volume of the hematoma.

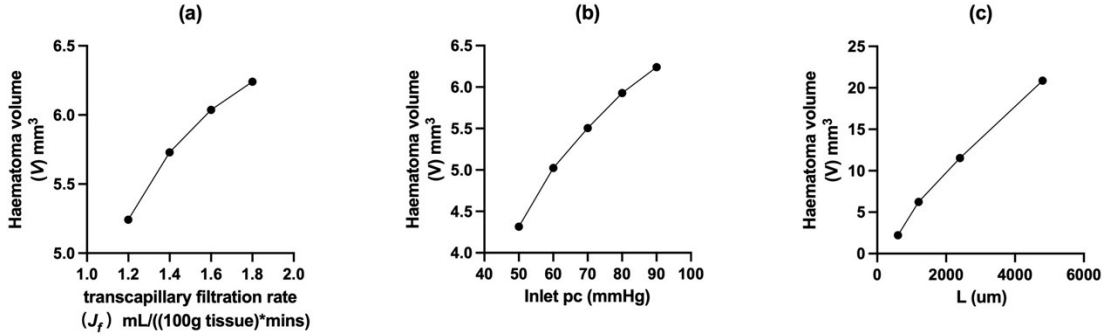


Figure 4.9 Variations in haematoma volume as functions of (a) transcapillary filtration rate, (b) inlet capillary pressure in the permeable vessel, and (c) vessel length.

Drawing upon the results of the sensitivity analysis and preceding research, the author proposes that the transcapillary filtration rate, J_f, emerges as the most crucial

parameter for verification in future experiments. This recommendation aims at advancing the development of the HT model.

Chapter 5: Mathematical modelling of haemorrhagic transformation in the human brain

The work presented in this chapter is expected to be submitted in November 2022 as: X. Chen*, J. Wang*, K. R. van Kranendonk, T. I. Józsa, W. K. El-Bouri, M. Kappelhof, M. van der Sluijs, Y. B.W.M. Roos, A. van der Lugt, H. A. Marquering, C. B. L. Majoie, S. J. Payne, "Mathematical modelling of haemorrhagic transformation in the human brain", Applied Mathematical Modelling, 2022.

Contributor Roles Taxonomy:

Jiayu Wang: Methodology, Validation, Writing - Original Draft (Section 5.0-5.1, 5.2.4-5.5), Visualization, Conceptualization.

Xi Chen: Methodology, Writing - Original Draft (Section 5.2.1-5.2.3), Software, Data Curation.

Dr. Katinka R. van Kranendonk: Investigation, Writing - Review & Editing.

Dr. Tamas. I. Józsa and Dr. Wahbi El-Bouri: Software, Writing - Review & Editing.

Prof. Charles B. L. M. Majoie: Supervision, Writing - Review & Editing.

Prof. Stephen J Payne: Supervision, Writing - Review & Editing.

Other authors: Investigation, Writing - Review & Editing, Data Curation.

* These authors contributed equally.

Corresponding author: Jiayu Wang

In this chapter, the perfusion model, part of leakage model and code programming were developed by Xi Chen under the supervision of Professor Stephen J. Payne, and these are not part of this thesis. The analysis of CT images and the remaining leakage model are, however, part of this thesis. The works conducted by Xi Chen will be clearly stated in the footnote.

5.0 Abstract

Objective. Haemorrhagic transformation (HT) is one of the most common complications after ischaemic stroke. HT can be the result of stroke progression or a complication of reperfusion treatment for stroke. The aim of this study is to apply a previously proposed HT mathematical model within a computational whole brain model to determine the

factors that affect the severity of HT at this scale. In addition, these simulations are directly compared with neuroimaging data.

Approach. The MR CLEAN-NO IV trial assessed the effect of endovascular therapy (EVT) alone compared with intravenous alteplase treatment (IVT) followed by EVT for patients with acute ischaemic stroke due to large vessel occlusion. Of the 15 HT patients chosen for this study from the MR CLEAN-NO IV trial, 5 are haemorrhagic infarction type 1, 5 are haemorrhagic infarction type 2 and 5 are parenchymal haematoma type 1. The comparison is carried out by comparing the haematoma locations and haematoma volume between the simulations and the clinical images. The parameters of the model are then optimised. Finally, the model is used to investigate the factors that affect the severity of HT.

Main results. Based on the computational whole brain model, the perfusion was found to be reduced by 5-16% after HT onset. The results are in good agreement with the clinical data. This study also shows that 1% increase of blood viscosity reduces perfusion by 0.0434% and increases haematoma volume by 10.35% from baseline, and 1% increase of blood pressure reduces perfusion by 0.80% and increases haematoma volume by 4.73% from baseline. These results indicate that increased blood glucose and hypertension both lead to a higher severity of HT.

Significance. This model, by bridging the gap between the mathematical HT model and clinical imaging data, provides the first whole brain prediction model for HT assessment.

Connections with Prior Research. This model advances prior HT research by transitioning from a 3D microvasculature network to a comprehensive 3D computational brain

model. It's important to note that in this model, subregions in the brain model are assumed to be the source of blood leakage. The concept of leakage originating from a broken blood vessel is not utilized. This development enables the author to identify crucial parameters, such as the definition of hematoma surface pressure, and corroborate these with available clinical indicators.

5.1 Introduction

Stroke is one of the most important causes of damage to the brain and was ranked as the second leading cause of death across the world in 2018 (Katan and Luft, 2018). The incidence of stroke is predicted to continue to increase in ageing populations. Haemorrhagic transformation (HT) is one of the most common complications after ischaemic stroke, caused by damage to the blood–brain barrier (BBB) that can be the result of stroke progression or a complication of stroke treatment with reperfusion therapy. HT is a frequent, often asymptomatic, complication (Álvarez-Sabín et al., 2013) that has the potential to lead to long-term morbidity and mortality (Marsh et al., 2013). The Heidelberg Bleeding classification which incorporates the European Cooperative Acute Stroke Study (ECASS) classification, classifies HT based on its radiological appearance on follow-up computed tomography (CT) or magnetic resonance imaging (MRI) (von Kummer et al., 2015): haemorrhagic infarction type 1 (HI1), which is defined as small petechiae along the peripheral margins of infarct; haemorrhagic infarction type 2 (HI2) as confluent petechiae within the infarcted area but without mass effect;

parenchymal haematoma type 1 (PH1), defined as blood clots in ≤ 30% of the infarcted area with some slight mass effect; and parenchymal haematoma type 2 (PH2) as blood clots in > 30% of the infarcted area with substantial mass effect. HT can also be quantified by measuring its volume and large volumes were associated with poor functional outcomes (van Kranendonk et al., 2020). HT is often located in the internal regions of the brain: putaminal (occurrence: 46.2%), thalamic (occurrence: 19.4%) and pontine (occurrence: 14%) (Nah et al., 2012).

The severity of HT is highly variable and a key question is whether the occurrence and severity of HT can be predicted accurately after ischaemic stroke, based on available imaging data and clinical parameters. Wang and Payne (2021) first proposed a mathematical model that describes the behaviour of HT within a 2D vasculature model. In this vasculature model, the geometries of vessels in the same generation were the same. However, based on anatomical studies, capillaries have been shown to have a more web-like than tree-like structure (Duvernoy et al., 1981). In addition, the effects of HT on surrounding normal vessels and tissue were not considered in this initial model.

Wang et al. (2022b) extended the previous model to an enlarged vasculature length scale in order to compare the model predictions more accurately with the human vasculature. The penetrating model they used was that of El-Bouri and Payne (2018) and they investigated the effects of HT on the surrounding tissue and vessels. It was found that perfusion reduces by approximately $13-17\%$ and cerebral blood volume (CBV) reduces by around $20-25\%$ after HT onset due to the effect of capillary compression

caused by increased interstitial pressure. However, this model focuses on a length scale of around $1\,mm$, which remains difficult to compare with imaging data.

Therefore, it is necessary to extend the HT model to a full brain length scale ($100\,mm$) and validate this model with real imaging data, as shown in Figure 5.1. Various full brain models have been developed, for example, to investigate the correlation between stress and midline shift (MLS) (Bing et al., 2020), to study the importance of different constitutive relationships and material properties (Weickenmeier et al., 2017), to explore the risk factors associated with the early stages of Alzheimer's disease (Guo et al., 2018) and to simulate tissue perfusion (Padmos et al., 2021). However, a full brain model that describes HT has not previously been developed.

The aim of this study is thus to develop a model which can simulate the severity of haemorrhage in a full brain model. In addition, this model has the potential to be used to help clinicians to determine the bleeding region more accurately. The HT model developed by Wang and Payne (2021) and Wang et al. (2022b) were used, which was further extended by inclusion of an oedema model developed by Mokhtarudin and Payne (2015).

The developed HT model is applied to provide information in addition to a perfusion model described by Guo et al. (2018), Padmos et al. (2021) and Józsa et al. (2021). Then the results are compared with imaging data from the MR CLEAN-NO IV trial (LeCouffe et al., 2021). Properties such as haematoma volume are estimated and compared with neuroimaging measurements (LeCouffe et al., 2021, Jain et al., 2013). By comparing with the clinical data, the parameters used for these simulations, such as the definition of

haematoma surface pressure, can be optimised. The factors that may affect the severity of HT, including increased blood viscosity and blood pressure are investigated as a conclusion.

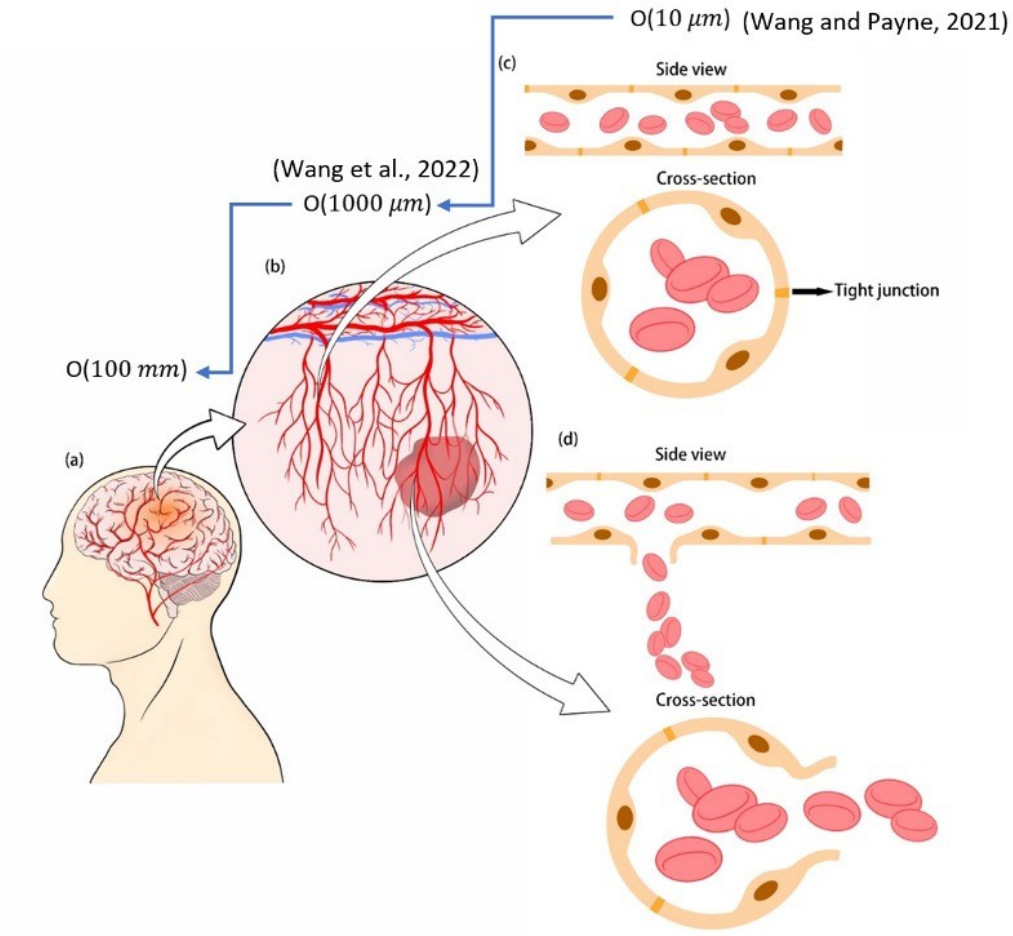


Figure 5.1. Macroscopic (a) and microscopic (b, c, d) configurations of haemorrhagic transformation (HT) simulation across different length: (a) HT model in the entire human brain (present study); (b) simulation of HT in penetrating vessel network (Wang et al., 2022b); (c) healthy vessel; (d) BBB breakdown and haemorrhage modelling around a single vessel (Wang and Payne, 2021). Figure adapted from Wang and Payne (2021).

5.2 Materials and methods

The model consists of two components that simulate blood perfusion and individual haematomas respectively. The models will be introduced individually before being coupled. The methods to provide quantification of HT will then be introduced.

5.2.1 Perfusion Model[1]

5.2.1.1 Governing Equations

In the perfusion model, blood flow in the microcirculation is captured by a three-compartment porous medium (arteriole, capillary, and venule compartments) approach. Darcy's law is used to model the porous medium. The corresponding governing are:

$$\nabla \cdot \left(\frac{K_a}{\mu_b} \nabla p_a\right) ¿ \omega_{ac} \cdot \left(p ¿ ¿ a - p_c\right), ¿ \tag{5.1}$$

$$\nabla \cdot \left(\frac{K_c}{\mu_b} \nabla p_c\right) ¿ - \omega_{ac} \cdot \left(p ¿ ¿ a - p_c\right) + \omega_{cv} \cdot \left(p ¿ ¿ c - p_v\right), ¿ ¿ \tag{5.2}$$

$$\nabla \cdot \left(\frac{K_v}{\mu_b} \nabla p_v\right) ¿ - \omega_{cv} \cdot \left(p ¿ ¿ c - p_v\right), ¿ \tag{5.3}$$

where p_a, p_c and p_v denote the blood pressures in the arteriole, capillary, and venule compartments. K_a, K_c and K_v denotes the permeability tensors for the arteriole, capillary, and venule compartments respectively, whereas ω_{ij} represents the fluid transfer coefficient between compartments i and j, and μ_b denotes dynamic blood viscosity. Note that the transfer coefficients are different in white matter and grey matter and can thus be further defined by ω_{ac}^{w}, ω_{ac}^{g} and ω_{cv}^{w}, ω_{cv}^{g}, respectively (El-Bouri and Payne, 2016, Józsa et al., 2021).

[1] The perfusion model was developed by Xi Chen.

According to the results presented in previous studies (El-Bouri and Payne, 2016, Józsa et al., 2021), the permeability values in the arteriole and venule compartments are described using anisotropic permeability tensors since penetrating vessels are oriented perpendicular to the pial surface. In contrast, the permeability of the inter-connected capillary network is isotropic (Józsa et al., 2021) and thus reduces to a scalar value.

5.2.1.2 Boundary Conditions

In the cerebral blood circulation, blood feeds the brain through penetrating arterioles and flows back into the veins on the pial surface. Previous studies on cerebral blood perfusion show that each arterial vessel is responsible for the perfusion of a subregion on the pial surface (Okell et al., 2013, Mutsaerts et al., 2015). Therefore, the brain pial surface is subdivided into 109 subregions and the subregions in the model can be used in this way to simulate vessel occlusions at different locations. The boundary conditions are then implemented as given in Table 5.1.

Table 5.1: Boundary conditions for the perfusion model.

	Cortical Surface	Ventricle Surface
Arteriole Blood	$p_a = 90\,mmHg$ (Non-occluded regions); $K_a \nabla p_a = 0$ (Occluded regions, which are chosen manually to match the hematoma locations);	$K_a \nabla p_a = 0$
Capillary Blood	$\nabla p_c = 0$	$\nabla p_c = 0$
Venule Blood	$p_v = 15\,mmHg$	$K_v \nabla p_v = 0$

A constant pressure value is given to the non-occluded perfusion regions while no-flow boundary conditions are given on the occluded subregions. The occluded subregions are

chosen to match locations of the hematoma based on the clinical images. Since blood cannot flow through the ventricular surface, zero flux Neumann boundary conditions are imposed on the ventricle surface for all three compartments.

5.2.2 Leakage model

5.2.2.1 Governing Equations

In this model, the blood is assumed to leak into the interstitial space and an additional compartment for the interstitial flow is thus required. Therefore, a porous circulation model with 4 compartments (arteriole, capillary network, venule, and interstitial space) is proposed here to predict the growth of a haematoma and the change in cerebral blood flow (CBF) and perfusion before and after HT. The blood leakage is modelled using the capillary wall filtration model and the flow rate can be written as (Starling, 1896, Mokhtarudin, 2016a):

$$Q_{flux} = \begin{cases} 2\bar{n}_b \dfrac{L_p}{r}(p_c - p_w) \in bleeding\,tissue \\ 0 \in healthy\,tissue \end{cases} \tag{5.4}$$

where $\bar{n}_b$ is the volume fraction of blood vessel in a unit volume of brain tissue, L_p denotes the vascular permeability, r denotes vessel radius, p denotes the hydrostatic pressure with subscripts that represent capillary blood pressure and interstitial fluid pressure respectively and Q_{flux} denotes the leakage flow rate.

Here, the compression of the capillary blood vessels is also considered using the tube law (Drzewiecki et al., 1997, Mokhtarudin, 2016a), and the capillary compression function is assumed to be of the form:

$$f = \frac{1}{2}\left[1 + \tanh\left(1 + \frac{\overline{p} - p_w}{0.01E}\right)\right]¿ \quad (5.5)$$

where f denotes the fraction of vessels remaining open, $\overline{p}$ is the baseline value of interstitial pressure, and $E = 6.5\,mmHg$ is the bulk modulus representing the capillary wall stiffness.

Since the blood flow into the haematoma compresses the tissue, it acts to squeeze the interstitial fluid in the brain. Therefore, the blood flow and the interstitial flow driven by the growing haematoma both need to be considered. There are no current experimental data available to define the surface of a haematoma. Hence, in these simulations, in order to obtain reasonable values of haematoma volume, the threshold of haematoma surface pressure, $p^{¿} = 3.5\,mmHg$ above the baseline tissue pressure. The value is chosen following simulations (results shown below) that show that this value appears to be the optimal one to obtain haematoma volumes that match clinical imaging data reasonably well. The sensitivity analysis for this haematoma surface pressure will, however, be presented and discussed below.

Based on the author's knowledge, there is currently no anatomical data of the bleeding proportion in different types of vessels in HT. In this model, only the capillaries are assumed to be leaky when HT occurs. Gliem et al. (2012) found that bleeding frequently occurred around thin-walled vessel in the infarct border zone and the capillary wall thickness is around $2\,um$ (Payne and Lucas, 2018). In addition, based on morphological measurements of the frequency distribution of vessels diameter, majority of vessels are found to be capillary vessels (Lauwers et al., 2008). Furthermore, Wang et al. (2022b)

[1] Eqs(5.6-5.10) were developed by Xi Chen

found that the larger leaky vessel led to larger haematoma volume and in this simulation, the PH2 type of HT is excluded. Therefore, in terms of to determine the bleeding regions in different compartments (arteries, capillaries and veins), the leakage is only assumed to occur in the capillary compartment.

The governing equations for the leakage model can be written as the following:

$$\nabla \cdot (\frac{K}{\mu} \nabla p_w) = -f \cdot Q_{flux} \quad (5.6)$$

$$\nabla \cdot (\frac{K_a}{\mu_b} \nabla p_a) = f \cdot \omega_{ac} \cdot (p¿¿a - p_c)¿ \quad (5.7)$$

$$\nabla \cdot (\frac{K_c}{\mu_b} \nabla p_c) = -f \cdot \omega_{ac} \cdot (p¿¿a - p_c) + f \cdot \omega_{cv} \cdot (p¿¿c - p_v) + f \cdot Q_{flux} ¿¿ \quad (5.8)$$

$$\nabla \cdot (\frac{K_v}{\mu_b} \nabla p_v) = -f \cdot \omega_{cv} \cdot (p¿¿c - p_v)¿ \quad (5.9)$$

where μ denotes fluid viscosity in the interstitial space.

The permeability of fluid in the interstitial space depends on whether the space is occupied by blood or interstitial fluid. Since the fluid component is assumed to be determined by a pressure threshold $p^{¿} = 3.5\, mmHg$, the tissue permeability of fluid in the interstitial space depends on pressure values and it is thus assumed to be of the form:

$$\frac{K}{\mu} = \frac{K_w}{\mu} + \frac{1}{2}(\frac{K_b}{\mu} - \frac{K_w}{\mu}) \cdot ¿ \quad (5.10)$$

where K_w and K_b denote the conductivities of water and blood in the interstitial space, respectively.

[1] Eqs(5.6-5.10) were developed by Xi Chen

5.2.2.2 Boundary Conditions

In the haematoma model, following removal of the occlusion, the blood perfusion is assumed to be fully restored. Although this is a strong assumption imposed for simplicity, it will be possible in future to examine the effect of incomplete restoration. The perfusion then leads to an increased blood pressure on the blood vessel wall and causes vessel rupture and the formation of a haematoma. Constant pressure boundary conditions are imposed on the pial surface for all subregions. The interstitial space boundaries are the interface between interstitial fluid and cerebrospinal fluid and the pressure is assumed to be constant due to the high compliance of the cerebrospinal fluid (CSF) (Mokhtarudin and Payne, 2017). The boundary conditions for the haematoma model are given in Table 5.2.

Table 5.2: Boundary conditions for the haematoma model.

	Cortical Surface	**Ventricle Surface**
Arteriole Blood	$p_a = 90\,mmHg$	$K_a \nabla p_a = 0$
Capillary Blood	$\nabla p_c = 0$	$\nabla p_c = 0$
Venule Blood	$p_v = 15\,mmHg$	$K_v \nabla p_v = 0$
Interstitial Fluid	$p_w = 10\,mmHg$	$p_w = 10\,mmHg$

5.2.3 Model Coupling[1]

In the perfusion model, it is assumed that the locations with higher values of capillary blood pressure are prone to vessel disruption, BBB breakdown, and consequently HT. Since haematoma is likely only to occur in the infarcted region, a 70% perfusion

[1] Model Coupling was conducted by Xi Chen

reduction is used as the primary threshold for the tissue bleeding (Campbell et al., 2015, Jovin et al., 2017, Payne, 2016). Furthermore, although subcortical HT has been found to appear more frequently than cortical HT, it should be noted that the prediction of the precise spatial location of the haematoma is highly challenging. To obtain the haematoma locations that match the clinical images, capillary pressure ranges were varied and used as the secondary threshold for vessel rupture and tissue bleeding. The geometry of the bleeding tissue obtained from the perfusion model was then included within the leakage model to simulate the growth of the haematoma and the resulting perfusion reduction.

1. The heathy perfusion is simulated to obtain the healthy blood flow (Figure 5.2a).
2. The occluded subregions are chosen (Figure 5.2b) to obtain the stroke blood perfusion (Figure 5.2c).
3. Patient-specific capillary pressure ranges are chosen manually. Regions with 70% perfusion reduction (Figure 5.2d) and over where the capillary blood pressure lie in the ranges are defined as bleeding tissue for each patient.
4. The regions chosen as bleeding tissue are imported into the leakage model for haematoma simulation (Figure 5.2e).
5. The haematomas are defined as regions with interstitial pressure rise over 3.5 mmHg. Comparison in the pairs of haematoma centre locations (x_i, y_i, z_i) and volumes, which are obtained from the computational model and clinical images is performed Figure 5.2f). If the differences do not lie in a reasonable range (the differences in pairs of x values, y values and z values from the computational model and imaging data are < 5%), then go back to step 2 until a reasonable hematoma is obtained.

[1] Model Coupling was conducted by Xi Chen

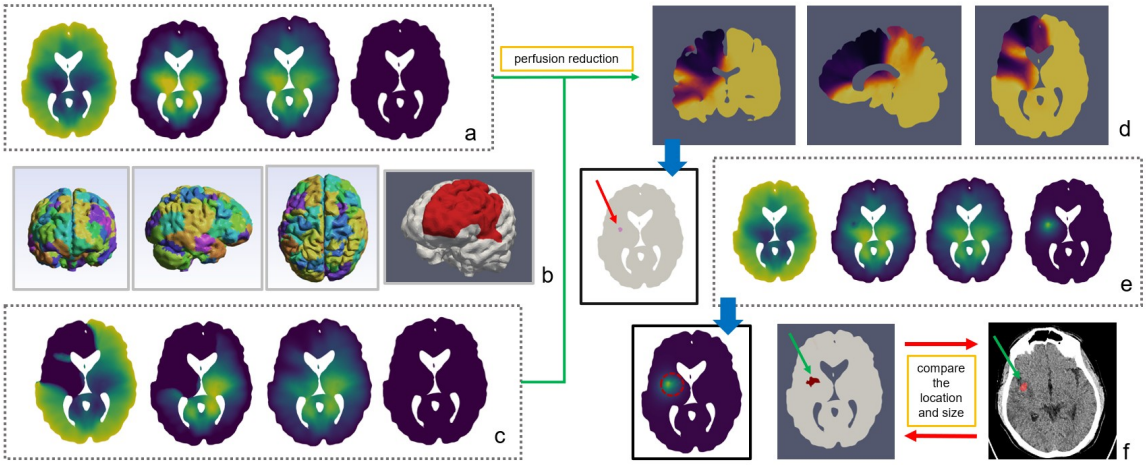


Figure 5.2 (a) Simulation of blood pressures in healthy blood flow in the arteriole, capillary, venule and interstitial space, respectively. (b) Subregions on the cortical surface and selection of the occluded regions (red). (c) Simulation of brain blood pressures in infarction. A reduction in blood pressures in the occluded region is shown as the colour darkens. (d) Blood perfusion reduction obtained from the healthy and stroke cases. (e) Bleeding tissue is assumed to occur in the regions where perfusion reduction is over 70% and is chosen by varying the capillary blood pressure ranges. The bleeding tissue is then imported into the leakage model for the simulation of the growth of hematoma. (f) 3.5 mmHg of pressure rise is used as the threshold of hematoma boundary and the hematoma is compared with the CT images.

All the parameters used in the models and their sources are given in full in Table 5.3.

[1] Model Coupling was conducted by Xi Chen

Table 5.3: Values of model parameters used in the perfusion, oedema and osmotherapy models and their sources.

Parameter	Value	Reference(s)
K_a	$4.4424 \times 10^{-12} m^2$	Estimated by 0-order arteriole diameters and vessel density (Józsa et al., 2021)
K_c	$1.5408 \times 10^{-14} m^2$	$1.0 \times 10^{-15} m^2$ (El-Bouri and Payne, 2016); $1.0 \times 10^{-10} m^2$ (Tully and Ventikos, 2011)
K_v	$8.8848 \times 10^{-12} m^2$	Estimated by pressure and blood perfusion rate (Józsa et al., 2021)
K_w	$3.6 \times 10^{-15} m^2$	(Su, 2012)
K_b	$1.0 \times 10^{-15} m^2$	(Su, 2012)
ω_{ac}^{w}	$1.326 \times 10^{-6} Pa^{-1} \cdot s^{-1}$	Derived from perfusion rates in grey and white matter (Lüders et al., 2002, Józsa et al., 2021)
ω_{ac}^{g}	$5.22 \times 10^{-7} Pa^{-1} \cdot s^{-1}$	
ω_{cv}^{w}	$4.641 \times 10^{-7} Pa^{-1} \cdot s^{-1}$	
ω_{cv}^{g}	$1.828 \times 10^{-6} Pa^{-1} \cdot s^{-1}$	
p_a at cortical surface	$12000\, Pa = 90\, mmHg$	(Józsa et al., 2021)
$\overline{p}$	$10\, mmHg$	(Payne, 2006)
p_v at cortical surface	$2000\, Pa = 15\, mmHg$	(Józsa et al., 2021)
L_p	$3.0 \times 10^{-11} m \cdot Pa^{-1} \cdot s^{-1}$	(Su, 2012)
R_c	$5.0 \times 10^{-6} m$	(Cassot et al., 2006)
$\overline{n}_b$	0.03	(Ito et al., 2001)
μ_b	$3.6 \times 10^{-3} Pa \cdot s$	(Su, 2012)
μ	$1.0 \times 10^{-3} Pa \cdot s$	(Mokhtarudin and Payne, 2015)

In the model, the governing equations are solved numerically using Python with a high-performance open-source Finite Element library, FEniCS (Logg and Wells, 2010, Logg et al., 2012). The highly coupled equations in the Finite Element model are solved in a mixed function space describing the multi-compartment dynamic system. The pressure in each compartment (p_i) is discretised with piecewise linear Lagrange (P1) elements. Meanwhile, the permeabilities (K_i) and the other coefficients (ω_{ij}, L_p, etc) used in the model are represented in piecewise constant (dP0) tensor and scalar function spaces, respectively. The flow fields and the blood perfusion are computed in dP0 elements and

are solved using the BiCojungate Gradient STABilised method (BiCGSTAB) with an Algebraic MultiGrid (AMG) preconditioner. The time steps are discretized using a backward Euler scheme throughout the model.

5.2.4 Quantifications of CT images

Patients with HT were included in this study from the MR CLEAN-NO IV trial (LeCouffe et al., 2021). The MR CLEAN-NO IV trial was a multicentre randomized controlled trial that assessed the effect of EVT alone compared with IVT before EVT after acute ischaemic stroke due to large vessel occlusion. The study protocol of MR CLEAN-NO IV has previously been described by Treurniet et al. (2021). HT was assessed on follow-up CT according to the Heidelberg bleeding classification acquired within 7 days after stroke onset (LeCouffe et al., 2021, Treurniet et al., 2021). 5 patients with HI1, 5 with HI2 and 5 with PH1 were included. Patients with PH2 were excluded because there were significant tissue displacements and large midline shifts (MLS) which are more difficult to simulate (and may require a non-linear constitutive model for the tissue). All 15 series of CT images were quantified by manually delineating the haemorrhage by a trained observer (KRK) using ITK-SNAP (version 3.4.0).

All CT images were imported into MATLAB R2022a to generate a pixel (2D) matrix, which was used to determine the centre of each haematoma. A coordinate was established to describe hematoma centres, as shown in Figs. 5.3 and 5.4. The origin is set at the lower left of the cerebellum (left of bottom oblongata) for all patients and computational brain models. It was found to be challenging to determine the centre of the brain when there

is a significant effect of MLS shown in the imaging data. Thus, setting the origin outside the brain based on the boundary of brain became the preferred choice. The centre of haematoma in the brain can thus be described in a three-dimensional co-ordinate of the form (x, y, z) where x, y and z lie in the range of $0-100\%$.

The determination of the haematoma location is based on the delineation of the haemorrhage. The haematoma could then be quantified in the pixel matrix. The pixels of the haematoma shown in the pixel matrix can be described as (x_i, y_i, z_i). Then all the locations of haematoma pixels in three directions were used to obtain the centre of each haematoma. The flow diagram of the quantification of HT method is shown in Figure 5.3.

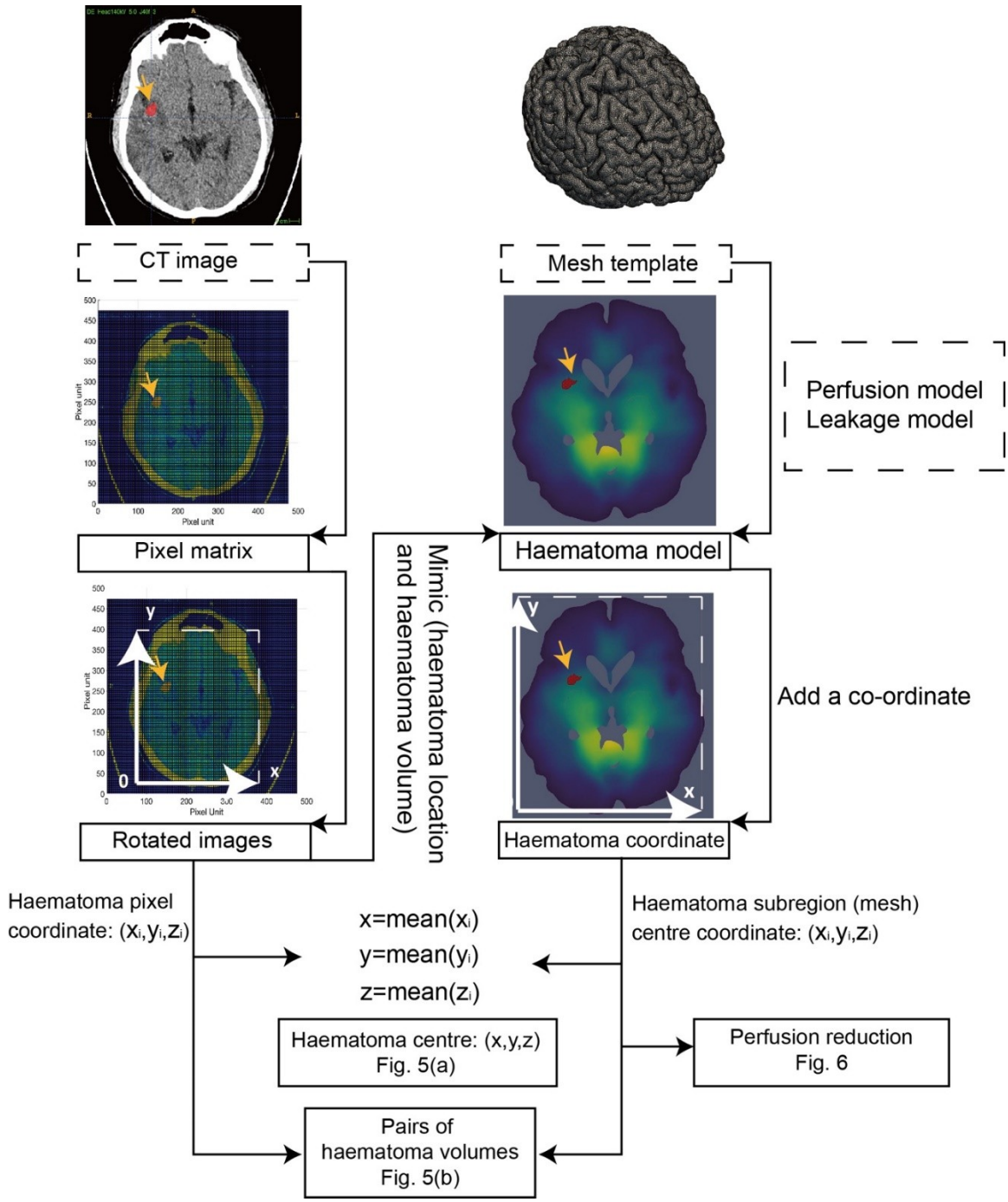


Figure 5.3. Schematic drawing of quantification method of HT for both CT images and the computational brain model. Dashed boxes: input. Yellow arrows: haematoma locations. The image was rotated after being imported into MATLAB using the function "imrotate" in MATLAB to ensure the same size (dimensions) of matrix.

5.3 Results

5.3.1 Haematoma location and volume measurements

Using Eq. (5.4) -(5.10), the haematoma models can be computed for each patient with different sizes and locations of HT. An example of a HT simulation is given in Figure 5.4 for a type HI2 haematoma. The haematoma volume from CT images was calculated to be $0.72\,ml$ and the result obtained from the simulation shows that the haematoma volume is close at $0.64\,ml$. The centre of haematoma obtained from the CT images is located at $(25.82\%, 60.60\%, 48.72\%)$ and that calculated from the simulation is located at (29.48%, 61.65%, 47.17%¿. As discussed above, the co-ordinates of each haematoma centre are given in percentage length (i.e., a dimensionless length) to mitigate the effects of brain geometry that may vary from one patient to another. Figure 5.5 shows the correlation of haematoma and bleeding region (note that the example shown in this figure is not the same as the example in Figure 5.4). It can be seen that the bleeding region (white) is located completely inside the haematoma (red).

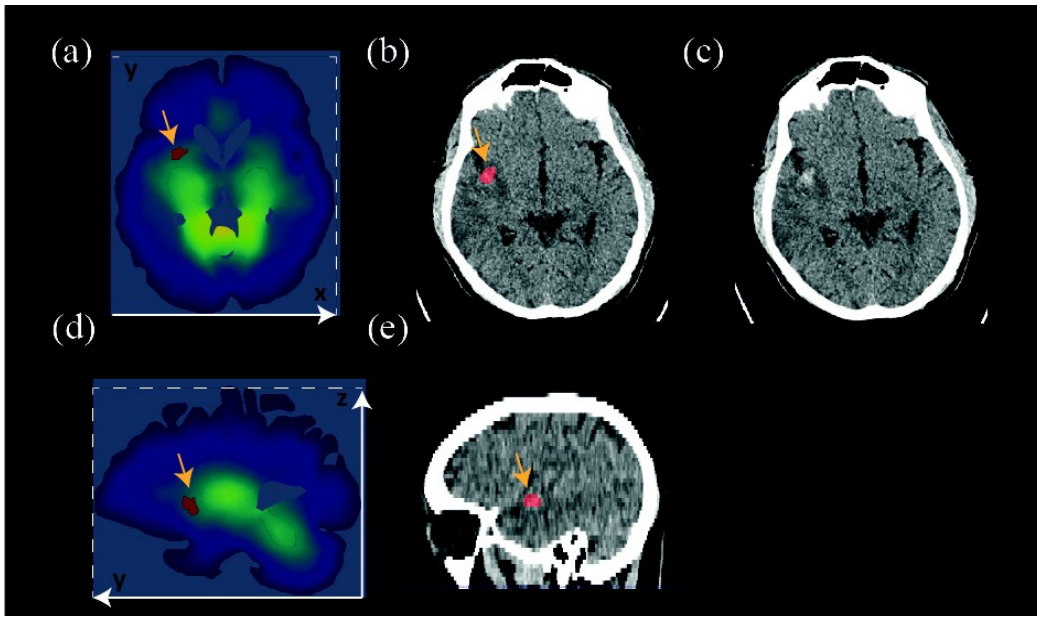


Figure 5.4. Example HT model showing a haematoma located in a full brain model obtained from the axial plane (a) and sagittal plane (d). This example is compared with an example of HT by showing the axial plane (b) and sagittal plane (e). The positive x-axis extends to the right, reaching the far-right side of the brain; the positive y-axis extends to the front, reaching the front side of the brain; and the positive z-axis extends to the top of the brain. The CT image without annotation (c).

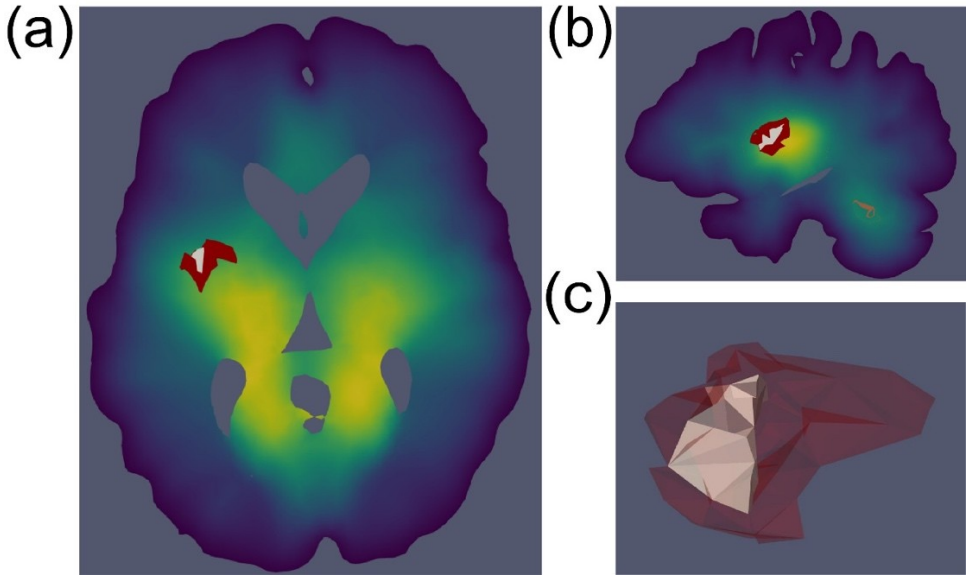


Figure 5.5: Example of haematoma and bleeding region. A haematoma (red substance) including bleeding region (white substance) from the axial plane (a). Slice view of the haematoma and bleeding region obtained from the

simulation (b). The haematoma and bleeding region are shown overlaid in (c). The bleeding region is fully inside the haematoma.

These 15 HT imaging data were chosen because of their high image quality. As shown in Figure 5.6(a), 5 patients had HT in the left hemisphere (x value < 50%) and 10 patients had HT in the right hemisphere. The haematoma centres obtained from the image data and simulations are all close to each other (no significantly statistical differences are found using a t-test).

The co-ordinate differences from simulations and CT images occur because our model is limited in its location of the haematoma since the subregion size was pre-determined, i.e., the finite resolutions of both the CT images and the computational brain model lead to small differences in the haematoma centres (Józsa et al., 2021). Comparisons of haematoma volumes (V) are also shown in Figure 5.6(b) and the p-value for the pair of volumes is ¿0.05, indicating that there is again no statistically significant difference between the predicted and measured haematoma volumes.

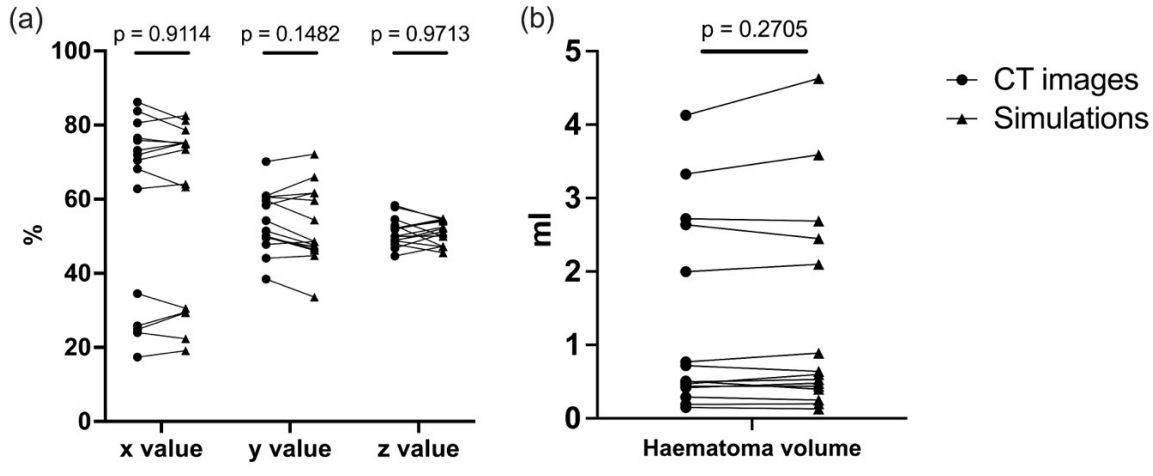


Figure 5.6. Comparison of HT between CT images and simulations. Quantification of haematoma centres in x, y and z axis (a). Comparison of haematoma volume between image data and simulations (b).

5.3.2 Perfusion deficit quantification

Figure 5.7 shows the comparison of perfusion reduction in the region of interest. In these simulations, the perfusion is found to be reduced by $5\%-16\%$ after HT onset. The perfusion reduction (ΔF) (from the full brain model) is computed from data collected on the ipsilateral side compared with the contralateral (healthy) side. The right part of Figure 6 shows the perfusion reduction values computed in a penetrating network model, the values of which are taken from Wang et al. (2022b).

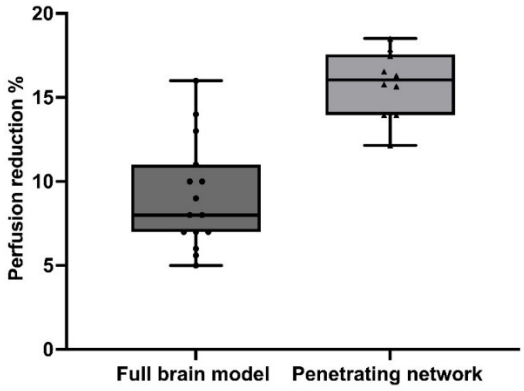


Figure 5. 7. Comparison of perfusion reduction obtained from this full brain model and penetrating network model. The data for right boxplot are reproduced from Wang et al. (2022b).

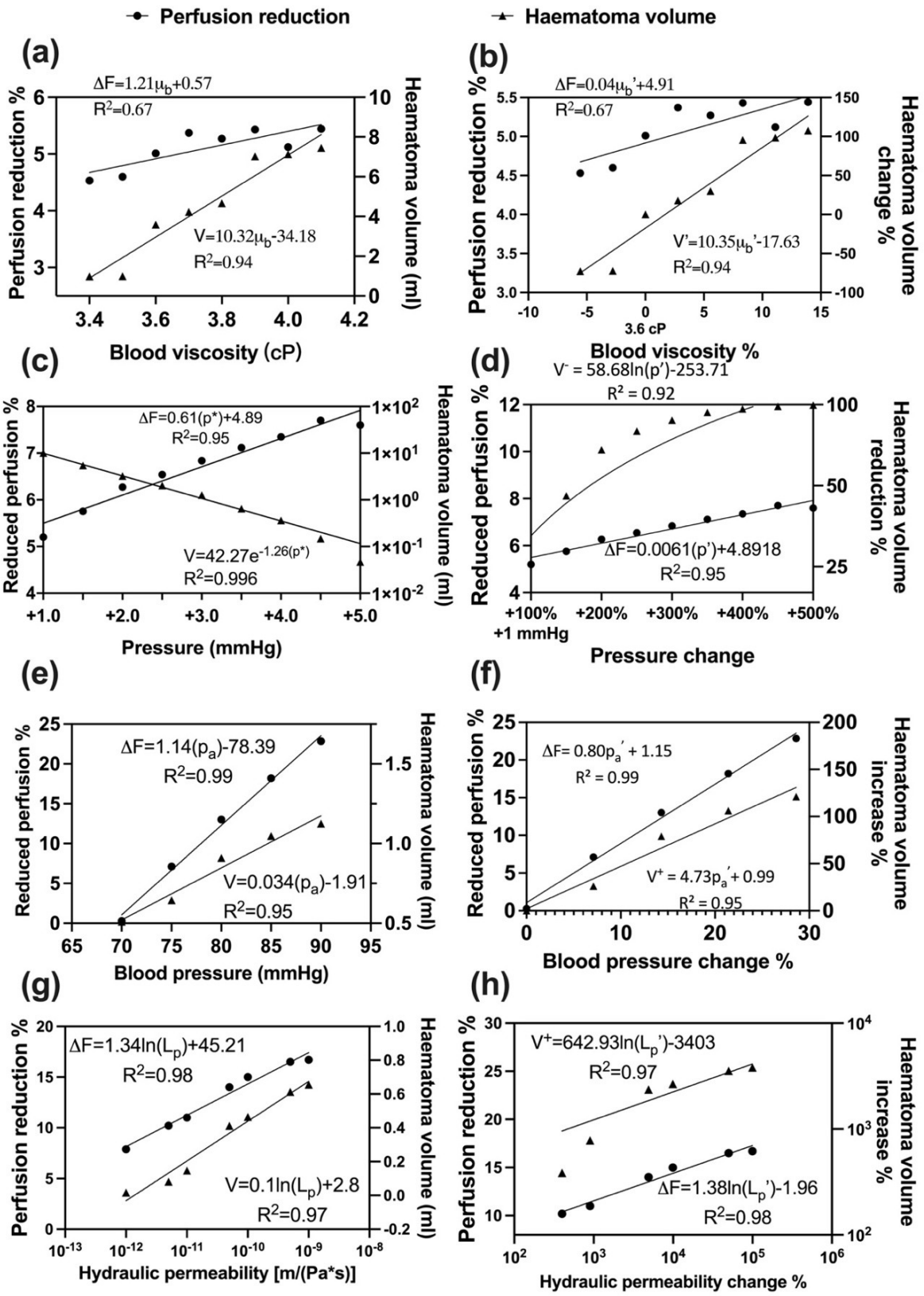
5.3.3 Sensitivity analysis

Next, one example of HT was used to process the sensitivity analysis with various values of blood viscosity μ_b, the definition of haematoma surface pressure $p^{¿}$ and blood pressure p_a. This example of HT was set close to the lenticular nucleus, which is found to be a high occurrence location of HT (Horie et al., 2019). Correlations between haematoma volumes (V ¿and perfusion reduction (ΔF) with μ_b, $p^{¿}$ and p_a were tested, as shown in Figure 5.8. A critical phenomenon that was found when the blood viscosity

was adjusted is that the haematoma volume increases with increased blood viscosity when the blood viscosity is in the range of $3.4-4.1\,cP$. It is found that 1% increase of blood viscosity increases 10.35% of haematoma volume from the baseline (when $\mu_b=3.6\,cP$), as shown in Figure 5.8(b). In addition, the perfusion is found to reduce when the blood viscosity increases: 1% increase of blood viscosity reduces 0.0434% of perfusion, Figure 5.8(b).

As shown in Figure 5.8(c), a higher definition of haematoma surface pressure leads to a larger haematoma volume and smaller perfusion reduction, as would be expected (note the logarithmic scale, which indicates the very high sensitivity). The haematoma volume changes significantly with the definition of haematoma surface pressure $p^{¿}$. Haematoma volume is calculated to be $10.02\,ml$ when $p^{¿}$ is set as the initial value at $1\,mmHg$. When the value of $p^{¿}$is set at $5\,mmHg$, the haematoma volume is equal to $0.05\,ml$. When the value of $p^{¿}$ is thus set to be just 5 times larger than its original value, the haematoma volume will decrease by some four orders of magnitude. As shown in Figure 5.8(d), 1% change of $p^{¿}$ ($\pm p^{'}$) leads to 0.0061% change of perfusion.

Higher blood pressure, as expected, results in larger perfusion reduction and haematoma volume. As shown in Figure 5.8(e), when the blood pressure p_a is set from $70\,mmHg$ to $90\,mmHg$, the haematoma volume grows from $0.51\,ml$ to $1.12\,ml$ and perfusion reduction increases from 0.28% to 22.85%. The measure of importance is shown in Figure 5.8(f): 1% increase of blood pressure reduces 0.80% of perfusion and increases $4.73\%$of haematoma volume from the baseline.


Perfusion reduction
Haematoma volume
(a)
ΔF=1.21μb+0.57
R2=0.67
V=10.32μb-34.18
R2=0.94
Perfusion reduction %
Heamatoma volume (ml)
Blood viscosity (cP)
(b)
ΔF=0.04μb'+4.91
R2=0.67
V'=10.35μb'-17.63
R2=0.94
Perfusion reduction %
Haematoma volume change %
3.6 cP
Blood viscosity %
(c)
ΔF=0.61(p*)+4.89
R2=0.95
V=42.27e-1.26(p*)
R2=0.996
Reduced perfusion %
Heamatoma volume (ml)
Pressure (mmHg)
(d)
V- = 58.68ln(p')-253.71
R2 = 0.92
ΔF=0.0061(p')+4.8918
R2=0.95
Reduced perfusion %
Haematoma volume reduction %
+1 mmHg
Pressure change
(e)
ΔF=1.14(pa)-78.39
R2=0.99
V=0.034(pa)-1.91
R2=0.95
Reduced perfusion %
Heamatoma volume (ml)
Blood pressure (mmHg)
(f)
ΔF= 0.80pa' + 1.15
R2 = 0.99
V+ = 4.73pa' + 0.99
R2 = 0.95
Reduced perfusion %
Haematoma volume increase %
Blood pressure change %
(g)
ΔF=1.34ln(Lp)+45.21
R2=0.98
V=0.1ln(Lp)+2.8
R2=0.97
Perfusion reduction %
Haematoma volume (ml)
Hydraulic permeability [m/(Pa*s)]
(h)
V+=642.93ln(Lp')-3403
R2=0.97
ΔF=1.38ln(Lp')-1.96
R2=0.98
Perfusion reduction %
Haematoma volume increase %
Hydraulic permeability change %

1

Figure 5.8. Variations in perfusion reduction and haematoma volume as functions of (a) blood viscosity, (c) the definition of haematoma surface pressure, (e) blood pressure (source pressure) and (g) hydraulic permeability. Measures of importance of perfusion reduction and haematoma volume change as functions of (b) viscosity change, (d) the definition of haematoma surface pressure change, (f) blood pressure change, (h) hydraulic permeability. ΔF denotes perfusion reduction. V denotes the haematoma volume, V' denotes the haematoma volume change. V^- denotes reduced haematoma volume and V^+ denotes increased haematoma volume. $\mu_b^{'}$ denotes the blood viscosity change, p' denotes the definition of haematoma surface pressure change and $p_a^{'}$ denotes the blood pressure change. Note that the right y axis in (c) is shown in logarithmic scale at a base of e.

Higher hydraulic permeability results in larger perfusion reduction and haematoma volume, as shown in Figures 5.8(g) and 5.8(h). When the permeability increased by four orders of magnitude from $10^{-12}\ m/(Pa\cdot S)$, the perfusion reduction increased from $7.89\,\%$ to $16.7\,\%$ and the haematoma volume increased from 0.017ml to 0.66ml.

5.4 Discussion

In this study, a model of HT has been developed in a full brain model to examine the relationship between the bleeding region with HT and to investigate how HT can be affected by various haemodynamic parameters. This simulation is based on the model proposed by Wang and Payne (2021), which presents a mathematical model of HT after ischaemic stroke. They investigated how changes in vascular geometry can affect the severity of HT. To develop further these simulations, Wang et al. (2022b) simulated the HT in a penetrating network to determine how HT can affect healthy blood vessels and tissues. In this study, this HT model has further developed into a computational whole brain model to investigate the correlation between bleeding region and haematoma. The HT was quantified and validated the results with a set of clinical images to simulate

the bleeding region of haematomas. By using the optimised parameters, a HT scenario was established to investigate the haemodynamic factors that may affect HT.

In the quantification of HT for real clinical image data, the author controlled the haematoma volumes and centres by adjusting the infarcted regions and capillary pressure manually to approach the haematoma volumes and centres obtained from CT images. The coordinate points of haematoma centres both from these models and CT images are compared in Figure 5.6(a) by t-test. All p-values of x, y and z values of haematoma centres are > 0.05. Aligning the y-values, however, proved to be relatively difficult compared to processing the other two values. This is due to different patients having different geometries of brains; thus, the origin of the coordinate system will be slightly different comparing with the computational model, i.e., the accurate coordinate of the bottom of oblongata is challenging to determine. In addition, the resolution of the computational brain subregion also leads to some differences. This should be addressed more rigorously in the future.

The voxel-based dice similarity coefficient (DSC), which was proposed by Dice (1945), is commonly used to quantify the area overlap between the algorithm and manually segmented regions for patients with various diseases (Zhou et al., 2020, Griffis et al., 2016, Chai et al., 2012, Yamamoto et al., 2012, Edmund et al., 2014). However, DSC can only be calculated based on two images shown by pixels or voxels. In this study, the computational brain model is mesh-based, whereas the CT images are pixel-based. Thus, the overlap regions of HT from the computational brain model and CT images are

difficult to determine and define. In addition, it is challenging to determine the region of interest since the geometries of patients' brains vary from one patient to another.

In this study, the location and the volume of haematoma are the primary focus. However, the shape of the haematoma is not validated with the CT images since the main aim of this study is to optimise the model parameters (for example, p^{ι}) and to investigate the factors that may influence the severity of HT. The author suggests, however, that the shape of the haematoma should be determined in the next study to locate the bleeding region more accurately. DSC (Dice, 1945) (to determine the overlap) and symmetric correspondence method (Papademetris et al., 2002) (to obtain the difference in boundaries) are potential ways to quantify the shape difference.

In the comparison of the haematoma volumes between the CT scan and the computational model, no statistically significant difference was found. The results of haematoma volumes from the simulations are close to the clinical data. From the 15 patients, 5 are HI1, 5 are HI2 and 5 are PH1. All haematoma volumes are less than $5\,ml$. Results were not split up into the different types since these imaging data was used to optimise the model parameters. Different types of HT provide nearly the same results, for example, the optimised p^{ι} was found to be $3.5\,mmHg$ for all types of HT. The PH2 patients were not included at this stage since this model is not able to investigate HT with large tissue displacement, especially for patients with a significant MLS.

As shown in Figure 5.7, a reduction in perfusion is found following HT, in the range of $5-16\,\%$. Jain et al. (2013) compared the CT perfusion parameters for a control group and an HT group: the mean reduction rate of relative cerebral blood flow (rCBF) was

found to be $10 \pm 4.3\%$ $(5.7-14.3\%)$, which is in good agreement with the results presented here (note this experimental result of rCBF is not obtained from MR CLEAN-NO IV). Since rCBF was calculated clinically from data collected on the ipsilateral side compared with the contralateral (healthy) side, the same method was used to determine the reduction of perfusion in these simulations (noting that the comparison is not exact).

Wang et al. (2022b) predicted that the reduction of perfusion in a penetrating network voxel, which is in the size of $1 \times 1 \times 2.5\,mm$, is approximately $13-17\%$ after HT onset. The results presented here are found to be smaller than the perfusion reduction from the penetrating network. The author suggests that this is because different sizes of regions of interest are selected.

In this study, results show that increased blood viscosity has the potential to increase the volumes of haematoma. Çinar et al. (2001) measured the correlations between blood glucose with blood viscosity: when the mean value of blood glucose increased from $100-400\,mg/dL$, viscosity increased by 25% ($r=0.59, P=0.002$). Mushtaq et al. (2019) also found that hyperglycaemia is associated with blood viscosity. A phenomenon that increased baseline glucose levels were associated with overall symptomatic intracerebral haemorrhage (sICH) occurrence was proposed by van der Steen et al. (2022) . The simulations from this model support the hypothesis that increased blood glucose levels lead to a higher level of severity of HT if the high blood glucose level results in higher blood viscosity.

In addition, high blood glucose and high blood pressure are linked, since high levels of sugar in blood can lead to atherosclerosis (Bays et al., 2005, Brown and Goldstein, 1984, Libby, 2002). As shown in Figure 5.8(e), higher blood pressure leads to a larger haematoma and a larger reduction in perfusion, as would be expected. Blood pressure acts as a driving force of HT in this model. The results thus also support the results proposed by van der Steen et al. (2022): i.e., that increased baseline systolic blood pressures can increase overall sICH occurrence. The results have further indicated that high levels of blood glucose result in a more severe form of HT.

It should be noted that in this simulation, the time dynamics were not included since all images were taken at the time of CT scanning. Thus, the dynamic process of haemostasis was not considered. However, one important aspect of a reduction in cerebral blood volume (CBV) caused by haemostasis should be considered in the following stages of model development due to localized vasoconstriction occurring before haemostasis starts (Armstrong and Golan, 2011). Localized vasoconstriction caused by haemostasis could also lead to significant capillary compression but here it was assumed that increased intracranial pressure (ICP) was the primary source of reduced CBV. It also indicates that further studies are needed to determine the dynamic correlations between variations in perfusion reduction and haematoma volume.

To the best of the author's knowledge, there are very limited available experimental data that propose rigorous definitions of the haematoma boundary using physical parameters after HT onset, especially for HT in the full brain. Wang and Payne (2021) and Wang et al. (2022b) set the definition of haematoma boundary at $0.1\,mmHg$ above

tissue pressure, which was found to ensure a haematoma radius close to experimental data in mice: Jenkins et al. (1989) measured the distance between the haematoma boundary and related damaged vessels as $700\,\mu m$. However, these simulations were based on a single leaky vessel and in relatively small regions of interest, compared to the full brain model.

It can be seen from Figure 5.8(c) that haematoma volume is highly sensitive to the definition of haematoma boundary pressure. Since the haematoma boundary was drawn manually from clinical imaging data, the identification of the haematoma boundary may be different from the haematoma definition based on experimental data from individual vessels in mice (Jenkins et al., 1989, Wang and Payne, 2021). To keep the size of haematoma volume to a reasonable size compared with clinical data (van Kranendonk et al., 2020), the author optimised the definition of haematoma surface pressure, $p^{¿}$, and found this to be $3.5\,mmHg$ above tissue pressure in this simulation.

Regarding the identifiability aspects of the model, nearly all the parameters are likely to vary from one patient to another (to a greater or lesser degree). The hydraulic permeability L_p is suspected to be one of the most likely values to vary significantly from one patient to another, although obtaining experimental measurements of this parameter is highly challenging. The sensitivity analysis for the hydraulic permeability L_p is shown in Figures 5.8(g) and 5.8(h). Future work will be required to confirm the hydraulic permeability for different types and locations of HT, which will be required to predicting the severity of HT more accurately.

In addition, the author has only one computational brain model with a specific shape, while the geometries of patient brains vary from one patient to another. Although the coordinate points of haematoma centres (described using percentage values) were used in this simulation to eliminate the influence of the different shapes between the brain model and real patients' brains, more adaptive brain models will be needed in the future to fit different brain shapes. One of the potential models has been proposed by Jozsa et al. (2022): the anatomical (geometrical) fitness of the brain models was evaluated by comparing the simulated grey and white matter volumes to measurements in healthy reference subjects. Thus, various patients can be compared with every computational brain which is adjusted to geometry. The same method can be used in future to fit this computational brain model with specific patient brains.

As shown in Figure 5.5, the bleeding region and haematoma are both present in the brain model. However, this model is not able to locate the specific bleeding vessels. Since the vessel geometry varies from one patient to another, it is challenging to determine the bleeding vessels. It is suggested that the bleeding regions will need to be validated in the future as and when the relevant clinical data become available.

The long-term aim of this work is to identify those patients who are most at risk of haemorrhage based on imaging data (and other non-imaging parameters) and to predict the occurrence and severity of HT. However, this model still has many limitations to predict HT. One of the potential methods to develop a prediction model is linking HT with oedema. Oedema and HT were found to be highly associated after stroke and oedema was commonly assumed as a leading factor of HT (Vemmos et al., 2004). In

addition, oedema could potentially be examined and identified by a wearable ultrasound device such as that invented by Wang et al. (2022a). Thus, HT could in future become much more predictable by applying a wearable ultrasound device combined with this model relating oedema and haematoma.

5.5 Conclusion

Through the development of a mathematical model to simulate HT in a computational brain model, validation with real clinical images is possible through the comparison between haematoma geometry, locations, and perfusion change. This study has identified that a reduction in perfusion after HT onset is in the range of $5-16\,\%$, which is with good agreement with experimental data. One of the more significant results found here is that increased blood glucose level and high blood pressure lead to more severe HT, as observed clinically:

- $1\,\%$ increase in blood viscosity reduces perfusion by $0.0434\,\%$ and increases haematoma volume by $10.35\,\%$ from baseline.
- $1\,\%$ increase in blood pressure reduces perfusion by $0.80\,\%$ and increases haematoma volume by $4.73\,\%$from baseline.

This model is the first such to be able to simulate the correlation between bleeding regions and haematoma and should be of assistance in future to assess HT for clinicians.

5.6 Evaluating the Model: Advantages and Limitations

The following table (Table 5.3) discusses whether this study has successfully addressed its three primary objectives from the perspectives of modelling, physiology, and clinical practice. A summary of highlights and assumptions is listed in Table 1.1.

Table 5.3. Model accomplishments and limitations

Model:	Whole computation brain model
Objectives:	Modelling objective
Completed aspects:	• Governing mathematical equations to describe HT in a whole computation brain model has been developed. This model works as the final step for the whole study. • The possible regions susceptible to haemorrhage have been considerably narrowed down. • It is now feasible to obtain vital clinical markers, such as the volume of the haematoma, which bear a significant comparability with data obtained from actual clinical practice.
Unfinished aspects and limitations:	• This model, however, has its limitations and is not able to pinpoint the precise location of the bleeding vessels accurately. • Owing to a dearth of experimental data, certain vital parameters such as the surface pressure of the haematoma

	must be manually adjusted, potentially leading to inaccuracies. • The research conducted lacks the necessary validation of the identified areas prone to bleeding through the use of clinical imaging data. Consequently, the precision in determining the locations of potential bleeding areas remains a challenge.
Objectives:	Physiology perspective
Completed aspects:	• The model incorporates the biomechanics of the brain tissue into its calculations. The distribution of pressure within the tissue is derived from a previously validated brain model, thereby maintaining consistency and accuracy in its results.
Unfinished aspects and limitations:	• The BBB breakdown in blood vessels from previous model is not used here. Instead, it operates under the assumption that subregions serve as the origins of haemorrhaging. • Even though the definition of hematoma surface pressure is validated with clinical data by comparing hematoma volume and locations from both the model and clinical data, the inconsistency and inaccuracy of manually drawn hematomas by clinicians present challenges in determining the accuracy of the hematoma surface definition. A further set of clinical imaging data, along with a standard for delineating the boundary of the hematoma based on physiological data, will be crucial for future studies (It's evident that relying solely on visual inspection and

	colour differences to differentiate between healthy tissue and a hematoma is not very reliable or trustworthy).
Objectives:	Clinical objective
Completed aspects:	• This model is able to assist clinicians to narrow the suspected region of bleeding before the surgery or treatment. Saving time to assess the vulnerable blood vessels and tissue.
Unfinished aspects and limitations:	• The model's ability to accurately predict regions susceptible to bleeding necessitates further validation through comparison with clinical data. • The model requires manual adjustment of the simulated haemorrhage region. Consequently, the time taken to achieve the final results is considerably prolonged, reflecting a potential area for optimization in the model's operational efficiency. • In order to apply this model into clinical setting, it is critical to note that the computational brain model should exhibit variability from one patient to another. This suggests that the current model's capacity for personalization is limited, which is a significant constraint for its practical clinical application.

5.7 Appendix

Appendix 5.A Discussion of model coupling procedures

Table 5.4 Critical appraisal of steps in model coupling (section 5.2.3)

Steps	Comments

#1	• This is the starting point for the whole model.
#2	• In the present stage of this procedure, the selection of occluded subregions is undertaken manually, contributing to the difficulty in exerting control over the ambiguity associated with the bleeding region. Confirmation of both the dimensions and the location of the hematoma is achieved; however, the validation of the bleeding regions and occluded regions is unfortunately absent at the end.
#3	• In this step, the assumption is held that capillaries are the only vessels prone to leakage during the event of a HT, representing a significant limitation of the model. • Patient-specific capillary pressure ranges are designated manually, giving rise to uncertainties regarding the precise regions of haemorrhage. • Another noteworthy constraint of this model is the lack of validation of capillary pressure in bleeding region, which potentially hinders its reliability and application accuracy.
#4	• The bleeding regions are chosen as the source of HT.
#5	• In the present model, haematomas are characterized as regions where interstitial pressure exceeds 3.5 mmHg. This definition, however, lacks substantiation through experimental data, representing a potential point of inaccuracy. • Attributable to the constraints of imaging resolution and the

	ambiguity inherent in the manual delineation of the haematoma region by clinicians, disparities may emerge in the assessment of haematoma location and volume.

1

Chapter 6: Conclusion, Final Discission and Future Direction

6.1 Thesis Summary

In this thesis, a mathematical method to develop a haemorrhagic transformation model is described. This model has been applied in 2D and 3D at both micro and macro length scales and has been qualitatively validated to a certain degree against clinical data.

In the first study, a mathematical model to simulate the severity of HT in the microvasculature is proposed. It is possible to use this fundamental model to simulate the behaviour of HT in various vessels with different geometries. This study has identified that the haematoma radius is largely invariant of the vessel geometry. The model thus indicates that arterioles and venules can cause larger volumes of haematoma than the capillary generation. One of the more significant findings to emerge from this study is that capillary compression has been shown to have a greater impact on venules than on the arteriole and capillary generations. Meanwhile, this study has found that capillary compression is able to reduce the leakage fraction of blood flow and hence to restrain the development of a haematoma.

In the second model, this mathematical model is applied on a multi-scale microvasculature network. This model indicates that larger vessel breakdown leads to larger haematoma radius, higher tissue displacement and higher ICP. These results may be able to explain the different categories of HT that have been found clinically. One of

the more significant highlights is that this simulation of HT can be compared based on the reductions in both cerebral blood volume and perfusion. A reduction in CBV in the range of 20–25 % and in perfusion of approximately 13–17 % after HT onset are determined. The solutions and insights gained from this study may be of assistance in future to assess the impact of the HT on an enlarged 3D tissue region and at a whole-brain scale.

In the third model, the previous mathematical HT model is extended into a computational brain model. The key parameters are validated with clinical imaging data to generate an optimised HT model which fits a full brain. Then the correlations of reduced perfusion and haematoma volume with glucose levels are investigated, which support the clinical findings. Based on the computational whole brain model, the perfusion is found to be reduced by $5-16\%$after HT onset. The results are in good agreement with the clinical data. It is shown that the haematoma volume will increase when blood viscosity is above a threshold (but reduce below this threshold), and for patients with high blood pressure, which indicates that increased blood glucose and hypertension both lead to higher severity of HT. The sensitivity analysis, varying the definition of haematoma surface pressure and blood pressure to determine the severity of HT, was emphasized at the end of this model.

Developing these models from 2D to 3D bridges the gap between the mathematical HT model and clinical imaging data. This study provides the first whole brain prediction model for HT assessment. However, this study has several limitations.

Limitations of Chapter 3 and Chapter 4:

1. The BBB breakdown is assumed to be a uniform process, with an evenly distributed leakage.
2. The tissue is assumed to be a homogeneous material.
3. The definition of haematoma surface pressure presents a significant challenge for validation.
4. The current model is limited to be assist clinicians to predict HT after stroke yet.
5. The validation with clinical imaging data is missing.

Limitations of Chapter 5:

1. While this model provides valuable insights, it has limitations, including the inability to accurately identify the precise location of bleeding vessels.
2. Due to a lack of experimental data, certain critical parameters such as the hematoma surface pressure require manual adjustment, which could lead to inaccuracies.
3. This model does not utilize the blood-brain barrier (BBB) breakdown from previous models. Instead, it assumes that subregions act as the sources of haemorrhaging.
4. For future studies, additional clinical imaging data and a standard method for determining hematoma boundaries based on physiological data will be essential.
5. The model necessitates manual adjustments of the simulated haemorrhage region, resulting in a lengthy process to achieve the final results. This indicates

a potential area for enhancing the model's efficiency.

6. For clinical application, it is important to note that the computational brain model should reflect the variability among individual patients. This points to a limitation in the current model's ability for personalization, posing a significant challenge for its practical clinical usage.

6.2 Further Discussion

6.2.1 Temporal scales

In the context of this model, the focus is directed towards changes that, although slow, maintain a quasi-steady state. Nevertheless, these changes occur quick enough to exclude the influence of other factors such as the effects of haemostasis. Upon computation, it was found that the time required for the formation of a small haematoma (with a radius of $150\,\mu m$) is approximately 1.4 minutes. In contrast, a common size haematoma (with a radius of $10\,mm$) necessitates around 8 minutes for formation. The comparative analysis between the haematoma formation time and the process of haemostasis is elaborated upon in Chapter 3. It suggests that during the specific time frame of HT, the HT process can be presumed to be in a quasi-steady state.

6.2.2 Therapy optimisation

The primary clinical objectives of this study encompass determining the predictability of HT, and aiding clinicians in identifying haemorrhaging vessels or confining potential

bleeding regions, thereby reducing the duration of treatment. To a certain extent, the current study has provided some answers to these queries.

The conceptualization of the HT model, applicable to a single vessel and a penetrating network, has the potential to enhance clinicians' understanding of the dynamics of HT formation. However, due to the limitations of contemporary imaging technology, the detection of individual capillaries remains a formidable challenge. Once advancements in technology enable the precise detection of blood vessel geometry, this model could be harnessed to identify vulnerable vessels effectively.

The forthcoming model, structured within a comprehensive computational brain model, is able to prove instrumental in aiding clinicians to pinpoint and limit suspected haemorrhagic regions, thereby expediting the treatment process. Meanwhile, the identification of potential bleeding areas provides a critical advantage for surgical planning by enabling the avoidance of sensitive regions, thus fostering an overall improvement in surgical outcomes.

However, the pivotal question of whether this model can assist clinicians in predicting HT has not been effectively addressed. Further discussion on potential solutions and future work pertaining to this issue will be presented in the Section 6.3 of this chapter.

6.2.3 Verification, validation, and uncertainty quantification

As discussed earlier, this simulation results still have gap between clinical data. Thus, it is necessary to use the framework for verification, validation, and uncertainty quantification (VV&UQ) to help determine the uncertainties.

Verification and validation:

In this study, the methods proposed by Pathmanathan and Gray (2014) are suggested to be used. Thus, the verification process is split into code verification and solution (or calculation) verification.

Regarding code verification, based on the methods proposed by Oberkampf and Roy (2010), several different criteria can be employed to verify a scientific computing code. These criteria, arranged from the least to the most rigorous, are as follows:

1. simple tests,
2. code-to-code comparisons,
3. discretization error quantification,
4. convergence tests,
5. order-of-accuracy tests.

In this study, convergence tests are conducted to verify the codes in Chapter 4. It's noteworthy that the governing equations in Chapter 3 and Chapter 4 are similar. Notably, the coding section in Chapter 5, not pertinent to this thesis, was composed by my colleague, Xi Chen.

Solution (or calculation) verification can be divided into (Oberkampf and Roy, 2010):

1. verification of input data,
2. verification of post-processing tools,
3. numerical error estimation

In this model, the input data adheres to several consistency checks:

- Parameter Consistency: The values of the parameters are ensured to be coherent with each other and appropriate for the problem domain.
- Model Structure Consistency: The compatibility of the selected mathematical models is verified, ensuring they work harmoniously within the model structure.
- Hardware and Software Consistency: The model confirms the fulfilment of hardware and software requirements, ensuring a seamless execution environment.

The pseudo-algorithms used for post-processing tools are presented in Chapter 3. It's important to note that numerical errors couldn't be eliminated in this study. All coding was executed successfully in MATLAB 2022a, which operates using a default precision format of 'double'.

Validating computational results with clinical data in Chapter 3 and 4 was challenging due to the lack of experimental haematoma data at the microvasculature network level. However, in Chapter 5, the author is able to compare the computed haematoma volume, haematoma locations, cerebral blood volume (CBV), and perfusion change with clinical data. However, the use of a validation matric , see example in Oberkampf and Roy (2010), was not feasible in this study, as the clinical brain model is individualized and haematoma location varies between different patients.

Uncertainty quantification

Due to the lack of experimental data in Chapters 3 and 4, along with the personalized brain geometries and haematoma conditions in the clinical data for Chapter 5, quantifying all uncertainties, such as model input uncertainty and numerical uncertainty, proves to be a significant challenge. As a result, providing these uncertainties in a cumulative distribution function (y-axis) with haematoma volume on the x-axis is a complex task.

6.3 Future Work

Future works will be needed to improve the existing model. It is emphasized that the final aim of this HT model is to predict the HT after ischaemic stroke onset, either caused by the progression of ischaemic stroke or the treatment with thrombolytic therapy. However, this model, introduced in this thesis, concluded by investigating which factors could affect the severity of HT by using a validated full brain HT model. It is suggested that an investigation of the combination of oedema and HT could be considered as a key solution to predict the HT after ischaemic stroke.

In addition, the formation of HT depends on many factors as previously discussed. Several future works to optimise this model are suggested here, including the modelling of BBB breakdown based on TJs and considering the effect of vasoconstriction due to haemostasis.

These studies will be useful in the development of an improved prediction model for clinicians. However, these future works will require the combination of oedema model,

will also involve laboratory experiments to acquire relevant information and clinical trials to validate the prediction model. These proposed works are described below.

6.3.1 Oedema and HT model

In this model, predicting the occurrence and severity of HT was found to be challenging by using haemodynamic and clinical images. The main concern is that it is difficult to assess the weakness of the blood vessels after ischaemic stroke either based on CT images or MRI images due to the limitations of resolution. Angiography is a technique that can be used to observe the vessel structure but also has limitations to determine the capillary properties. An angiography takes 1.5 hours in average, which is likely to be inefficient for HT patients (Heiserman et al., 1994).

Another main concern is that this model requires manual adjustment of the simulated haemorrhage region. Consequently, the time taken to achieve the final results is considerably prolonged, reflecting a potential area for optimization in the model's operational efficiency. Thus, other leading factors that can predict HT are needed in the future model. The formation of oedema can be considered as one leading factor to predict HT and an alternative method.

This is because oedema and HT were found to be highly associated after stroke and oedema was commonly assumed as a leading factor of HT (Vemmos et al., 2004). The HT is considered as the final phase of endothelial dysfunction after oedema onset (Bar and Biller, 2018). Oedema is relatively easier to detect compared with determining HT. Oedema is potentially to be examined and identified by a wearable ultrasound device

invented by Wang et al. (2022a). This wearable ultrasound device can work 2 days after patients leave hospitals and detect the formation of oedema continuously. Thus, HT could be more predictable by applying this wearable ultrasound devices combined with the models of correlations of oedema and haematoma. It is noted that a clinical trial should be approved in the future to test these ultrasound devices' performance to detect oedema in brain.

In addition, a validated oedema model was developed by Mokhtarudin and Payne (2015). By using this model, it is worth investigating the joint effects of oedema and HT on brain tissue. In addition, the time dynamics of endothelial dysfunction could be included in these future studies to determine the sequence of occurrence of the oedema and the HT, validated with adequate clinical imaging data.

6.3.2 Virtual Imaging in validation

Chapter 5 provides a discourse on the limitations posed by the employment of a single comprehensive computational brain model. The diversity in brain geometries across individual patients instigates challenges in the validation of HT, thereby complicating the process considerably. However, the development of a personalized brain model that accurately replicates every patient's brain remains a challenge. Predominantly, brain models are derived from an assortment of samples, where the geometry is averaged to establish a singular final representation (Huang et al., 2016, Guo et al., 2018).

The personalized brain model for every patient is vital to validate the HT model with clinical MRI or CT images. Jozsa et al. (2022) proposed a method to personalize the brain

model for every patient. This approach begins by creating a general mesh template in the standard space, followed by an affine registration of this template to the tissue mask of each specific subject. The total brain volume of healthy controls tends to be overestimated by 58 ml (on average 5%) by the corresponding brain models. The primary advantages of this method are twofold: it avoids time-consuming and frail patient-specific geometry reconstruction (Oostenveld et al., 2011).

The limitations of this personalized brain model pose constraints for further validation of HT simulation:

- The simulations rely on physiological parameters that can't yet be experimentally determined. These parameters are crucial for understanding vascular resistance within the brain tissue.
- The model doesn't account for compensatory mechanisms like collateralisation, which are important in reducing the risk of infarcts. The model also doesn't include processes responsible for the absence of reperfusion after recanalization.

6.3.3 BBB breakdown modelling

BBB breakdown has a complex mechanism. The mechanism starts during ischaemia and hypoxia, which involves a series of molecular cascades (Yang and Rosenberg, 2011). The model introduced in this thesis, on the one hand, is limited to include modelling the production of matrix metalloproteinase 9 and matrix metalloproteinase 2 (MMPs). The enzymes of these are secreted to weaken the extracellular matrix in tissue remodelling processes (Murphy and Knäuper, 1997). The correlation of MMPs productions and the

treatment of ischaemic stroke is suggested to be considered for prediction of HT. On the other hand, the BBB breakdown modelling for HT is more complex than oedema modelling, since the leakage of blood cells and plasma should be investigated separately. The size of TJs constrains the leakage of blood cells. In this thesis, the mechanism of blood cells leakage was considered separately due to the lack of experimental data.

The process of blood cells leakage might involve various cell behaviours and interactions such as cell signalling, cell movement, cell growth and death. The Cellular Potts Model (CPM) is an example of a computational modelling method that simulates cellular interactions, which was developed by Graner and Glazier (1992) to study cell sorting and also has been used in describing various biological phenomena, for example tumour growth (Chen et al., 2007), tumour invasion into healthy tissue (Szabó and Merks, 2013), and progenitor cell sorting (Krieg et al., 2008). Implementation of CPM to model the cell-cell interactions during cerebral ischaemia may provide a better understanding of infarct formation and the interactions between the endothelial cells with blood cells.

6.3.4 Haemostasis

In Chapter 3, the estimation of haemostasis rate and formation rate of haematoma was discussed. The time scale of haemostasis is at least 3 times slower than the formation time of a haematoma. However, one aspect of reduction in cerebral blood volume (CBV) caused by haemostasis should be considered in the following stages of model development due to localized vasoconstriction occurring before haemostasis starts

(Armstrong and Golan, 2011). Localized vasoconstriction caused by haemostasis could also lead to capillary compression but in this model, the increased intracranial pressure (ICP) was assumed to be the only source of reduced CBV.

Based on the author's best knowledge, however, there is no current experimental data that quantifies the direct impact of haemostasis to vasoconstriction in human. Further study of vasoconstriction will require more experimental data.

6.4 Final Remark

The models developed in this thesis are useful to evaluate factors that affect the severity of HT. Although the models pose several limitations, the recommended future studies will hopefully help to improve the models and translate them to assist clinicians and researchers to further assess and treat HT.

References:

AASLID, R., MARKWALDER, T.-M. & NORNES, H. 1982. Noninvasive transcranial Doppler ultrasound recording of flow velocity in basal cerebral arteries. *Journal of neurosurgery*, 57**,** 769-774.

ABBOTT, N. J., PATABENDIGE, A. A., DOLMAN, D. E., YUSOF, S. R. & BEGLEY, D. J. 2010. Structure and function of the blood–brain barrier. *Neurobiology of disease*, 37**,** 13-25.

ACOSTA, S., PENNY, D. J. & RUSIN, C. G. 2015. An effective model of blood flow in capillary beds. *Microvascular Research*, 100**,** 40-47.

ADAMS JR, H. P., BENDIXEN, B. H., KAPPELLE, L. J., BILLER, J., LOVE, B. B., GORDON, D. L. & MARSH 3RD, E. 1993. Classification of subtype of acute ischemic stroke. Definitions for use in a multicenter clinical trial. TOAST. Trial of Org 10172 in Acute Stroke Treatment. *stroke*, 24**,** 35-41.

AIFANTIS, E. 1980. On the problem of diffusion in solids. *Acta Mechanica*, 37**,** 265-296.

ALASTRUEY, J., PARKER, K., PEIRÓ, J., BYRD, S. & SHERWIN, S. 2007. Modelling the circle of Willis to assess the effects of anatomical variations and occlusions on cerebral flows. *Journal of biomechanics*, 40**,** 1794-1805.

ÁLVAREZ-SABÍN, J., MAISTERRA, O., SANTAMARINA, E. & KASE, C. S. 2013. Factors influencing haemorrhagic transformation in ischaemic stroke. *The Lancet Neurology*, 12**,** 689-705.

AMES, A. R., WRIGHT, R. L., KOWADA, M., THURSTON, J. & MAJNO, G. 1968. Cerebral ischemia. II. The no-reflow phenomenon. *The American journal of pathology*, 52**,** 437.

ARENILLAS, J. F. & ÁLVAREZ-SABÍN, J. 2005. Basic mechanisms in intracranial large-artery atherosclerosis: advances and challenges. *Cerebrovascular Diseases*, 20**,** 75-83.

ARMSTRONG, A. W. & GOLAN, D. E. 2011. Pharmacology of hemostasis and thrombosis. *Principles of Pharmacology: The Pathophysiologic Basis of Drug Therapy. 3rd ed. Philadelphia: Lippincott Williams & Wilkins*, 372-400.

ASAHI, M., WANG, X., MORI, T., SUMII, T., JUNG, J.-C., MOSKOWITZ, M. A., FINI, M. E. & LO, E. H. 2001. Effects of matrix metalloproteinase-9 gene knock-out on the proteolysis of blood–brain barrier and white matter components after cerebral ischemia. *Journal of neuroscience*, 21**,** 7724-7732.

ASSOCIATION, S. 2016. Stroke statistics.

ASSOCIATION, S. 2018. Stroke statistics.

ATTWELL, D., BUCHAN, A. M., CHARPAK, S., LAURITZEN, M., MACVICAR, B. A. & NEWMAN, E. A. 2010. Glial and neuronal control of brain blood flow. *Nature*, 468**,** 232-243.

AVMAN, N. & BERING, E. A. 1961. A plastic model for the study of pressure changes in the circle of Willis and major cerebral arteries following arterial occlusion. *Journal of Neurosurgery*, 18**,** 361-365.

BAI, M., ELSWORTH, D. & ROEGIERS, J. C. 1993. Multiporosity/multipermeability approach to the simulation of naturally fractured reservoirs. *Water Resources Research*, 29**,** 1621-1633.
BAISH, J. W., NETTI, P. A. & JAIN, R. K. 1997. Transmural coupling of fluid flow in microcirculatory network and interstitium in tumors. *Microvascular research*, 53**,** 128-141.
BALLABH, P., BRAUN, A. & NEDERGAARD, M. 2004. The blood–brain barrier: an overview: structure, regulation, and clinical implications. *Neurobiology of disease*, 16**,** 1-13.
BAR, B. & BILLER, J. 2018. Select hyperacute complications of ischemic stroke: cerebral edema, hemorrhagic transformation, and orolingual angioedema secondary to intravenous Alteplase. *Expert Review of Neurotherapeutics*, 18**,** 749-759.
BARKER, S. J. 1998. Blood Volume Measurement The Next Intraoperative Monitor? *Anesthesiology: The Journal of the American Society of Anesthesiologists*, 89**,** 1310-1312.
BAYIN, Ş. S. & BAYIN, Ş. S. 2006. *Mathematical methods in science and engineering*, Wiley Online Library.
BAYS, H., ABATE, N. & CHANDALIA, M. 2005. Adiposopathy: sick fat causes high blood sugar, high blood pressure and dyslipidemia.
BEAR, J. 1988. *Dynamics of fluids in porous media*, Courier Corporation.
BEDEKAR, D., JENSEN, T. & SCHMAINDA, K. M. 2010. Standardization of relative cerebral blood volume (rCBV) image maps for ease of both inter-and intrapatient comparisons. *Magnetic resonance in medicine*, 64**,** 907-913.
BENTIVOGLIO, Y. & GOLDBERG, M. 1988. From cardiac catheterization data to hemodynamic parameters. *Philadelphia, PA, FA Davis Co*, 189-255.
BERKHEMER, O. A., FRANSEN, P. S., BEUMER, D., VAN DEN BERG, L. A., LINGSMA, H. F., YOO, A. J., SCHONEWILLE, W. J., VOS, J. A., NEDERKOORN, P. J. & WERMER, M. J. 2015. A randomized trial of intraarterial treatment for acute ischemic stroke. *n Engl J Med*, 372**,** 11-20.
BING, Y., GARCIA-GONZALEZ, D., VOETS, N. & JÉRUSALEM, A. 2020. Medical imaging based in silico head model for ischaemic stroke simulation. *Journal of the mechanical behavior of biomedical materials*, 101**,** 103442.
BIOT, M. A. 1941. General theory of three-dimensional consolidation. *Journal of applied physics*, 12**,** 155-164.
BIOT, M. A. 1962a. Generalized theory of acoustic propagation in porous dissipative media. *The Journal of the Acoustical Society of America*, 34**,** 1254-1264.
BIOT, M. A. 1962b. Mechanics of deformation and acoustic propagation in porous media. *Journal of applied physics*, 33**,** 1482-1498.
BIOT, M. A. & WILLIS, D. G. 1957. The elastic coefficients of the theory of consolidation.
BISHOP, C., POWELL, S., RUTT, D. & BROWSE, N. 1986. Transcranial Doppler measurement of middle cerebral artery blood flow velocity: a validation study. *Stroke*, 17**,** 913-915.

BLINDER, P., SHIH, A. Y., RAFIE, C. & KLEINFELD, D. 2010. Topological basis for the robust distribution of blood to rodent neocortex. *Proceedings of the National Academy of Sciences*, 107**,** 12670-12675.

BOAS, D. A., JONES, S. R., DEVOR, A., HUPPERT, T. J. & DALE, A. M. 2008. A vascular anatomical network model of the spatio-temporal response to brain activation. *Neuroimage*, 40**,** 1116-1129.

BOITEN, J. & LODDER, J. 1991. Lacunar infarcts. Pathogenesis and validity of the clinical syndromes. *Stroke*, 22**,** 1374-1378.

BORDONI, L., LI, B., KURA, S., BOAS, D. A., SAKADŽIĆ, S., ØSTERGAARD, L., FRISCHE, S. & GUTIÉRREZ-JIMÉNEZ, E. 2020. Quantification of capillary perfusion in an animal model of acute intracranial hypertension. *Journal of Neurotrauma*.

BOUDREAU, D. M., GUZAUSKAS, G., VILLA, K. F., FAGAN, S. C. & VEENSTRA, D. L. 2013. A model of cost-effectiveness of tissue plasminogen activator in patient subgroups 3 to 4.5 hours after onset of acute ischemic stroke. *Annals of emergency medicine*, 61**,** 46-55.

BOURCIER, R., GOYAL, M., LIEBESKIND, D. S., MUIR, K. W., DESAL, H., SIDDIQUI, A. H., DIPPEL, D. W., MAJOIE, C. B., VAN ZWAM, W. H. & JOVIN, T. G. 2019. Association of time from stroke onset to groin puncture with quality of reperfusion after mechanical thrombectomy: a meta-analysis of individual patient data from 7 randomized clinical trials. *JAMA neurology*, 76**,** 405-411.

BROUNS, R. & DE DEYN, P. 2009. The complexity of neurobiological processes in acute ischemic stroke. *Clinical neurology and neurosurgery*, 111**,** 483-495.

BROWN, M. S. & GOLDSTEIN, J. L. 1984. How LDL receptors influence cholesterol and atherosclerosis. *Scientific American*, 251**,** 58-69.

BUXTON, R. B. & FRANK, L. R. 1997. A model for the coupling between cerebral blood flow and oxygen metabolism during neural stimulation. *Journal of cerebral blood flow & metabolism*, 17**,** 64-72.

BUXTON, R. B., WONG, E. C. & FRANK, L. R. 1998. Dynamics of blood flow and oxygenation changes during brain activation: the balloon model. *Magnetic resonance in medicine*, 39**,** 855-864.

CAMPBELL, B. C., MITCHELL, P. J., KLEINIG, T. J., DEWEY, H. M., CHURILOV, L., YASSI, N., YAN, B., DOWLING, R. J., PARSONS, M. W. & OXLEY, T. J. 2015. Endovascular therapy for ischemic stroke with perfusion-imaging selection. *New England Journal of Medicine*, 372**,** 1009-1018.

CARANDANG, R., SESHADRI, S., BEISER, A., KELLY-HAYES, M., KASE, C. S., KANNEL, W. B. & WOLF, P. A. 2006. Trends in incidence, lifetime risk, severity, and 30-day mortality of stroke over the past 50 years. *Jama*, 296**,** 2939-2946.

CASSOT, F., LAUWERS, F., FOUARD, C., PROHASKA, S. & LAUWERS-CANCES, V. 2006. A novel three-dimensional computer-assisted method for a quantitative study of microvascular networks of the human cerebral cortex. *Microcirculation*, 13**,** 1-18.

CASSOT, F., LAUWERS, F., LORTHOIS, S., PUWANARAJAH, P., CANCES-LAUWERS, V. & DUVERNOY, H. 2010. Branching patterns for arterioles and venules of the human cerebral cortex. *Brain research*, 1313**,** 62-78.

CASTELLANOS, M., LEIRA, R., SERENA, J., PUMAR, J. M., LIZASOAIN, I., CASTILLO, J. & DÁVALOS, A. 2003. Plasma metalloproteinase-9 concentration predicts hemorrhagic transformation in acute ischemic stroke. *Stroke-a Journal of Cerebral Circulation*, 34**,** 40-44.

CEBRAL, J. R., YIM, P. J., LÖHNER, R., SOTO, O. & CHOYKE, P. L. 2002. Blood flow modeling in carotid arteries with computational fluid dynamics and MR imaging. *Academic radiology*, 9**,** 1286-1299.

CHAI, X., VAN HERK, M., HULSHOF, M. C. & BEL, A. 2012. A voxel-based finite element model for the prediction of bladder deformation. *Medical physics*, 39**,** 55-65.

CHAPMAN, S. J., SHIPLEY, R. J. & JAWAD, R. 2008. Multiscale modeling of fluid transport in tumors. *Bulletin of mathematical biology*, 70**,** 2334.

CHEN, N., GLAZIER, J. A., IZAGUIRRE, J. A. & ALBER, M. S. 2007. A parallel implementation of the Cellular Potts Model for simulation of cell-based morphogenesis. *Computer physics communications*, 176**,** 670-681.

CHERRICK, G. R., STEIN, S. W., LEEVY, C. M. & DAVIDSON, C. S. 1960. Indocyanine green: observations on its physical properties, plasma decay, and hepatic extraction. *The Journal of clinical investigation*, 39**,** 592-600.

CHIANG, J., KOWADA, M., AMES 3RD, A., WRIGHT, R. & MAJNO, G. 1968. Cerebral ischemia. III. Vascular changes. *The American journal of pathology*, 52**,** 455.

ÇINAR, Y., ŞENYOL, A. M. & DUMAN, K. 2001. Blood viscosity and blood pressure: role of temperature and hyperglycemia. *American journal of hypertension*, 14**,** 433-438.

COMMITTEE, C. F. D. 1998. Guide: Guide for the Verification and Validation of Computational Fluid Dynamics Simulations (AIAA G-077-1998 (2002)). American Institute of Aeronautics and Astronautics, Inc.

COPIN, J. C., BENGUALID, D. J., DA SILVA, R. F., KARGIOTIS, O., SCHALLER, K. & GASCHE, Y. 2011. Recombinant tissue plasminogen activator induces blood–brain barrier breakdown by a matrix metalloproteinase-9-independent pathway after transient focal cerebral ischemia in mouse. *European Journal of Neuroscience*, 34**,** 1085-1092.

COUNCIL, N. R. 2012. *Assessing the reliability of complex models: mathematical and statistical foundations of verification, validation, and uncertainty quantification*, National Academies Press.

CRAMER, S. P. & LARSSON, H. B. 2014. Accurate determination of blood–brain barrier permeability using dynamic contrast-enhanced T1-weighted MRI: a simulation and in vivo study on healthy subjects and multiple sclerosis patients. *Journal of Cerebral Blood Flow & Metabolism*, 34**,** 1655-1665.

DEKABAN, A. S. & SADOWSKY, D. 1978. Changes in brain weights during the span of human life: relation of brain weights to body heights and body weights. *Annals of Neurology: Official Journal of the American Neurological Association and the Child Neurology Society*, 4**,** 345-356.

DEL ZOPPO, G. J. & MABUCHI, T. 2003. Cerebral microvessel responses to focal ischemia. *Journal of Cerebral Blood Flow & Metabolism*, 23**,** 879-894.

DEL ZOPPO, G. J., POECK, K., PESSIN, M. S., WOLPERT, S. M., FURLAN, A. J., FERBERT, A., ALBERTS, M. J., ZIVIN, J. A., WECHSLER, L. & BUSSE, O. 1992. Recombinant tissue

plasminogen activator in acute thrombotic and embolic stroke. *Annals of neurology*, 32**,** 78-86.
DICE, L. R. 1945. Measures of the amount of ecologic association between species. *Ecology*, 26**,** 297-302.
DINTENFASS, L. 1967. Inversion of the Fahraeus–Lindqvist phenomenon in blood flow through capillaries of diminishing radius. *Nature*, 215**,** 1099-1100.
DONNAN, G. A., DAVIS, S. M., CHAMBERS, B. R., GATES, P. C., HANKEY, G. J., MCNEIL, J. J., ROSEN, D., STEWART-WYNNE, E. G. & TUCK, R. R. 1996. Streptokinase for acute ischemic stroke with relationship to time of administration. *Jama*, 276**,** 961-966.
DRAKE, J., MOSTACHFI, O., TENTI, G. & SIVALOGANATHAN, S. 1996. Realistic simple mathematical model of brain biomechanics for computer simulation of hydrocephalus and other brain abnormalities. *Can. J. Neurol. Sci*, 23**,** S5.
DRZEWIECKI, G., FIELD, S., MOUBARAK, I. & LI, J. K.-J. 1997. Vessel growth and collapsible pressure-area relationship. *American Journal of Physiology-Heart and Circulatory Physiology*, 273**,** H2030-H2043.
DUVERNOY, H. M., DELON, S. & VANNSON, J. 1981. Cortical blood vessels of the human brain. *Brain research bulletin*, 7**,** 519-579.
DZIALOWSKI, I., PEXMAN, J. W., BARBER, P. A., DEMCHUK, A. M., BUCHAN, A. M. & HILL, M. D. 2007. Asymptomatic hemorrhage after thrombolysis may not be benign: prognosis by hemorrhage type in the Canadian alteplase for stroke effectiveness study registry. *Stroke*, 38**,** 75-79.
EDMUND, J. M., KJER, H. M., VAN LEEMPUT, K., HANSEN, R. H., ANDERSEN, J. A. & ANDREASEN, D. 2014. A voxel-based investigation for MRI-only radiotherapy of the brain using ultra short echo times. *Physics in Medicine & Biology*, 59**,** 7501.
EGEMEN, E. & SOLAROGLU, I. 2017. Anatomy of cerebral veins and dural sinuses. *Primer on cerebrovascular diseases*. Elsevier.
EIDE, P. & SORTEBERG, W. 2007. Association among intracranial compliance, intracranial pulse pressure amplitude and intracranial pressure in patients with intracranial bleeds. *Neurological research*, 29**,** 798-802.
EL-BOURI, W. K. & PAYNE, S. J. 2015. Multi-scale homogenization of blood flow in 3-dimensional human cerebral microvascular networks. *Journal of theoretical biology*, 380**,** 40-47.
EL-BOURI, W. K. & PAYNE, S. J. 2018. Investigating the effects of a penetrating vessel occlusion with a multi-scale microvasculature model of the human cerebral cortex. *NeuroImage*, 172**,** 94-106.
EL-BOURI, W. K. & PAYNE, S. J. 2016. A statistical model of the penetrating arterioles and venules in the human cerebral cortex. *Microcirculation*, 23**,** 580-590.
ELMORE, S. 2007. Apoptosis: a review of programmed cell death. *Toxicologic pathology*, 35**,** 495-516.
FAHRAEUS, R. & LINDQVIST, T. 1931. The viscosity of the blood in narrow capillary tubes. *American Journal of Physiology-Legacy Content*, 96**,** 562-568.

FANG, Q. & BOAS, D. A. Tetrahedral mesh generation from volumetric binary and grayscale images. 2009 IEEE international symposium on biomedical imaging: from nano to macro, 2009. Ieee, 1142-1145.
FANG, Q., SAKADŽIĆ, S., RUVINSKAYA, L., DEVOR, A., DALE, A. M. & BOAS, D. A. 2008. Oxygen advection and diffusion in a three-dimensional vascular anatomical network. *Optics express*, 16**,** 17530-17541.
FERRO, J. M. 2003. Cardioembolic stroke: an update. *The lancet neurology*, 2**,** 177-188.
FILIPEK, P. A., RICHELME, C., KENNEDY, D. N. & CAVINESS JR, V. S. 1994. The young adult human brain: an MRI-based morphometric analysis. *Cerebral cortex*, 4**,** 344-360.
FIORELLI, M., BASTIANELLO, S., VON KUMMER, R. D., DEL ZOPPO, G. J., LARRUE, V., LESAFFRE, E., RINGLEB, A. P., LORENZANO, S., MANELFE, C. & BOZZAO, L. 1999. Hemorrhagic transformation within 36 hours of a cerebral infarct: relationships with early clinical deterioration and 3-month outcome in the European Cooperative Acute Stroke Study I (ECASS I) cohort. *Stroke*, 30**,** 2280-2284.
FLAMMER, J., PACHE, M. & RESINK, T. 2001. Vasospasm, its role in the pathogenesis of diseases with particular reference to the eye. *Progress in retinal and eye research*, 20**,** 319-349.
FOX, I. 1956. A new dye for continuous recording of dilution curves in whole blood independent of variations in blood oxygen saturation. *Circulation*, 14**,** 937-938.
FRANCIS, C., FREDERIC, L., SYLVIE, L., PRASANNA, P. & HENRI, D. 2009. Scaling laws for branching vessels of human cerebral cortex. *Microcirculation*, 16**,** 331-344.
FRONTERA, J. A., FERNANDEZ, A., SCHMIDT, J. M., CLAASSEN, J., WARTENBERG, K. E., BADJATIA, N., CONNOLLY, E. S. & MAYER, S. A. 2009. Defining vasospasm after subarachnoid hemorrhage: what is the most clinically relevant definition? *Stroke*, 40**,** 1963-1968.
GAGNON, L., SAKADŽIĆ, S., LESAGE, F., MUSACCHIA, J. J., LEFEBVRE, J., FANG, Q., YÜCEL, M. A., EVANS, K. C., MANDEVILLE, E. T. & COHEN-ADAD, J. 2015. Quantifying the microvascular origin of BOLD-fMRI from first principles with two-photon microscopy and an oxygen-sensitive nanoprobe. *Journal of Neuroscience*, 35**,** 3663-3675.
GARCIA-GONZALEZ, D., JAYAMOHAN, J., SOTIROPOULOS, S., YOON, S.-H., COOK, J., SIVIOUR, C., ARIAS, A. & JÉRUSALEM, A. 2017. On the mechanical behaviour of PEEK and HA cranial implants under impact loading. *Journal of the mechanical behavior of biomedical materials*, *69***,** 342-354.
GARCIA-GONZALEZ, D., RACE, N. S., VOETS, N. L., JENKINS, D. R., SOTIROPOULOS, S. N., ACOSTA, G., CRUZ-HACES, M., TANG, J., SHI, R. & JÉRUSALEM, A. 2018. Cognition based bTBI mechanistic criteria; a tool for preventive and therapeutic innovations. *Scientific Reports*, 8**,** 1-14.
GIBSON, C. L. 2013. Cerebral ischemic stroke: is gender important? *Journal of Cerebral Blood Flow & Metabolism*, 33**,** 1355-1361.
GLIEM, M., MAUSBERG, A. K., LEE, J. I., SIMIANTONAKIS, I., VAN ROOIJEN, N., HARTUNG, H. P. & JANDER, S. 2012. Macrophages prevent hemorrhagic infarct transformation in murine stroke models. *Annals of neurology*, 71**,** 743-752.

GOULD, I. G., TSAI, P., KLEINFELD, D. & LINNINGER, A. 2017. The capillary bed offers the largest hemodynamic resistance to the cortical blood supply. *Journal of Cerebral Blood Flow & Metabolism*, 37**,** 52-68.
GRANER, F. & GLAZIER, J. A. 1992. Simulation of biological cell sorting using a two-dimensional extended Potts model. *Physical review letters*, 69**,** 2013.
GREEN, A. E. & NAGHDI, P. M. 1969. On basic equations for mixtures. *The Quarterly Journal of Mechanics and Applied Mathematics*, 22**,** 427-438.
GRIFFIS, J. C., ALLENDORFER, J. B. & SZAFLARSKI, J. P. 2016. Voxel-based Gaussian naïve Bayes classification of ischemic stroke lesions in individual T1-weighted MRI scans. *Journal of neuroscience methods*, 257**,** 97-108.
GROUP, M. A. S. T. E. S. 1996. Thrombolytic therapy with streptokinase in acute ischemic stroke. *New England Journal of Medicine*, 335**,** 145-150.
GUIBERT, R., FONTA, C., RISSER, L. & PLOURABOUÉ, F. 2012. Coupling and robustness of intra-cortical vascular territories. *Neuroimage*, 62**,** 408-417.
GUO, L., VARDAKIS, J. C., LASSILA, T., MITOLO, M., RAVIKUMAR, N., CHOU, D., LANGE, M., SARRAMI-FOROUSHANI, A., TULLY, B. J. & TAYLOR, Z. A. 2018. Subject-specific multi-poroelastic model for exploring the risk factors associated with the early stages of Alzheimer's disease. *Interface focus*, 8**,** 20170019.
GUYTON, A. C., GRANGER, H. J. & TAYLOR, A. E. 1971. Interstitial fluid pressure. *Physiological reviews*, 51**,** 527-563.
HACKE, W. 1997. rtPA in acute ischemic stroke. *European perspective*, 49**,** S60-S62.
HAMANN, G. F., LIEBETRAU, M., MARTENS, H., BURGGRAF, D., KLOSS, C. U., BÜLTEMEIER, G., WUNDERLICH, N., JÄGER, G. & PFEFFERKORN, T. 2002. Microvascular basal lamina injury after experimental focal cerebral ischemia and reperfusion in the rat. *Journal of Cerebral Blood Flow & Metabolism*, 22**,** 526-533.
HARTMANN, D. A., COELHO-SANTOS, V. & SHIH, A. Y. 2022. Pericyte control of blood flow across microvascular zones in the central nervous system. *Annual review of physiology*, 84**,** 331-354.
HARUNA, M., KUMON, K., YAHAGI, N., WATANABE, Y., ISHIDA, Y., KOBAYASHI, N. & AOYAGI, T. 1998. Blood Volume Measurement at the Bedside Using ICG Pulse Spectrophometry. *Anesthesiology: The Journal of the American Society of Anesthesiologists*, 89**,** 1322-1328.
HAYWOOD, J., SHAFFER, R., FASTENOW, C., FINK, G. & BRODY, M. 1981. Regional blood flow measurement with pulsed Doppler flowmeter in conscious rat. *American Journal of Physiology-Heart and Circulatory Physiology*, 241**,** H273-H278.
HEISERMAN, J. E., DEAN, B., HODAK, J., FLOM, R., BIRD, C., DRAYER, B. & FRAM, E. 1994. Neurologic complications of cerebral angiography. *American Journal of Neuroradiology*, 15**,** 1401-1407.
HEUSCH, G., KLEINBONGARD, P., BÖSE, D., LEVKAU, B., HAUDE, M., SCHULZ, R. & ERBEL, R. 2009. Coronary microembolization: from bedside to bench and back to bedside. *Circulation*, 120**,** 1822-1836.

HILLEN, B., DRINKENBURG, B. A., HOOGSTRATEN, H. W. & POST, L. 1988. Analysis of flow and vascular resistance in a model of the cricle of Willis. *Journal of Biomechanics*, 21**,** 807-814.
HOFF, R. G., VAN DIJK, G. W., ALGRA, A., KALKMAN, C. J. & RINKEL, G. J. 2008. Fluid balance and blood volume measurement after aneurysmal subarachnoid hemorrhage. *Neurocritical care*, 8**,** 391-397.
HORIE, N., MOROFUJI, Y., IKI, Y., SADAKATA, E., KANAMOTO, T., TATEISHI, Y., IZUMO, T., ANDA, T., MORIKAWA, M. & TSUJINO, A. 2019. Impact of basal ganglia damage after successful endovascular recanalization for acute ischemic stroke involving lenticulostriate arteries. *Journal of Neurosurgery*, 132**,** 1880-1888.
HUANG, Y., PARRA, L. C. & HAUFE, S. 2016. The New York Head—A precise standardized volume conductor model for EEG source localization and tES targeting. *NeuroImage*, 140**,** 150-162.
HUANG, Y.-H., LIN, W.-C., LU, C.-H. & CHEN, W.-F. 2014. Volume of chronic subdural haematoma: is it one of the radiographic factors related to recurrence? *Injury*, 45**,** 1327-1331.
HUPPERT, T. J., ALLEN, M. S., BENAV, H., JONES, P. B. & BOAS, D. A. 2007. A multicompartment vascular model for inferring baseline and functional changes in cerebral oxygen metabolism and arterial dilation. *Journal of cerebral blood flow & metabolism*, 27**,** 1262-1279.
IADECOLA, C., BUCKWALTER, M. S. & ANRATHER, J. 2020. Immune responses to stroke: mechanisms, modulation, and therapeutic potential. *The Journal of clinical investigation*, 130**,** 2777-2788.
IIJIMA, T., AOYAGI, T., IWAO, Y., MASUDA, J., FUSE, M., KOBAYASHI, N. & SANKAWA, H. 1997. Cardiac output and circulating blood volume analysis by pulse dye-densitometry. *Journal of clinical monitoring*, 13**,** 81-89.
ITO, H., KANNO, I., IIDA, H., HATAZAWA, J., SHIMOSEGAWA, E., TAMURA, H. & OKUDERA, T. 2001. Arterial fraction of cerebral blood volume in humans measured by positron emission tomography. *Annals of nuclear medicine*, 15**,** 111-116.
ITO, H., KANNO, I., KATO, C., SASAKI, T., ISHII, K., OUCHI, Y., IIDA, A., OKAZAWA, H., HAYASHIDA, K. & TSUYUGUCHI, N. 2004. Database of normal human cerebral blood flow, cerebral blood volume, cerebral oxygen extraction fraction and cerebral metabolic rate of oxygen measured by positron emission tomography with 15O-labelled carbon dioxide or water, carbon monoxide and oxygen: a multicentre study in Japan. *European journal of nuclear medicine and molecular imaging*, 31**,** 635-643.
JAIN, A., JAIN, M., KANTHALA, A., DAMANIA, D., STEAD, L., WANG, H. & JAHROMI, B. 2013. Association of CT perfusion parameters with hemorrhagic transformation in acute ischemic stroke. *American Journal of Neuroradiology*, 34**,** 1895-1900.
JAIN, R. K. 1987. Transport of molecules in the tumor interstitium: a review. *Cancer research*, 47**,** 3039-3051.
JAIN, R. K., TONG, R. T. & MUNN, L. L. 2007. Effect of vascular normalization by antiangiogenic therapy on interstitial hypertension, peritumor edema, and

lymphatic metastasis: insights from a mathematical model. *Cancer research*, 67**,** 2729-2735.
JENKINS, A., MAXWELL, W. & GRAHAM, D. 1989. Experimental intracerebral haematoma in the rat: sequential light microscopical changes. *Neuropathology and applied neurobiology*, 15**,** 477-486.
JENKINSON, M., PECHAUD, M. & SMITH, S. BET2: MR-based estimation of brain, skull and scalp surfaces. Eleventh annual meeting of the organization for human brain mapping, 2005. Toronto., 167.
JICKLING, G. C., LIU, D., STAMOVA, B., ANDER, B. P., ZHAN, X., LU, A. & SHARP, F. R. 2014. Hemorrhagic transformation after ischemic stroke in animals and humans. *Journal of Cerebral Blood Flow & Metabolism*, 34**,** 185-199.
JIN, R., YANG, G. & LI, G. 2010. Molecular insights and therapeutic targets for blood–brain barrier disruption in ischemic stroke: critical role of matrix metalloproteinases and tissue-type plasminogen activator. *Neurobiology of disease*, 38**,** 376-385.
JOVIN, T. G., CHAMORRO, A., COBO, E., DE MIQUEL, M. A., MOLINA, C. A., ROVIRA, A., SAN ROMÁN, L., SERENA, J., ABILLEIRA, S. & RIBÓ, M. 2015. Thrombectomy within 8 hours after symptom onset in ischemic stroke. *New England Journal of Medicine*, 372**,** 2296-2306.
JOVIN, T. G., SAVER, J. L., RIBO, M., PEREIRA, V., FURLAN, A., BONAFE, A., BAXTER, B., GUPTA, R., LOPES, D. & JANSEN, O. 2017. Diffusion-weighted imaging or computerized tomography perfusion assessment with clinical mismatch in the triage of wake up and late presenting strokes undergoing neurointervention with Trevo (DAWN) trial methods. *International Journal of Stroke*, 12**,** 641-652.
JÓZSA, T. I., PADMOS, R. M., SAMUELS, N., EL-BOURI, W., HOEKSTRA, A. G. & PAYNE, S. J. 2021. A porous circulation model of the human brain for in silico clinical trials in ischaemic stroke. *Interface Focus*, 11**,** 20190127.
JOZSA, T. I., PETR, J., BARKHOF, F., PAYNE, S. J. & MUTSAERTS, H. J. 2022. MRI-based computational model generation for cerebral perfusion simulations in health and ischaemic stroke. *bioRxiv*.
KARNIADAKIS, G. E. 2009. VERIFICATION, VALIDATION, AND UNCERTAINTY QUANTIFICATION. *International Assessment of Research and Development in Simulation-based Engineering and Science***,** 89.
KASSNER, A., ROBERTS, T., MORAN, B., SILVER, F. & MIKULIS, D. 2009. Recombinant tissue plasminogen activator increases blood-brain barrier disruption in acute ischemic stroke: an MR imaging permeability study. *American journal of neuroradiology*, 30**,** 1864-1869.
KATAN, M. & LUFT, A. Global burden of stroke. Seminars in neurology, 2018. Thieme Medical Publishers, 208-211.
KATZ, V. J. 1979. The history of Stokes' theorem. *Mathematics Magazine*, 52**,** 146-156.
KHODAEE, F., VAHIDI, B. & FATOURAEE, N. 2016. Analysis of mechanical parameters on the thromboembolism using a patient-specific computational model. *Biomechanics and modeling in mechanobiology*, 15**,** 1295-1305.

KIM, D.-J., CZOSNYKA, Z., KASPROWICZ, M., SMIELEWESKI, P., BALEDENT, O., GUERGUERIAN, A.-M., PICKARD, J. D. & CZOSNYKA, M. 2012. Continuous monitoring of the Monro-Kellie doctrine: is it possible? *Journal of neurotrauma*, 29**,** 1354-1363.
KIMELBERG, H. 2004. Water homeostasis in the brain: basic concepts. *Neuroscience*, 129**,** 851-860.
KLEINMAN, J. T., HILLIS, A. E. & JORDAN, L. C. 2011. ABC/2: estimating intracerebral haemorrhage volume and total brain volume, and predicting outcome in children. *Developmental Medicine & Child Neurology*, 53**,** 281-284.
KLONER, R. A. 2011. No-reflow phenomenon: maintaining vascular integrity. *Journal of cardiovascular pharmacology and therapeutics*, 16**,** 244-250.
KOTHARI, R. U., BROTT, T., BRODERICK, J. P., BARSAN, W. G., SAUERBECK, L. R., ZUCCARELLO, M. & KHOURY, J. 1996. The ABCs of measuring intracerebral hemorrhage volumes. *Stroke*, 27**,** 1304-1305.
KRIEG, M., ARBOLEDA-ESTUDILLO, Y., PUECH, P.-H., KÄFER, J., GRANER, F., MÜLLER, D. & HEISENBERG, C.-P. 2008. Tensile forces govern germ-layer organization in zebrafish. *Nature cell biology*, 10**,** 429-436.
KURAMATSU, J. B., SAUER, R., MAUER, C., LÜCKING, H., KLOSKA, S. P., KIPHUTH, I.-C., STAYKOV, D., KÖHRMANN, M. & HUTTNER, H. B. 2011. Correlation of age and haematoma volume in patients with spontaneous lobar intracerebral haemorrhage. *Journal of Neurology, Neurosurgery & Psychiatry*, 82**,** 144-149.
KYRIACOU, S. K., MOHAMED, A., MILLER, K. & NEFF, S. 2002. Brain mechanics for neurosurgery: modeling issues. *Biomechanics and modeling in mechanobiology*, 1**,** 151-164.
LAKHAN, S. E., KIRCHGESSNER, A., TEPPER, D. & AIDAN, L. 2013. Matrix metalloproteinases and blood-brain barrier disruption in acute ischemic stroke. *Frontiers in neurology*, 4**,** 32.
LANG, G. E., VELLA, D., WATERS, S. L. & GORIELY, A. 2017. Mathematical modelling of blood–brain barrier failure and oedema. *Mathematical medicine and biology: a journal of the IMA*, 34**,** 391-414.
LAPCHAK, P. A., CHAPMAN, D. F. & ZIVIN, J. A. 2000. Metalloproteinase inhibition reduces thrombolytic (tissue plasminogen activator)–induced hemorrhage after thromboembolic stroke. *Stroke*.
LAUWERS, F., CASSOT, F., LAUWERS-CANCES, V., PUWANARAJAH, P. & DUVERNOY, H. 2008. Morphometry of the human cerebral cortex microcirculation: general characteristics and space-related profiles. *Neuroimage*, 39**,** 936-948.
LECOUFFE, N. E., KAPPELHOF, M., TREURNIET, K. M., RINKEL, L. A., BRUGGEMAN, A. E., BERKHEMER, O. A., WOLFF, L., VAN VOORST, H., TOLHUISEN, M. L. & DIPPEL, D. W. 2021. A randomized trial of intravenous alteplase before endovascular treatment for stroke. *New England Journal of Medicine*, 385**,** 1833-1844.
LEES, K. R., BLUHMKI, E., VON KUMMER, R., BROTT, T. G., TONI, D., GROTTA, J. C., ALBERS, G. W., KASTE, M., MARLER, J. R. & HAMILTON, S. A. 2010. Time to treatment with intravenous alteplase and outcome in stroke: an updated pooled

analysis of ECASS, ATLANTIS, NINDS, and EPITHET trials. *The Lancet*, 375**,** 1695-1703.
LEINONEN, V., VANNINEN, R. & RAURAMAA, T. 2018. Raised intracranial pressure and brain edema. *Handbook of Clinical Neurology*. Elsevier.
LI, X., VON HOLST, H., HO, J. & KLEIVEN, S. 3-D finite element modeling of brain edema: Initial studies on intracranial pressure using comsol multiphysics. Excerpt from the Proceedings of the COMSOL Conference, 2009.
LI, X., VON HOLST, H. & KLEIVEN, S. 2011. Influence of gravity for optimal head positions in the treatment of head injury patients. *Acta neurochirurgica*, 153**,** 2057-2064.
LIBBY, P. 2002. Atherosclerosis: the new view. *Scientific American*, 286**,** 46-55.
LINDLEY, R. I., WARDLAW, J. M., SANDERCOCK, P. A., RIMDUSID, P., LEWIS, S. C., SIGNORINI, D. F. & RICCI, S. 2004. Frequency and risk factors for spontaneous hemorrhagic transformation of cerebral infarction. *Journal of Stroke and Cerebrovascular Diseases*, 13**,** 235-246.
LINNINGER, A., GOULD, I., MARINNAN, T., HSU, C.-Y., CHOJECKI, M. & ALARAJ, A. 2013. Cerebral microcirculation and oxygen tension in the human secondary cortex. *Annals of biomedical engineering*, 41**,** 2264-2284.
LO, E. H., BRODERICK, J. P. & MOSKOWITZ, M. A. 2004. tPA and proteolysis in the neurovascular unit. *Stroke*, 35**,** 354-356.
LO, E. H., DALKARA, T. & MOSKOWITZ, M. A. 2003. Mechanisms, challenges and opportunities in stroke. *Nature reviews neuroscience*, 4**,** 399-414.
LOGG, A., ØLGAARD, K. B., ROGNES, M. E. & WELLS, G. N. 2012. FFC: the FEniCS form compiler. *Automated Solution of Differential Equations by the Finite Element Method*. Springer.
LOGG, A. & WELLS, G. N. 2010. DOLFIN: Automated finite element computing. *ACM Transactions on Mathematical Software (TOMS)*, 37**,** 1-28.
LORTHOIS, S., CASSOT, F. & LAUWERS, F. 2011. Simulation study of brain blood flow regulation by intra-cortical arterioles in an anatomically accurate large human vascular network. Part II: flow variations induced by global or localized modifications of arteriolar diameters. *Neuroimage*, 54**,** 2840-2853.
LORTHOIS, S., LAUWERS, F. & CASSOT, F. 2014. Tortuosity and other vessel attributes for arterioles and venules of the human cerebral cortex. *Microvascular research*, 91**,** 99-109.
LOSCALZO, J. & BRAUNWALD, E. 1988. Tissue plasminogen activator. *New England Journal of Medicine*, 319**,** 925-931.
LOZANO, R., NAGHAVI, M., FOREMAN, K., LIM, S., SHIBUYA, K., ABOYANS, V., ABRAHAM, J., ADAIR, T., AGGARWAL, R. & AHN, S. Y. 2012. Global and regional mortality from 235 causes of death for 20 age groups in 1990 and 2010: a systematic analysis for the Global Burden of Disease Study 2010. *The lancet*, 380**,** 2095-2128.
LUCAS, C. & PAYNE, S. An Anatomical Model of the Cerebral Vasculature and the Autoregulation of Cerebral Blood Flow. 6th World Congress of Biomechanics (WCB 2010). August 1-6, 2010 Singapore, 2010. Springer, 446-449.

LÜDERS, E., STEINMETZ, H. & JÄNCKE, L. 2002. Brain size and grey matter volume in the healthy human brain. *Neuroreport*, 13**,** 2371-2374.
MAESO, R., NAVARRO-CID, J., MUÑOZ-GARCÍA, R., RODRIGO, E., RUILOPE, L. M., LAHERA, V. & CACHOFEIRO, V. 1996. Losartan reduces phenylephrine constrictor response in aortic rings from spontaneously hypertensive rats: role of nitric oxide and angiotensin II type 2 receptors. *Hypertension*, 28**,** 967-972.
MAIER, A., GEE, M., REEPS, C., ECKSTEIN, H.-H. & WALL, W. 2010. Impact of calcifications on patient-specific wall stress analysis of abdominal aortic aneurysms. *Biomechanics and modeling in mechanobiology*, 9**,** 511-521.
MANDEVILLE, J. B., MAROTA, J. J., AYATA, C., MOSKOWITZ, M. A., WEISSKOFF, R. M. & ROSEN, B. R. 1999a. MRI measurement of the temporal evolution of relative CMRO2 during rat forepaw stimulation. *Magnetic Resonance in Medicine: An Official Journal of the International Society for Magnetic Resonance in Medicine*, 42**,** 944-951.
MANDEVILLE, J. B., MAROTA, J. J., AYATA, C., ZAHARCHUK, G., MOSKOWITZ, M. A., ROSEN, B. R. & WEISSKOFF, R. M. 1999b. Evidence of a cerebrovascular postarteriole windkessel with delayed compliance. *Journal of Cerebral Blood Flow & Metabolism*, 19**,** 679-689.
MARSH, E. B., LLINAS, R. H., HILLIS, A. E. & GOTTESMAN, R. F. 2013. Hemorrhagic transformation in patients with acute ischaemic stroke and an indication for anticoagulation. *European journal of neurology*, 20**,** 962-967.
MARTIN, W. W., POWERS, W. J. & RAICHLE, M. E. 1987. Cerebral blood volume measured with inhaled C15O and positron emission tomography. *Journal of Cerebral Blood Flow & Metabolism*, 7**,** 421-426.
MATTSON, D. L. 2001. Comparison of arterial blood pressure in different strains of mice. *American journal of hypertension*, 14**,** 405-408.
MERALI, Z., HUANG, K., MIKULIS, D., SILVER, F. & KASSNER, A. 2017. Evolution of blood-brain-barrier permeability after acute ischemic stroke. *PLoS One*, 12**,** e0171558.
MIHARA, K., AOKI, T., MORIGUCHI, A., MAEDA, M., FURUICHI, Y., MATSUOKA, N. & MUTOH, S. 2005. Prohemorrhagic and bleeding time activities of recombinant tissue plasminogen activator, heparin, aspirin, and a glycoprotein IIb/IIIa antagonist. *Journal of neurotrauma*, 22**,** 1362-1373.
MILLOY, M. & WOOD, E. 2015. Withdrawal from methadone in US prisons: cruel and unusual? *The Lancet*, 386**,** 316-318.
MODAT, M., RIDGWAY, G. R., TAYLOR, Z. A., LEHMANN, M., BARNES, J., HAWKES, D. J., FOX, N. C. & OURSELIN, S. 2010. Fast free-form deformation using graphics processing units. *Computer methods and programs in biomedicine*, 98**,** 278-284.
MOKHTARUDIN, M. 2016a. *Mathematical modelling of cerebral ischaemia-reperfusion injury*. University of Oxford.
MOKHTARUDIN, M. J. M. 2016b. *Mathematical modelling of cerebral ischaemia-reperfusion injury*. University of Oxford.
MOKHTARUDIN, M. J. M. & PAYNE, S. J. 2017. The study of the function of AQP4 in cerebral ischaemia–reperfusion injury using poroelastic theory. *International journal for numerical methods in biomedical engineering*, 33**,** e02784.

MOKHTARUDIN, M. M. & PAYNE, S. 2015. Mathematical model of the effect of ischemia–reperfusion on brain capillary collapse and tissue swelling. *Mathematical biosciences*, 263**,** 111-120.
MONRO, A. 1783. Observations on the Structure and Functions of the Nervous System.
MONTONEY, M., GARDELL, S. J. & MARDER, V. J. 1995. Comparison of the bleeding potential of vampire bat salivary plasminogen activator versus tissue plasminogen activator in an experimental rabbit model. *Circulation*, 91**,** 1540-1544.
MOORE, S. & DAVID, T. 2008. A model of autoregulated blood flow in the cerebral vasculature. *Proceedings of the Institution of Mechanical Engineers, Part H: Journal of Engineering in Medicine*, 222**,** 513-530.
MOORE, S., DAVID, T., CHASE, J., ARNOLD, J. & FINK, J. 2006. 3D models of blood flow in the cerebral vasculature. *Journal of biomechanics*, 39**,** 1454-1463.
MOORE, S., MOORHEAD, K., CHASE, J., DAVID, T. & FINK, J. 2005. One-dimensional and three-dimensional models of cerebrovascular flow.
MOTTO, C., CICCONE, A., ARITZU, E., BOCCARDI, E., DE GRANDI, C., PIANA, A. & CANDELISE, L. 1999. Hemorrhage after an acute ischemic stroke. *Stroke*, 30**,** 761-764.
MURPHY, G. & KNÄUPER, V. 1997. Relating matrix metalloproteinase structure to function: why the “hemopexin” domain? *Matrix Biology*, 15**,** 511-518.
MURRAY, K. D. 1964. Dimensions of the circle of Willis and dynamic studies using electrical analogy. *Journal of neurosurgery*, 21**,** 26-34.
MUSHTAQ, M., ABDUL MATEEN, M. & KIM, U.-H. 2019. Hyperglycemia associated blood viscosity can be a nexus stimuli. *Clinical Hemorheology and Microcirculation*, 71**,** 103-112.
MUTSAERTS, H., VAN DALEN, J., HEIJTEL, D., GROOT, P., MAJOIE, C., PETERSEN, E., RICHARD, E. & NEDERVEEN, A. 2015. Cerebral perfusion measurements in elderly with hypertension using arterial spin labeling. *PloS one*, 10**,** e0133717.
NAH, H.-W., KWON, S. U., KANG, D.-W., AHN, J.-S., KWUN, B.-D. & KIM, J. S. 2012. Moyamoya disease-related versus primary intracerebral hemorrhage: location and outcomes are different. *Stroke*, 43**,** 1947-1950.
NAKAGAWA, K., SERRADOR, J. M., LAROSE, S. L. & SOROND, F. A. 2011. Dynamic cerebral autoregulation after intracerebral hemorrhage: A case-control study. *BMC neurology*, 11**,** 1-8.
NASSAR, T., AKKAWI, S. E., SHINA, A., HAJ-YEHIA, A., BDEIR, K., TARSHIS, M., HEYMAN, S. N. & HIGAZI, A. A.-R. 2004. In vitro and in vivo effects of tPA and PAI-1 on blood vessel tone. *Blood*, 103**,** 897-902.
NEKLUDOV, M., BELLANDER, B.-M., BLOMBÄCK, M. & WALLEN, H. N. 2007. Platelet dysfunction in patients with severe traumatic brain injury. *Journal of neurotrauma*, 24**,** 1699-1706.
NIEWADA, M., KOBAYASHI, A., SANDERCOCK, P. A., KAMIŃSKI, B. & CZŁONKOWSKA, A. 2005. Influence of gender on baseline features and clinical outcomes among 17,370 patients with confirmed ischaemic stroke in the international stroke trial. *Neuroepidemiology*, 24**,** 123-128.

NIIMI, H., KOMAI, Y., YAMAGUCHI, S. & SEKI, J. 2006. Microembolic flow disturbances in the cerebral microvasculature with an arcadal network: a numerical simulation. *Clinical hemorheology and microcirculation*, 34**,** 247-255.
O'COLLINS, V. E., MACLEOD, M. R., DONNAN, G. A., HORKY, L. L., VAN DER WORP, B. H. & HOWELLS, D. W. 2006. 1,026 experimental treatments in acute stroke. *Annals of neurology*, 59**,** 467-477.
OBERKAMPF, W. L. & ROY, C. J. 2010. *Verification and validation in scientific computing*, Cambridge University Press.
OBERKAMPF, W. L., TRUCANO, T. G. & HIRSCH, C. 2004. Verification, validation, and predictive capability in computational engineering and physics. *Appl. Mech. Rev.*, 57**,** 345-384.
OKELL, T. W., CHAPPELL, M. A., KELLY, M. E. & JEZZARD, P. 2013. Cerebral blood flow quantification using vessel-encoded arterial spin labeling. *Journal of Cerebral Blood Flow & Metabolism*, 33**,** 1716-1724.
OOSTENVELD, R., FRIES, P., MARIS, E. & SCHOFFELEN, J.-M. 2011. FieldTrip: open source software for advanced analysis of MEG, EEG, and invasive electrophysiological data. *Computational intelligence and neuroscience*, 2011**,** 1-9.
PADMOS, R. M., JÓZSA, T. I., EL-BOURI, W. K., KONDURI, P. R., PAYNE, S. J. & HOEKSTRA, A. G. 2021. Coupling one-dimensional arterial blood flow to three-dimensional tissue perfusion models for in silico trials of acute ischaemic stroke. *Interface focus*, 11**,** 20190125.
PAN, Y., CAI, X., HUO, X., ZHAO, X., LIU, L., WANG, Y., MIAO, Z. & WANG, Y. 2018. Cost-effectiveness of mechanical thrombectomy within 6 hours of acute ischaemic stroke in China. *BMJ open*, 8**,** e018951.
PAPADEMETRIS, X., SINUSAS, A. J., DIONE, D. P., CONSTABLE, R. T. & DUNCAN, J. S. 2002. Estimation of 3-D left ventricular deformation from medical images using biomechanical models. *IEEE transactions on medical imaging*, 21**,** 786-800.
PAPANTCHEV, V., HRISTOV, S., TODOROVA, D., NAYDENOV, E., PALOFF, A., NIKOLOV, D., TSCHIRKOV, A. & OVTSCHAROFF, W. 2007. Some variations of the circle of Willis, important for cerebral protection in aortic surgery—a study in Eastern Europeans. *European journal of cardio-thoracic surgery*, 31**,** 982-989.
PARK, J., KO, Y., KIM, W.-J., JANG, M., YANG, M., HAN, M.-K., OH, C.-W., PARK, S.-H., LEE, J. & LEE, J. 2012. Is asymptomatic hemorrhagic transformation really innocuous? *Neurology*, 78**,** 421-426.
PARTY, I. S. W. 2012. *National clinical guideline for stroke*, London: Royal College of Physicians.
PATEL, A., BERDUNOV, V., KING, D., QUAYYUM, Z., WITTENBERG, R. & KNAPP, M. 2017. Executive summary Part 2: Burden of Stroke in the next 20 years and potential returns from increased spending on research. *London: Stroke Association*.
PATHMANATHAN, P. & GRAY, R. A. 2014. Verification of computational models of cardiac electro-physiology. *International journal for numerical methods in biomedical engineering*, 30**,** 525-544.
PAYNE, S. 2006. A model of the interaction between autoregulation and neural activation in the brain. *Mathematical biosciences*, 204**,** 260-281.

PAYNE, S. 2016. *Cerebral autoregulation: control of blood flow in the brain*, Springer.
PAYNE, S. J. 2017. *Cerebral Blood Flow And Metabolism: A Quantitative Approach*, World Scientific Publishing Company.
PAYNE, S. J. & LUCAS, C. 2018. Oxygen delivery from the cerebral microvasculature to tissue is governed by a single time constant of approximately 6 seconds. *Microcirculation*, 25**,** e12428.
PIERPAOLI, C., WALKER, L., IRFANOGLU, M. O., BARNETT, A., BASSER, P., CHANG, L.-C., KOAY, C., PAJEVIC, S., ROHDE, G. & SARLLS, J. TORTOISE: an integrated software package for processing of diffusion MRI data. ISMRM 18th annual meeting, 2010. Stockholm.
PLUTA, R. M., HANSEN-SCHWARTZ, J., DREIER, J., VAJKOCZY, P., MACDONALD, R. L., NISHIZAWA, S., KASUYA, H., WELLMAN, G., KELLER, E. & ZAUNER, A. 2009. Cerebral vasospasm following subarachnoid hemorrhage: time for a new world of thought. *Neurological research*, 31**,** 151-158.
POZRIKIDIS, C. 2010. Numerical simulation of blood and interstitial flow through a solid tumor. *Journal of mathematical biology*, 60**,** 75-94.
POZRIKIDIS, C. 2011. *Introduction to theoretical and computational fluid dynamics*, Oxford University Press.
POZRIKIDIS, C. 2013. Leakage through a permeable capillary tube into a poroelastic tumor interstitium. *Engineering Analysis with Boundary Elements*, 37**,** 728-737.
POZRIKIDIS, C. & FARROW, D. 2003. A model of fluid flow in solid tumors. *Annals of biomedical engineering*, 31**,** 181-194.
PRIES, A., SECOMB, T. W., GESSNER, T., SPERANDIO, M., GROSS, J. & GAEHTGENS, P. 1994. Resistance to blood flow in microvessels in vivo. *Circulation research*, 75**,** 904-915.
PRIES, A. R., NEUHAUS, D. & GAEHTGENS, P. 1992. Blood viscosity in tube flow: dependence on diameter and hematocrit. *American Journal of Physiology-Heart and Circulatory Physiology*, 263**,** H1770-H1778.
PRIES, A. R. & SECOMB, T. W. 2005. Microvascular blood viscosity in vivo and the endothelial surface layer. *American Journal of Physiology-Heart and Circulatory Physiology*, 289**,** H2657-H2664.
QUICK, C. M., YOUNG, W. L., LEONARD, E. F., JOSHI, S., GAO, E. & HASHIMOTO, T. 2000. Model of structural and functional adaptation of small conductance vessels to arterial hypotension. *American Journal of Physiology-Heart and Circulatory Physiology*, 279**,** H1645-H1653.
RASLAN, A. & BHARDWAJ, A. 2007. Medical management of cerebral edema. *Neurosurgical focus*, 22**,** 1-12.
REOROWICZ, P., OBIDOWSKI, D., KLOSINSKI, P., SZUBERT, W., STEFANCZYK, L. & JOZWIK, K. 2014. Numerical simulations of the blood flow in the patient-specific arterial cerebral circle region. *Journal of biomechanics*, 47**,** 1642-1651.
RIPPE, B., KAMIYA, A. & FOLKOW, B. 1978. Simultaneous measurements of capillary diffusion and filtration exchange during shifts in filtration-absorption and at graded alterations in the capillary permeability surface area product (PS). *Acta physiologica Scandinavica*, 104**,** 318-336.

RODRIGUEZ-LUNA, D., BOYKO, M., SUBRAMANIAM, S., KLOURFELD, E., JO, P., DIEDERICHS, B. J., KOSIOR, J. C., DOWLATSHAHI, D., AVIV, R. I. & MOLINA, C. A. 2016. Magnitude of hematoma volume measurement error in intracerebral hemorrhage. *Stroke*, 47**,** 1124-1126.

ROSENBERG, G. A. 2002. Matrix metalloproteinases in neuroinflammation. *Glia*, 39**,** 279-291.

ROY, C. J. & OBERKAMPF, W. L. 2011. A comprehensive framework for verification, validation, and uncertainty quantification in scientific computing. *Computer methods in applied mechanics and engineering*, 200**,** 2131-2144.

SAFAEIAN, N. & DAVID, T. 2013. A computational model of oxygen transport in the cerebrocapillary levels for normal and pathologic brain function. *Journal of Cerebral Blood Flow & Metabolism*, 33**,** 1633-1641.

SAFAEIAN, N., SELLIER, M. & DAVID, T. 2011. A computational model of hemodynamic parameters in cortical capillary networks. *Journal of theoretical biology*, 271**,** 145-156.

SALEEM, S., WANG, D., ZHAO, T., SULLIVAN, R. D. & REED, G. L. 2021. Matrix metalloproteinase-9 expression is enhanced by ischemia and tissue plasminogen activator and induces hemorrhage, disability and mortality in experimental stroke. *Neuroscience*, 460**,** 120-129.

SAVER, J. L., GOYAL, M., BONAFE, A., DIENER, H.-C., LEVY, E. I., PEREIRA, V. M., ALBERS, G. W., COGNARD, C., COHEN, D. J. & HACKE, W. 2015. Stent-retriever thrombectomy after intravenous t-PA vs. t-PA alone in stroke. *New England Journal of Medicine*, 372**,** 2285-2295.

SCHMID, F., BARRETT, M. J., JENNY, P. & WEBER, B. 2019. Vascular density and distribution in neocortex. *Neuroimage*, 197**,** 792-805.

SCHMID, F., TSAI, P. S., KLEINFELD, D., JENNY, P. & WEBER, B. 2017. Depth-dependent flow and pressure characteristics in cortical microvascular networks. *PLoS computational biology*, 13**,** e1005392.

SCHRAG, M., MCAULEY, G., POMAKIAN, J., JIFFRY, A., TUNG, S., MUELLER, C., VINTERS, H. V., HAACKE, E. M., HOLSHOUSER, B. & KIDO, D. 2010. Correlation of hypointensities in susceptibility-weighted images to tissue histology in dementia patients with cerebral amyloid angiopathy: a postmortem MRI study. *Acta neuropathologica*, 119**,** 291-302.

SECOMB, T., HSU, R., BEAMER, N. & COULL, B. 2000. Theoretical simulation of oxygen transport to brain by networks of microvessels: effects of oxygen supply and demand on tissue hypoxia. *Microcirculation*, 7**,** 237-247.

SECOMB, T. W. & PRIES, A. R. 2013. Blood viscosity in microvessels: experiment and theory. *Comptes Rendus Physique*, 14**,** 470-478.

SEKI, H., YOSHIMOTO, T., OGAWA, A. & SUZUKI, J. 1985. Hemodynamics in hemorrhagic infarction--an experimental study. *Stroke*, 16**,** 647-651.

SEVERINGHAUS, J. W. & HONDA, Y. 1987. History of blood gas analysis. VII. Pulse oximetry. *Journal of clinical monitoring*, 3**,** 135-138.

SEVICK, E. M. & JAIN, R. K. 1989. Geometric resistance to blood flow in solid tumors perfused ex vivo: effects of tumor size and perfusion pressure. *Cancer research*, 49**,** 3506-3512.
SEVICK, E. M. & JAIN, R. K. 1991. Measurement of capillary filtration coefficient in a solid tumor. *Cancer research*, 51**,** 1352-1355.
SHIPLEY, R. J. & CHAPMAN, S. J. 2010. Multiscale modelling of fluid and drug transport in vascular tumours. *Bulletin of mathematical biology*, 72**,** 1464-1491.
SHITYAKOV, S. & FÖRSTER, C. Y. 2018. Computational simulation and modeling of the blood–brain barrier pathology. *Histochemistry and cell biology*, 149**,** 451-459.
SMITH, A. F., SHIPLEY, R. J., LEE, J., SANDS, G. B., LEGRICE, I. J. & SMITH, N. P. 2014. Transmural variation and anisotropy of microvascular flow conductivity in the rat myocardium. *Annals of biomedical engineering*, 42**,** 1966-1977.
SMITH, S. M. 2002. Fast robust automated brain extraction. *Human brain mapping*, 17**,** 143-155.
SMITH, S. M., JENKINSON, M., WOOLRICH, M. W., BECKMANN, C. F., BEHRENS, T. E., JOHANSEN-BERG, H., BANNISTER, P. R., DE LUCA, M., DROBNJAK, I. & FLITNEY, D. E. 2004. Advances in functional and structural MR image analysis and implementation as FSL. *Neuroimage*, 23**,** S208-S219.
SNARSKA, K., KAPICA-TOPCZEWSKA, K., BACHÓRZEWSKA-GAJEWSKA, H. & MAŁYSZKO, J. 2016. Renal function predicts outcomes in patients with ischaemic stroke and haemorrhagic stroke. *Kidney and Blood Pressure Research*, 41**,** 424-433.
SONG, Q., CHENG, Y., WANG, Y., LIU, J., WEI, C. & LIU, M. 2021. Enlarged perivascular spaces and hemorrhagic transformation after acute ischemic stroke. *Annals of Translational Medicine*, *9*.
STARLING, E. H. 1896. On the absorption of fluids from the connective tissue spaces.
STATHAM, P. & TODD, N. 1990. Intracerebral haematoma: aetiology and haematoma volume determine the amount and progression of brain oedema. *Brain Edema VIII*. Springer.
STEINER, L. & ANDREWS, P. 2006. Monitoring the injured brain: ICP and CBF. *BJA: British Journal of Anaesthesia*, 97**,** 26-38.
STRANDGAARD, S., OLESEN, J., SKINHØJ, E. & LASSEN, N. 1973. Autoregulation of brain circulation in severe arterial hypertension. *Br Med J*, 1**,** 507-510.
STRICKER, R. B., WONG, D., SHIU, D. T., REYES, P. T. & SHUMAN, M. A. 1986. Activation of plasminogen by tissue plasminogen activator on normal and thrombasthenic platelets: effects on surface proteins and platelet aggregation.
STROMBERG, D. D. & FOX, J. R. 1972. Pressures in the pial arterial microcirculation of the cat during changes in systemic arterial blood pressure. *Circulation Research*, 31**,** 229-239.
SU, S.-W. 2012. Modelling blood flow and oxygen transport in the human cerebral cortex.
SU, S. W., CATHERALL, M. & PAYNE, S. 2012. The influence of network structure on the transport of blood in the human cerebral microvasculature. *Microcirculation*, 19**,** 175-187.

SUMII, T. & LO, E. H. 2002. Involvement of matrix metalloproteinase in thrombolysis-associated hemorrhagic transformation after embolic focal ischemia in rats. *Stroke*, 33**,** 831-836.
SWABB, E. A., WEI, J. & GULLINO, P. M. 1974. Diffusion and convection in normal and neoplastic tissues. *Cancer research*, 34**,** 2814-2822.
SZABÓ, A. & MERKS, R. M. 2013. Cellular potts modeling of tumor growth, tumor invasion, and tumor evolution. *Frontiers in oncology*, 3**,** 87.
TAMAKI, K. & HEISTAD, D. D. 1986. Response of cerebral arteries to sympathetic stimulation during acute hypertension. *Hypertension*, 8**,** 911-917.
TAN, S., WANG, D., LIU, M., ZHANG, S., WU, B. & LIU, B. 2014. Frequency and predictors of spontaneous hemorrhagic transformation in ischemic stroke and its association with prognosis. *Journal of neurology*, 261**,** 905-912.
TANNE, D., MACKO, R. F., LIN, Y., TILLEY, B. C. & LEVINE, S. R. 2006. Hemostatic activation and outcome after recombinant tissue plasminogen activator therapy for acute ischemic stroke. *Stroke*, 37**,** 1798-1804.
TERRUSO, V., D'AMELIO, M., DI BENEDETTO, N., LUPO, I., SAIA, V., FAMOSO, G., MAZZOLA, M. A., ARIDON, P., SARNO, C. & RAGONESE, P. 2009. Frequency and determinants for hemorrhagic transformation of cerebral infarction. *Neuroepidemiology*, 33**,** 261-265.
TERZAGHI, K. 1943. Theoretical soil mechanics. johnwiley & sons. *New York***,** 11-15.
THEVATHASAN, A., NAYLOR, J., CHURILOV, L., MITCHELL, P. J., DOWLING, R. J., YAN, B. & KWAN, P. 2018. Association between hemorrhagic transformation after endovascular therapy and poststroke seizures. *Epilepsia*, 59**,** 403-409.
TREURNIET, K. M., LECOUFFE, N. E., KAPPELHOF, M., EMMER, B. J., VAN ES, A. C., BOITEN, J., LYCKLAMA, G. J., KEIZER, K., YO, L. S. & LINGSMA, H. F. 2021. MR CLEAN-NO IV: intravenous treatment followed by endovascular treatment versus direct endovascular treatment for acute ischemic stroke caused by a proximal intracranial occlusion—study protocol for a randomized clinical trial. *Trials*, 22**,** 1-15.
TRIAL—ITALY, M. A. S. 1995. Randomised controlled trial of streptokinase, aspirin, and combination of both in treatment of acute ischaemic stroke. *The Lancet*, 346**,** 1509-1514.
TSITSOPOULOS, P. P., MARKLUND, N., ROSTAMI, E., ENBLAD, P. & HILLERED, L. 2020. Association of the bleeding time test with aspects of traumatic brain injury in patients with alcohol use disorder. *Acta neurochirurgica*, 162**,** 1597-1606.
TSUJI, K., AOKI, T., TEJIMA, E., ARAI, K., LEE, S.-R., ATOCHIN, D. N., HUANG, P. L., WANG, X., MONTANER, J. & LO, E. H. 2005. Tissue plasminogen activator promotes matrix metalloproteinase-9 upregulation after focal cerebral ischemia. *Stroke*, 36**,** 1954-1959.
TULLY, B. & VENTIKOS, Y. 2011. Cerebral water transport using multiple-network poroelastic theory: application to normal pressure hydrocephalus. *Journal of Fluid Mechanics*, 667**,** 188-215.
UNTERBERG, A., STOVER, J., KRESS, B. & KIENING, K. 2004. Edema and brain trauma. *Neuroscience*, 129**,** 1019-1027.

VAN DER STEEN, W., VAN DER ENDE, N. A., VAN KRANENDONK, K. R., CHALOS, V., VAN OOSTENBRUGGE, R. J., VAN ZWAM, W. H., ROOS, Y. B., VAN DOORMAAL, P. J., VAN ES, A. C. & LINGSMA, H. F. 2022. Determinants of Symptomatic Intracranial Hemorrhage After Endovascular Stroke Treatment: A Retrospective Cohort Study. *Stroke*, 53**,** 2818-2827.

VAN KRANENDONK, K. R., TREURNIET, K. M., BOERS, A. M., BERKHEMER, O. A., COUTINHO, J. M., LINGSMA, H. F., VAN ZWAM, W. H., VAN DER LUGT, A., VAN OOSTENBRUGGE, R. J. & DIPPEL, D. W. 2020. Added prognostic value of hemorrhagic transformation quantification in patients with acute ischemic stroke. *Frontiers in Neurology*, 11**,** 1335.

VAN KRANENDONK, K. R., TREURNIET, K. M., BOERS, A. M., BERKHEMER, O. A., VAN DEN BERG, L. A., CHALOS, V., LINGSMA, H. F., VAN ZWAM, W. H., VAN DER LUGT, A. & VAN OOSTENBRUGGE, R. J. 2019. Hemorrhagic transformation is associated with poor functional outcome in patients with acute ischemic stroke due to a large vessel occlusion. *Journal of neurointerventional surgery*, 11**,** 464-468.

VANDER, A. J., SHERMAN, J. H. & LUCIANO, D. S. 1998. *Human physiology: the mechanisms of body function*, New York, US: McGraw-Hill, 1990.

VEMMOS, K. N., SPENGOS, K., TSIVGOULIS, G., ZAKOPOULOS, N., MANIOS, E., KOTSIS, V., DAFFERTSHOFER, M. & VASSILOPOULOS, D. 2004. Factors influencing acute blood pressure values in stroke subtypes. *Journal of Human Hypertension*, 18**,** 253-259.

VLACHOPOULOS, C., O'ROURKE, M. & NICHOLS, W. W. 2011. *McDonald's blood flow in arteries: theoretical, experimental and clinical principles*, CRC press.

VON KUMMER, R., BRODERICK, J. P., CAMPBELL, B. C., DEMCHUK, A., GOYAL, M., HILL, M. D., TREURNIET, K. M., MAJOIE, C. B., MARQUERING, H. A. & MAZYA, M. V. 2015. The Heidelberg Bleeding Classification: classification of bleeding events after ischemic stroke and reperfusion therapy. *Stroke*, 46**,** 2981-2986.

WANG, C., CHEN, X., WANG, L., MAKIHATA, M., LIU, H.-C., ZHOU, T. & ZHAO, X. 2022a. Bioadhesive ultrasound for long-term continuous imaging of diverse organs. *Science*, 377**,** 517-523.

WANG, J. & PAYNE, S. J. 2021. Mathematical modelling of haemorrhagic transformation after ischaemic stroke. *Journal of Theoretical Biology*, 110920.

WANG, J., VAN KRANENDONK, K. R., EL-BOURI, W., MAJOIE, C. B. & PAYNE, S. J. 2022b. Mathematical modelling of haemorrhagic transformation within a multi-scale microvasculature network. *Physiological Measurement*.

WANG, S., LOU, M., LIU, T., CUI, D., CHEN, X. & WANG, Y. 2013. Hematoma volume measurement in gradient echo MRI using quantitative susceptibility mapping. *Stroke*, 44**,** 2315-2317.

WANG, X., JUNG, J., ASAHI, M., CHWANG, W., RUSSO, L., MOSKOWITZ, M. A., DIXON, C. E., FINI, M. E. & LO, E. H. 2000. Effects of matrix metalloproteinase-9 gene knock-out on morphological and motor outcomes after traumatic brain injury. *Journal of Neuroscience*, 20**,** 7037-7042.

WANG, X., LEE, S.-R., ARAI, K., LEE, S.-R., TSUJI, K., REBECK, G. W. & LO, E. H. 2003. Lipoprotein receptor–mediated induction of matrix metalloproteinase by tissue plasminogen activator. *Nature medicine*, 9**,** 1313-1317.

WANG, X., TSUJI, K., LEE, S.-R., NING, M., FURIE, K. L., BUCHAN, A. M. & LO, E. H. 2004. Mechanisms of hemorrhagic transformation after tissue plasminogen activator reperfusion therapy for ischemic stroke. *Stroke*, 35**,** 2726-2730.

WARDLAW, J. M. 2008. What is a lacune? : Am Heart Assoc.

WARDLAW, J. M., MURRAY, V., BERGE, E., DEL ZOPPO, G., SANDERCOCK, P., LINDLEY, R. L. & COHEN, G. 2012. Recombinant tissue plasminogen activator for acute ischaemic stroke: an updated systematic review and meta-analysis. *The Lancet*, 379**,** 2364-2372.

WEICKENMEIER, J., BUTLER, C., YOUNG, P., GORIELY, A. & KUHL, E. 2017. The mechanics of decompressive craniectomy: Personalized simulations. *Computer Methods in Applied Mechanics and Engineering*, 314**,** 180-195.

WEISER, M., SPANGLER, W. & GRIBBLE, D. 1977. Blood pressure measurement in the dog. *Journal of the American Veterinary Medical Association*, 171**,** 364-368.

WHEELER, J. B., MUKHERJEE, R., STROUD, R. E., JONES, J. A. & IKONOMIDIS, J. S. 2015. Relation of murine thoracic aortic structural and cellular changes with aging to passive and active mechanical properties. *Journal of the American Heart Association*, 4**,** e001744.

WILLIE, C., MACLEOD, D., SHAW, A., SMITH, K., TZENG, Y., EVES, N., IKEDA, K., GRAHAM, J., LEWIS, N. & DAY, T. 2012. Regional brain blood flow in man during acute changes in arterial blood gases. *The Journal of physiology*, 590**,** 3261-3275.

YAMAMOTO, T., KABUS, S., VON BERG, J., LORENZ, C., CHUNG, M. P., HONG, J. C., LOO JR, B. W. & KEALL, P. J. 2012. Reproducibility of four-dimensional computed tomography-based lung ventilation imaging. *Academic radiology*, 19**,** 1554-1565.

YANG, Y. & ROSENBERG, G. A. 2011. Blood–brain barrier breakdown in acute and chronic cerebrovascular disease. *Stroke*, 42**,** 3323-3328.

YEMISCI, M., GURSOY-OZDEMIR, Y., VURAL, A., CAN, A., TOPALKARA, K. & DALKARA, T. 2009. Pericyte contraction induced by oxidative-nitrative stress impairs capillary reflow despite successful opening of an occluded cerebral artery. *Nature medicine*, 15**,** 1031-1037.

YONG, V. W., POWER, C., FORSYTH, P. & EDWARDS, D. R. 2001. Metalloproteinases in biology and pathology of the nervous system. *Nature Reviews Neuroscience*, 2**,** 502-511.

YOON, J., GRUBOY, I. P.-C., ZAID, A., SALIL, S. G., CONNOLLY, M., ARONOW, W. S., ELOZOMOR, W. & ZUBERI, J. 2016. Isolated idiopathic aortitis with an unusually thickened aortic wall: case report. *Annals of Translational Medicine*, 4.

YUAN, S. Y. & RIGOR, R. R. 2011. *Regulation of Endothelial Barrier Function*, Morgan & Claypool Life Sciences.

ZHANG, K., HERZOG, H., MAULER, J., FILSS, C., OKELL, T. W., KOPS, E. R., TELLMANN, L., FISCHER, T., BROCKE, B. & STURM, W. 2014. Comparison of cerebral blood flow acquired by simultaneous [15O] water positron emission tomography and

arterial spin labeling magnetic resonance imaging. *Journal of cerebral blood flow & metabolism*, 34**,** 1373-1380.
ZHOU, R., GUO, F., AZARPAZHOOH, M. R., SPENCE, J. D., UKWATTA, E., DING, M. & FENSTER, A. 2020. A voxel-based fully convolution network and continuous max-flow for carotid vessel-wall-volume segmentation from 3D ultrasound images. *IEEE Transactions on Medical Imaging*, 39**,** 2844-2855.
ZIENKIEWICZ, O. 1982. Basic formulation of static and dynamic behaviour of soil and other porous media. *Numerical methods in geomechanics*. Springer.
ZWEIFACH, B. W. 1974. Quantitative studies of microcirculatory structure and function: I. Analysis of pressure distribution in the terminal vascular bed in cat mesentery. *Circulation Research*, 34**,** 841-857.
ZWEIFACH, B. W. & LIPOWSKY, H. H. 1977. Quantitative studies of microcirculatory structure and function. III. Microvascular hemodynamics of cat mesentery and rabbit omentum. *Circulation research*, 41**,** 380-390.